HIGH-ACCURACY, HIGH-SPEED 3D OPTICAL SENSING IN UNSTRUCTURED ENVIRONMENTS

A Dissertation

Submitted to the Faculty

of

Purdue University

by

Jae-Sang Hyun

In Partial Fulfillment of the

Requirements for the Degree

of

Doctor of Philosophy

May 2020

Purdue University

West Lafayette, Indiana

THE PURDUE UNIVERSITY GRADUATE SCHOOL
STATEMENT OF DISSERTATION APPROVAL

Prof. Song Zhang, Chair

School of Mechanical Engineering

Prof. Xinyan Deng

School of Mechanical Engineering

Prof. Shirley Dyke

School of Mechanical Engineering

Prof. Eric Matson

Department of Computer and Information Technology

Approved by:

Eckhard Groll

Head of Mechanical Engineering Graduate Program

ACKNOWLEDGMENTS

I would like to thank my family, friends, and teachers who supported me throughout my entire life, as well as during my academic career. Even if I am very pleased to take this opportunity to thank everyone around me, the following short words below will never convey my sincere gratitude.

First, I would like to thank my advisor, Prof. Song Zhang, who always supported me and gave me his constant guidance throughout not only research but also my entire graduate school life. He has not hesitated to help me do whatever I wanted to do in the lab. From designing a mechanical projector to developing autonomous vehicles, every research topic during my graduate study was interesting and fun. Even if I made many mistakes and failures during research, he kept giving me opportunities to have diverse learning experiences. I admire his tenacity and insight for research.

Next, I would like to thank my PhD advisory committee members, Prof. Xinyan Deng, Prof. Shirley Dyke, and Prof. Eric Matson, for their supportive advice and help. They have often suggested some great ideas to solve the problems that I faced at different junctures. I appreciate their generosity and support to let me gain new insights that I have rarely had before.

Moreover, I would like to extend my sincere gratitude to Prof. Dikai Liu and Wissam El-Ratal, who broadened my horizons by introducing me to real engineering problems. I definitely believe that the amount of time I devoted to thinking about the problems and extending the thoughts to reach solutions has helped me gain insights into problems. I really appreciate it. Working with them was a valuable experience.

Next, I would like to thank my great past and present team members, including Brian Acosta, Yatong An, Xia Chen, Michael Crawford, Prof. Junfei Dai, Michael Feller, Xiaowei Hu, Chufan Jiang, Yi-Hong Liao, Beatrice Lim, Ziping Liu, Prof. Andres Marrugo, Saw Yan Naung, Huitaek Yun, Bogdan Vlahov, Jialei Wang, Ruitao

Zhang, Peter Zibley, Prof. Min Zhong, Zexuan Zhu. I would like to give special thanks to my colleagues, Beiwen Li and Tyler Bell. When I was struggling to write an article and understand the fundamentals, I always got help from them. I am so proud of them and have no doubt of their successes in academia. It was an indescribable joy and great honor to work with them.

Lastly, I would not be here without my parents' sacrifice and support. When I was tired and exhausted in studying abroad, my parents always listened to me and encouraged me to overcome a difficult situation. To my parents, sorry for worrying you, and thank you so much. To my brother, you have always helped me a lot throughout my entire life. I respect you. To my friends, thank you for encouraging me and giving me positive words. To my fiancé, Seungeun Kim, thank you for your encouragement and continued love. I am always happy with you. I love you all.

TABLE OF CONTENTS

Page

LIST OF FIGURES . . . viii

ABSTRACT . . . xv

1 INTRODUCTION . . . 1

- 1.1 Motivation . . . 2
  - 1.1.1 Automation and robotics in construction . . . 2
  - 1.1.2 Autonomous vehicle . . . 3
  - 1.1.3 Forensic science . . . 4
- 1.2 Objectives . . . 5
- 1.3 Dissertation organization . . . 7

2 RELATED WORK . . . 9

- 2.1 Lidar . . . 9
- 2.2 Radar . . . 11
- 2.3 Vision-based 3D shape measurement technologies . . . 11

3 ENHANCED TWO-FREQUENCY PHASE-SHIFTING METHOD . . . 22

- 3.1 Introduction . . . 22
- 3.2 Principle . . . 24
  - 3.2.1 Two-frequency phase-shifting algorithm . . . 24
  - 3.2.2 DFP system model . . . 28
  - 3.2.3 Temporal unwrapping use minimum/maximum phase maps . . . 29
- 3.3 Simulations . . . 31
- 3.4 Experiment . . . 33
- 3.5 Summary . . . 37

4 SUPERFAST 3D ABSOLUTE SHAPE MEASUREMENT USING FIVE BINARY PATTERNS . . . 39

Page

4.1 Introduction 39
4.2 Principle 42
4.2.1 Three-step phase-shifting algorithm 42
4.2.2 Proposed phase-coding algorithm 43
4.2.3 Computational framework for reducing noise influence 45
4.3 Experiment 49
4.4 Summary 54
5 HIGH-SPEED THREE-DIMENSIONAL ABSOLUTE SHAPE MEASUREMENT WITH THREE BINARY PATTERNS 56
5.1 Introduction 56
5.2 Principle 58
5.2.1 Hilbert transform 58
5.2.2 Enhanced two-frequency phase unwrapping method 59
5.3 Experiment 61
5.4 Summary 65
6 HIGH-SPEED AND HIGH-ACCURACY 3D SURFACE MEASUREMENT USING A MECHANICAL PROJECTOR 67
6.1 Introduction 67
6.2 Principle 71
6.2.1 Least squares algorithm 71
6.2.2 Phase-shifted sinusoidal fringe pattern generation with a mechanical projector 72
6.2.3 Computational framework to achieve sub-pixel matching accuracy 75
6.2.4 Epipolar geometry 76
6.2.5 Refinement algorithm 78
6.3 Experiment 80
6.4 Discussion 86
6.5 Summary 87

Page

7 INFLUENCE OF PROJECTOR PIXEL SHAPE ON ULTRAHIGH-RESOLUTION 3D SHAPE MEASUREMENT . . . 89

7.1 Introduction . . . 89

7.2 Phase-shifting algorithm . . . 91

7.3 Simulation . . . 92

7.4 Experiment . . . 97

7.5 Summary . . . 102

8 SUMMARY AND FUTURE DIRECTIONS . . . 104

8.1 Summary of Contributions . . . 104

8.2 Future directions . . . 107

8.2.1 Phase-based feature detection for global mapping . . . 107

8.2.2 Customized 3D scanning system for maintenance of infrastructures . . . 108

REFERENCES . . . 109

VITA . . . 117

LIST OF PUBLICATIONS . . . 118

LIST OF FIGURES

Figure Page

2.1 (a) An image of Velodyne HDL-64E lidar[1]; (b) an image of lidar attached on top of a car[2]; (c) lidar data set at a moment[3]. 10

2.2 (a) An illustration of how the solid-state lidar sensor works[1];(b) a schematic diagram of using multiple solid-state lidar units[2]; (c) a illustration of scanning area that each solid-state lidar sensor can see 11

2.3 Commercial 3D cameras. (a) Microsoft Kinect[1]; (b) Intel RealSense[2];(c) Orbbec Astra[3]. 12

2.4 A typical setting of standard stereo vision 13

2.5 A schematic diagram of epipolar geometry 14

2.6 A pair of rectified images for stereo matching, horizontal green lines show representative epipolar lines 14

2.7 Statistically random patterns used in commercial 3D sensors. Patterns used in (a) Microsoft Kinect; (b) Intel RealSense; and (c) Apple iPhoneX. 16

2.8 A schematic diagram of a DFP setup 16

2.9 A schematic diagram of a DFP setup 17

2.10 A schematic diagram of binary-coding unwrapping algorithm 19

3.1 Conceptual idea of removing 2π jumps of low-frequency phase map by using the minimum phase map determined from geometric constraints. (a) Windowed regions shows phase map that acquired by camera at different depth z: red dashed window shows at z_{min} and solid blue window shows at z_{max}; (b) Corresponding Φ_{min} and Φ_{max} defined on the projector; (c) Cross sections of Φ_{min} and Φ_{max} and the wrapped phase maps with 2π discontinuities. 30

3.2 Determination of number of 2π to be added by using Φ_{min} when low-frequency phase has multiple 2π jumps. (a) Example of having two 2π jumps; (b) Example of having three 2π jumps. 31

Figure Page

3.3 Simulation result of standard two-frequency phase unwrapping when the signal to noise ratio (SNR) is not high (for this example SNR = 25). (a) Three high-frequency phase-shifted fringe patterns with phase shifts of $2\pi/3$ and fringe period of $T = 30$ pixels; (b) Zoom-in view of fringe patterns shown in (a); (c) Wrapped phase of the high-frequency fringe patterns; (d) Zoom-in view of the high-frequency phase; (e) Low frequency fringe patterns; (f) Low-frequency phase; (g) Unwrapped high-frequency phase; (h) Zoom-in-view of the unwrapped high-frequency phase. 32

3.4 Example of using one jump on the low-frequency phase and geometric constraints to unwrap the high-frequency phase. (a) Original low frequency phase ϕ_2, the phase at z_{min} from geometric constraints Φ_{min}, and the unwrapped low-frequency phase Φ_2; (b) Unwrapped high-frequency phase Φ_1. 32

3.5 Comparison of the conventional two-frequency phase-shifting algorithm and the proposed enhanced algorithm when the fringe patterns are of high quality. (a) Photograph of the measured statue; (b) One of the captured high-frequency fringe patterns; (c) Wrapped phase from high-frequency fringe patterns; (d) Wrapped phase from low-frequency fringe patterns with fringe period of 1140 pixels; (e) Unwrapped phase using the conventional two-frequency phase-shifting algorithm; (f) Wrapped phase from low-frequency fringe patterns with fringe period of 380 pixels; (g) Minimum wrapped phase Φ_{min}; (h) Unwrapped phase using the proposed method; (i) 3D result using the conventional two-frequency phase-shifting method; (j) 3D result using the proposed two-frequency phase-shifting method. 34

3.6 Close-up views of the results from Fig. 3.5 around the eye region. (a) Zoom-in view of the unwrapped phase map shown in Fig. 3.5(e); (b) Zoom-in view of the unwrapped phase map shown in Fig. 3.5(h); (c) Zoom-in view of 3D result shown in Fig. 3.5(i); (d) Zoom-in view of 3D result shown in Fig. 3.5(j). 35

3.7 Comparison of the conventional two-frequency phase-shifting algorithm and the proposed enhanced algorithm when the fringe patterns have low SNR. (a) One of the captured high-frequency fringe patterns; (b) 3D result using the conventional two-frequency phase-shifting method; (c)-(f) 3D results using the proposed two-frequency phase-shifting method when low frequency fringe patterns use two (c), three (d), four (e), and five (f) periods of sinusoidal fringes respectively; (g)-(k) Zoom-in views of the same regions for results shown in (b)-(f). 36

Figure Page

4.1 Cross section of ideal image. (a) Wrapped phase map with fringe period of 30 pixels; (b) comparison of the stair phase with the fringe order after rounding off the phase to the nearest integer;(c) absolute phase directly obtained from Eq. (4.11); (d) absolute phase after removing spikes. 45

4.2 Conceptual idea of removing 2π discontinuity of stair phase map by using the minimum phase. (a) Wrapped stair phase map by using Eq. (4.10); (b) unwrapped stair phase map after adding 2π where discontinuity occurs; (c) cross section of Φ_{min} and Φ_s and the wrapped phase maps. 48

4.3 Determination of the number of 2π jumps of the stair phase over two periods.49

4.4 Experimental setup for DFP calibration 50

4.5 Experimental captured data of the proposed method with a fringe period of 1140 pixels for the stair phase. (a) Photograph of the measured statue; (b)-(d) three phase-shifted high-frequency fringe images; (e)-(f) two phase-shifted low-frequency fringe images; (g) wrapped phase from high-frequency fringe patterns; (h) absolute stair phase map Φ_s; (i) fringe order map K; (j) unwrapped phase Φ; (k) 3D reconstruction result. 51

4.6 Experimental captured data of the proposed method using geometric constraints. (a)-(b) two stair-shaped patterns (I_4 and I_5) for ϕ_s with a fringe period of 570 pixels; (c) wrapped stair phase ϕ_s with a 2π discontinuity; (d) the artificial minimum phase map when $z = z_{min}$; (e) unwrapped stair phase Φ_s using the geometric constraints; (f) fringe order map K; (g) unwrapped phase Φ; (h) 3D reconstruction result using the proposed method without applying any filter; (i) filtered 3D reconstruction result. 52

4.7 Images of the stair phase and graphs of a cross section to compare the real number with its quantized number. (a) Absolute stair phase map by using the conventional method; (b) cross section of the red line on (a) to describe R and corresponding K of the conventional method; (c) absolute stair phase map by using the proposed method; (d) cross section of the red line on (c) to describe R and corresponding K of the proposed method. 54

4.8 Measurement result of capturing hands in high-speed. (a) Photograph of two hands; (b) one of three phase-shifted fringe patterns; (c) 3D reconstruction result. 55

5.1 Computational framework of the proposed method. 62

5.2 Experimental setup for DFP system. 63

Figure Page

5.3 Experimental results of a uniform sphere using the proposed method. (a) DC component fringe image; (b) low-frequency fringe image; (c) high-frequency fringe image; (d) difference map of low-frequency fringe image; (e) Hilbert-transformed map of low-frequency; (f) low-frequency wrapped phase; (g) high-frequency wrapped phase; (h) unwrapped phase map using geometric constraints; (i) 3D reconstruction result. 64

5.4 Experimental results of a complex sculpture using the proposed method. (a) DC component of the measured statue; (b) low-frequency fringe image; (c) high-frequency fringe image; (d) 3D reconstruction result. 65

5.5 Measurement result of a flapping bird robot in high-speed. (a) DC component of the fringe images at the specific moment; (b)-(d) 3D reconstruction results (Video 1, MPEG, 5.9 MB). 66

5.6 Measurement result of falling multiple balls in high-speed. (a) DC component of the fringe images at the specific moment; (b)-(d) 3D reconstruction results (Video 2, MPEG, 3.8 MB). 66

6.1 Schematic diagram of the mechanical projection system. 73

6.2 Timing diagram for the proposed high-speed 3D shape measurement system. Here T^s represents the period of the slot projection; T^c represents the period of the signal generated by the microprocessor to trigger both high-speed cameras; t^{exp} represents the exposure time of the camera; and N represents the number of phase-shifted fringe patterns required for one 3D reconstruction. 74

6.3 Computational framework of our proposed 3D reconstruction method. . . . 75

6.4 Illustration of epipolar geometry for a stereo-vision system. 77

6.5 Image rectification to facilitate correspondence searching. (a) Texture image captured by the left camera; (b) rectified image of (a); (c) a pair of rectified images for stereo matching, horizontal green lines ($v_1, v_2, \dots$) show representative epipolar lines. 77

6.6 Graphical illustrations of the proposed disparity map establishments on one epipolar line v. The first row image shows two rectified images; the second row image illustrates the rough corresponding point establishment using the standard stereo-vision algorithm on the rectified texture image; the third row image illustrates that first step of refinement by applying the phase constraint, e.g., the initial corresponding point $P^r(u_0^r, v)$ is shifted by τ_0 to $P^r(u_0^r+\tau_0, v)$; and the bottom row image shows the last refinement stage by subpixel interpolation, further move $P^r(u_0^r+\tau_0, v)$ by $\Delta\tau$ to the ultimate matching point $P^r(u^r, v)$. 79

Figure Page

6.7 Photograph of experimental hardware system setup. 81

6.8 Measurement results of a ping-pong ball. (a) One of three phase-shifted fringe patterns captured by the left camera; (b) the texture image obtained by averaging three fringe patterns captured by the left camera; (c) wrapped phase map from those images captured by the left camera; (d)-(f) corresponding images for the right camera. 82

6.9 Measurement results of a ping-pong ball shown in Fig. 6.8. (a) 3D reconstruction using the rough disparity map generated by the ELAS algorithm; (b) 3D reconstruction result from refined disparity map after applying our proposed refinement algorithm; (c) overlays of the ideal fitted sphere and the measured data; (d) difference map between the fitted ideal sphere and the measured data (rms error of approximately 6 μm, and the standard deviation of approximately 78 μm). 83

6.10 Measurement results of a statue with complex geometry. (a) Photograph of the sculpture; (b) one of three phase-shifted fringe patterns captured by the left camera; (c) the corresponding texture image; (d) 3D reconstruction using the rough disparity map generated by the ELAS algorithm; (e) 3D reconstruction by applying the phase constraint; (f) 3D reconstruction using our proposed sub-pixel level refinement algorithm. 84

6.11 Closed-up views of the results from Fig. 6.10 around the mouth region. (a) Zoom-in view of Fig. 6.10(a); (b) zoom-in view of Fig. 6.10(d); (c) zoom-in view of Fig. 6.10(e); (d) zoom-in view of Fig. 6.10(f). 84

6.12 Measurement results of multiple isolated objects. (a) Photograph of the objects; (b) 3D reconstruction using the rough disparity map; (d) 3D reconstruction using the refined disparity map. 85

6.13 Experimental results of measuring a rapidly moving object. Five representative frames from a sequence of recording shown in the associated with Visualization 1 86

7.1 Illustration of two different types of DLP projectors. (a) Rectangular shaped pixels and the rotation axis; (b) diamond-shaded pixels and the rotation axis; (c) row and column definition of rectangular-shaped pixels; (d) row and column definition of diamond-shaped pixels. 92

7.2 Ideal binary patterns with different projector pixel shapes. (a) One of the binary patterns for a projector with rectangular-shaded pixels; (b) one of the binary patterns for a projector with diamond-shaded pixels. 93

Figure Page

7.3 Simulations for ultrahigh resolution captured system. (a) One of the captured fringe images for the projector with rectangular-shaped pixels; (b) one of the captured fringe images for the projector with diamond-shaped pixels; (c) wrapped phase map for the captured fringe images for the projector with rectangular-shaped pixels; (d) wrapped phase map for the captured fringe images for the projector with diamond-shaped pixels. . . . 94

7.4 Representative phase error maps with different projector-to-camera pixel size ratios. For all images, purely black represents absolute phase error of 0 rad, and purely white represents absolute phase error of 0.57 rad. (a) Phase error map for the captured fringe images for the projector with rectangular-shaped pixels (rms 0.12 rad) when projector-camera pixel size ratio is 16:1; (b) phase error map for the captured fringe images for the projector with diamond-shaped pixels (rms 0.17 rad) when projector-camera pixel size ratio is 16:1; (c)-(d) phase error maps results when the projector-camera pixel size ratio is 2:1; (e)-(f) phase error maps results when the projector-camera pixel size ratio is 1:1. 94

7.5 Simulation results of two projector types with different projector-to-camera pixel ratio with binary patterns. 95

7.6 Comparing simulation results when the projected fringe patterns are sinusoidal. (a) One of the captured fringe images for the projector with rectangular-shaped pixels; (b) one of the captured fringe images for the projector with diamond-shaped pixels; (c) phase error map for the captured fringe images for the projector with rectangular-shaped pixels; (d) phase error map for the captured fringe images for the projector with diamond-shaped pixels. 96

7.7 Simulation results of two projector types with different projector-to-camera pixel size ratios when projected patterns are sinusoidal patterns. 96

7.8 Photographs of experimental system setups. (a) *System I*: system using a projector with diamond-shaped pixels; (b) *System II*: system using a projector with rectangular-shaped pixels. 97

7.9 Representative captured images. (a) One of the captured fringe images from *System I*; (b) one of the captured fringe images from *System II*; (c) zoom-in view of the pattern shown in (a); (d) zoom-in view of the pattern shown in (b). 98

Figure Page

7.10 Phase error analysis for the flat plane experiments. (a) Phase error map of *System I* when projector-camera pixel ratio is 16:1; (b) Phase error map of *System II* when projector-camera pixel ratio is 16:1; (c)-(d) phase error maps results when the projector-camera pixel size ratio is 2:1; (e)-(f) phase error maps results when the projector-camera pixel size ratio is 1:1. 99

7.11 Experimental result of two projector types with respect to different projector-to-camera pixel size ratios. 100

7.12 Experimental result of a sphere. (a) Photograph captured by the first system; (b) one of the fringe images captured by *System I*; (c) 3D result by *System I*; (d) zoom-in view of (c); (e) photograph captured by *System II*; (f) one of the fringe images captured by *System II*; (g) 3D result by *System II*; (h) zoom-in view of (g). 101

7.13 Experimental results of a statue. (a) Photograph captured by *System I*; (b) one of the fringe images captured by *System I*; (c) 3D result with *System I*; (d) zoom-in view of (c); (e) photograph captured by *System II*; (f) one of the fringe images captured by *System II*; (g) 3D result with *System II*; (h) zoom-in view of (g). 102

7.14 Experimental results of complex 3D objects with different projector-to-camera pixel size ratios. (a) Photo of the object measured with projector-to-camera pixel size ratio of 2:1; (b) 3D result with *System I*; (c) 3D result with *System II*; (d) close-up view of (b); (e) close-up view of (c); (f) Photo of the object measured with projector-to-camera pixel size ratio of 1:1; (g) 3D result with *System I*; (h) 3D result with *System II*; (i) close-up view of (g); (j) close-up view of (h). 103

ABSTRACT

Hyun, Jae-Sang Ph.D., Purdue University, May 2020. High-Accuracy, High-speed 3D Optical Sensing in Unstructured Environments. Major Professor: Prof. Song Zhang, School of Mechanical Engineering.

Over the last few decades, as many companies have released low-cost commercialized 3D sensors, vision-based 3D sensing has been more accessible and ubiquitous. As a result, the range of applications for 3D-sensing technology has been extended to medicine, entertainment, and manufacturing, as well as other industries. However, unlike with well-controlled industries such as manufacturing factories, commercial sensors and resolutions are not yet accurate enough to be applied in unstructured environments, such as construction sites. For example, to inspect the inside of large infrastructures such as steel bridges, robots need high-accuracy 3D maps for inspection and path planning, and robot sensors should be robust enough to withstand harsh weather. To achieve the goal of scanning and inspecting surrounding environments, the 3D imaging system needs to reconstruct 3D images with high accuracy, high speed, and robustness to noise.

The first challenge in realizing a high-accuracy 3D imaging system in unstructured environments is noise in captured images. To improve the robustness of 3D images, we developed a computational framework by using geometric constraints for high-accuracy 3D sensing with only two-frequency patterns. A previously existing two-frequency phase unwrapping method has a limitation in accuracy because the scaling factor, which is calculated by the difference in fringe width between low-frequency and high-frequency patterns, significantly amplifies the noise signal. The framework suggested to use the relationship of optical devices for 3D sensing inversely. We can dramatically decrease the scaling factor required to reconstruct 3D images. Without

additional patterns, we can measure the geometry of objects within a certain depth range accurately.

The second challenge is mainly caused by the dynamic motion of moving platforms. If the sampling rate of 3D sensing is low, it is difficult for robots to localize the platform, generate 3D maps for surrounding environment, and make a right decision in planning a path or inspecting sites based on the information. To increase the speed of 3D sensing, we can reduce the number of patterns used for generating one 3D image. The number of patterns is an important factor in determining the speed of 3D reconstruction because a camera captures the patterns sequentially, which means that the number of patterns is proportional to the time taken to capture a set of images for one 3D image. We developed a method to reduce the number of patterns by using geometric constraints. In addition, by integrating texture image of the object with a phase-coding method, we used a total of five binary patterns to get absolute phase map for 3D reconstruction. By doing experiments with a high-speed camera, the sensing system captures 2D images at 3,333 Hz, and 3D images at 667 Hz.

Although the speed of 3D sensing has increased through reducing the number of patterns, the system has fundamental limitations in speed and spectrum of light. The system typically includes at least one Digital Light Processing (DLP) projector because of its accuracy and flexibility. However, the mechanism of the DLP projector, which flips a set of micro mirrors inside the projector for determining whether each pixel is turned on or off, slows down the speed of 3D sensing. To overcome the speed limitation, we designed a custom-made mechanical projector that rotates a wheel with evenly spaced spokes. By using the rotating wheel, the projector generates fringe patterns for phase retrieval, which is the same as that which the DLP projector generates. With the mechanism, we realize a speed of up to 10 kHz for 3D sensing. In addition, we can overcome another limitation the DLP projector has, which is a limited spectrum of light. The micro mirrors can reflect only a specific light spectrum, and the light emitter inside the projector is not replaceable. The mechanical projector places the source of light independently, so, a broad-light spectrum—including visible, infrared (IR), near infrared (NIR), and ultra-violet light—can be used for 3D sensing.

In summary, this dissertation research has contributed methods for realizing high-accuracy and high-speed 3D shape measurement: (1) using geometric constraints in phase-retrieval procedures to reduce noise on the captured images; (2) reducing the number of images for one 3D image to realize high-speed 3D shape measurement; and (3) developing a new type of projector to avoid the limitations in light spectrum and achieve high-speed 3D data. These contributions enable engineers, workers, and even robots to monitor unstructured environments with 3D sensor accurately and quickly analyze the situations they face in the fields of infrastructure maintenance, homeland security, and construction.

1. INTRODUCTION

Since the 1990s, automation in manufacturing has led to highly increased productivity and efficiency. The term *automobile factory* may conjure up an image of numerous robot arms engaged in manufacturing processes, such as welding, assembly, and painting. To minimize the defect rate of the final products, numerous sensor technologies are integrated and used for inspecting products or supervising processes in detail. Accurate 3D sensing is of especially great importance to manufacturing processes for quality improvement and defect reduction [1–3]. Although some accurate measuring tools use a contact method, inspecting a product by contacting a number of points takes a long time, thus making it more desirable to use a non-contact method for the sake of expediency.

The non-contact optical techniques for 3D sensing utilizes the properties of light; this requires an environment that can block factors such as lighting, air, and temperature from affecting the sensors' performance. A manufacturing factory is good because it can readily control these factors; however, it is difficult to apply the same technology to unstructured environments such as construction sites because these sites are more vulnerable to the changes in the environment. Even if the release of low-cost commercial 3D sensors makes it easier to generate 3D images of the surrounding environment, the accuracy and spatial resolution are still very low compared to the level of accuracy required in automation and robotics [4]. More crucially, these 3D sensors are vulnerable to dust and changes of lighting, which makes it difficult for them to be used in unstructured environments.

This dissertation aims to improve 3D sensing technology by allowing it to be used in unstructured environments. Specifically, the research focuses on achieving (1) high robustness to noise, (2) high-accuracy and high-speed 3D reconstruction, and (3) seamless stitching of 3D images for the surrounding environments. The goal of my research is to deal with each of these issues and ultimately seek a way to adapt the 3D technology in the unstructured environments.

The rest of this chapter provides motivation and objectives for the current research, followed by the overall organization of the dissertation.

1.1 Motivation

1.1.1 Automation and robotics in construction

Automation and robotics in construction (ARC) has not received much attention from companies and governments as much as manufacturing has [5]. Although an astronomical amount of money is allocated to build environments, infrastructures, and facilities every year, productivity in the construction industry has been declining [6]. Furthermore, the societies of many developed countries are rapidly aging, and the number of workers in construction sites are decreasing [7]. Even the current young generation is reluctant to work in the construction industry, which consumes tremendous raw materials and exposes workers to harsh working conditions. For these reasons, governments, major companies, and universities are trying to apply automation and robotics in construction to replace human workers with the robots.

One major example of robots in construction is that of mobile robots in steel-bridge inspection. There are more than 600,000 bridges in the United States, and among them, more than 50,000 bridges are structurally deficient and in need of repair [8]. In order to inspect the inside of the steel-bridge structures, human workers have to climb the huge steel bridge and go through narrow tunnels. This human labor costs a tremendous amount of money every year [9] and is not very accurate because it necessarily entails human errors. Furthermore, this kind of inspection increases the risk for serious physical injury to construction workers. According to an Occupational Safety and Health Administration (OSHA) report, working in confined spaces for a long time increases the risk of serious physical injury [10]. For these reasons, mobile robots have been widely used in steel-bridge inspections.

Unlike the robots in a manufacturing line performing repetitive tasks in an unchanged setting, mobile-inspection robots respond to their surrounding unstructured environments in approaching the target position and carrying out tasks. Additionally, they must deal with changes in the environment, such as the interference of lighting, dust, and weather. With the development of a high-performance processor, modern robots have been improved to integrate information from various types of sensors and process the data in real time to plan a motion path. However, the complexity of the unstructured environment in construction sites makes it difficult for robots to apply general localization and mapping algorithms. A few research groups designed the inspection robots to generate 3D maps inside tunnels, based on information from the sensors [11]. They succeeded in making the robots plan the paths with a laser-based 3D sensor [12]. However, the robots' sensors did not have high accuracy and resolution to recognize the areas that needed renovation.

Measuring the depth of the area and detecting the location of the rust are some of the key factors in diagnosing the status of the bridge, and this requires sensors with high accuracy and high resolution. The improved sensor will not only increase the task performance, but will also reduce the inspection time for robots.

1.1.2 Autonomous vehicle

Autonomous vehicles have been studied extensively since the 2000s. Many international and domestic competitions, such as DARPA Urban Challenge, to elevate levels of autonomy in vehicles [13]; additionally, major companies such as Google and Tesla have invested significant capital into commercializing their autonomous vehicles. For passenger transportation, the levels of autonomous driving can be classified into five levels, from zero (non-autonomous vehicle) to five (fully autonomous, or without the need of a human driver) [14]. With the development of sensors, networks, image processing, and computing power, many companies have achieved a goal of highly automated driving; currently, a vehicle can drive autonomously for quite a long time when accompanied by a human driver [15].

Despite these achievements, there are still many challenges to overcome. For instance, the vehicle should be able to run in an unstructured environment where no traffic lights are on the road or lanes are rarely visible; it also has to resolve the social dilemma of autonomous vehicle [16], In addition, the vehicle should be able to update its map in real time, have reactive behavior for avoiding obstacles, and share information with vehicle-to-vehicle (V2V) technology [17, 18]. Currently, the vehicle localizes itself by following global positioning system (GPS) signal and maps its surroundings by using information from other sensors, such as lidar, radar, and camera. Though the performance of lidar, which reconstructs 3D point clouds using time-of-flight (TOF), has improved a lot, the resolution of the lidar is not enough to detect surrounding objects independently. The camera is not sufficient because there is no depth information of the image. In this context, high-speed and high-resolution 3D sensing with texture image for classification of the objects and mapping the surroundings in 3D could greatly improve the performance of autonomous vehicles.

1.1.3 Forensic science

With developments in the field of chemical and material science, a variety of chemicals and tools have been used to collect evidence at crime scenes. However, for collecting shoe prints or tire treads, investigators still prefer conventional methods, such as plastering and measuring the size of the evidence with measuring tape because newer technologies such as 3D scanners are expensive, not user-friendly, and not intuitive. Although plastering can reconstruct the shoe prints fairly well, the procedure of hardening takes a lot of time; more crucially, it is an exothermic process, which might ruin the site of the incident. In addition, the maintenance of the collected data using the conventional method risks data loss. Therefore, the Forensic Science Research and Development Technology Working Group (TWG) has prioritized research and development (R&D) to develop a system that satisfies operational requirements for forensic science [19]. Because capturing the crime scene and collecting evidence requires very high accuracy, it is another possibility where non-destructive 3D scanning technology can be used.

1.2 Objectives

- **Develop a method to improve the robustness and accuracy of the 3D scanning algorithm by using geometric constraints.**

  Compared to many other 3D reconstruction methods, the digital fringe projection system (DFP) is preferable for scanning shoe prints in forensic science and a painted surface for infrastructure maintenance because of its high spatial resolution and high accuracy. Typically, the standard DFP system is composed of one projector as transmitter and one projector as receiver. By projecting sinusoidal fringe patterns onto the object and measuring the distortion level of the patterns in the fringe analysis, the system can accurately reconstruct the 3D geometry of the object. Based on the captured images with fringe patterns, the system can ascertain the correspondence between the camera pixels and projector pixels one-by-one, which is key for 3D reconstruction. If the triangulation relationship between two optical devices and the object is accurately set, the system can reconstruct the 3D geometry accurately. However, under the unstructured environments, it is difficult to match corresponding pairs accurately because the sensors are disturbed by external factors. In order to reduce noise and make the system more robust, this research aims to develop a method to use the depth range that the system can measure as a constraint in calculating the 3D information. The system would be able to retrieve the 3D geometry within the range more accurately and more robustly. The details of this research are introduced in Chapter 3.

- **Develop a method to increase 3D scanning speed.**

  For the standard DFP system, converting the domain of captured images from texture to phase is the most important procedure for 3D reconstruction. One of the most common ways to retrieve the phase is through accumulating a set of captured images. This means that the number of patterns is an important factor to determine the speed of 3D reconstruction because the patterns are captured by a camera sequentially; in other words, the number of patterns is proportional to the time taken to capture a set of images for one 3D image. This dissertation research aims to reduce the number of patterns required in high-speed 3D sensing. By integrating texture image of the object with an existing fringe analysis method, the required number of fringe patterns for 3D reconstruction can be reduced.

  The other challenge of high-speed 3D shape measurement for the DFP system is that the projector utilizes 8-bit grayscale patterns to project sinusoidal fringe patterns. However, the grayscale projection requires that the system be precisely synchronized and do gamma calibration to compensate for nonlinear effect. This dissertation research tries to maximize the projection speed by defocusing the projector lens and using binary patterns instead of 8-bit patterns. The geometric constraints can also be used for 3D reconstruction to increase the accuracy of the 3D reconstruction algorithm. The details of this research are introduced in Chapters 4 and 5.

- **Develop a custom-designed mechanical projector for high-speed and high-accuracy 3D surface measurement and broad-light spectrum.**

  The DLP projector, which is widely used in the DFP system, has digital mirror devices (DMD) to project a pattern(s) pixel by pixel. Micro mirrors inside the DLP projector are made of a silicon-based material, which reflects only a specific range of light spectrum, thereby limiting the light spectrum that can be used for 3D sensing in the DFP system. Furthermore, the DLP projector has a speed limitation for projecting gray-scale patterns needed for fringe analysis. This research focuses on developing a new custom-designed projector, which may overcome the light spectrum and speed limitation of the conventional DLP projector. In order to tackle this issue, the current research places the source of the light for projection independently and develops a projection mechanism with a mechanical device, such as direct current (DC) motor. The details of this research are discussed in Chapter 6.

- **Compare the performance of the DLP projectors typically used for 3D reconstruction under ultra-resolution 3D shape measurement.**

  There are two types of DMD used in the DLP projectors: diamond-shaped pixels, and rectangular-shaped pixels. However, when the camera pixel size is much smaller than the projector, in order to achieve ultrahigh resolution 3D shape measurement, we found that the diamond-shaped DMD pixels cannot be used to achieve high-quality 3D shape measurement. We believe that this is caused by the sampling effect of mismatched pixel shape from the computer-generated pixel and the projected pixel. This research focuses on the performance of the DFP system for ultrahigh resolution 3D shape measurement using two different types of projectors with a camera pixel size being much smaller than the projector pixel size in object space. The details of this research are discussed in Chapter 7.

1.3 Dissertation organization

The rest of the dissertation is organized as follows. In Chapter 2, we explain various types of sensors for unstructured environments and the configuration of sensors for each example. In Chapter 3, we introduce a novel absolute phase unwrapping method, which reduces noise compared to the existing methods. In Chapter 4, we introduce an absolute phase-retrieval method, which uses only five binary patterns and thereby increases the speed of 3D sensing. In Chapter 5, we introduce a novel method for the absolute phase-retrieval using only three binary patterns. In Chapter 6, we explain a novel method that enables us to utilize a broad-light spectrum and enables superfast 3D sensing by customizing a new type of mechanical projector. In Chapter 7, we compare the performance of two different projectors often used in 3D reconstruction, and in Chapter 8, we outline the proposed work for this dissertation.

2. RELATED WORK

With the development of sensor technology, new types of sensors have been released. Many sensors, except for ultrasonic sensor, utilize electromagnetic signal in different frequencies to detect the environment and measure the geometries of objects. Proper sensors should be configured depending on the environments measured. In this section, we discuss various sensors used for recognizing the surrounding environments and state-of-the-art sensing technologies.

2.1 Lidar

Lidar, an acronym of light detection and ranging, is one of the essential sensors for mapping because it has relatively high resolution in 3D and long-range detecting by using laser. The lidar uses time-of-flight (TOF), which measures the time difference between the moment of sending a signal and the moment of receiving the signal from the target and calculating the distance by multiplying the speed of light. For mobile applications, NIR lasers ranging from 780 nm to 2500 nm are most common because the lights are invisible and a high-frequency laser can harm the human eye. Lidar sensors have been used extensively in robotics, construction, and autonomous vehicles. For autonomous vehicles, the lidar typically generates a 3D map by rotating the system 360 degrees, as shown in Fig. 2.1(a). Figure 2.1(b) shows an example of autonomous vehicle that has a lidar on top of the vehicle, and Fig. 2.1(c) shows a 3D map generated by the lidar. Even if the lidar succeeded in making a long-range and real-time 3D map, the sensor has still fused with other camera-based sensors such as stereo vision camera and RGB-D sensor in real applications because the number of point clouds is not enough for object classification or image segmentation, and there is no color information on the 3D data.

(a) (b) (c)

Fig. 2.1. (a) An image of Velodyne HDL-64E lidar[1]; (b) an image of lidar attached on top of a car[2]; (c) lidar data set at a moment[3].

Commercial solid-state lidar units have been developed, which utilize optical phased array technology to steer the laser beam instead of rotating the system [20] as shown in Fig. 2.2(b). Replacing the rotating mechanism of lidar with a million individual micro-scale emitters helps lower the cost and increase accessibility to the people. However, to scan the surrounding environments in 360 degrees, integrating several lidar sensors is required because of the angle the sensor can scan, as shown in Fig. 2.2(c). In addition, other types of sensors are still required to recognize the surrounding object in localization and mapping. For example, to localize the vehicle in the generated 3D map, GPS and Inertial Measurement Units (IMUs) are typically integrated with the 3D data by lidar. However, GPS signal is not accurate in urban areas because of the interference of signals, and IMUs can provide only the current mechanical state of the vehicle. By accumulating the signals from IMUs, the vehicle can get help localizing itself, but there is an inherent error: drift. In addition, the lidar is not sufficient for recognizing environmental features such as lane markers and curbs, as seen in Fig. 2.1(c).

[1] `https://velodynelidar.com/hdl-64e.html`

[2] `https://atmelcorporation.wordpress.com/2015/09/08`

[3] `https://www.cnet.com/roadshow/news/how-lasers-map-the-world-for-self-driving-cars`

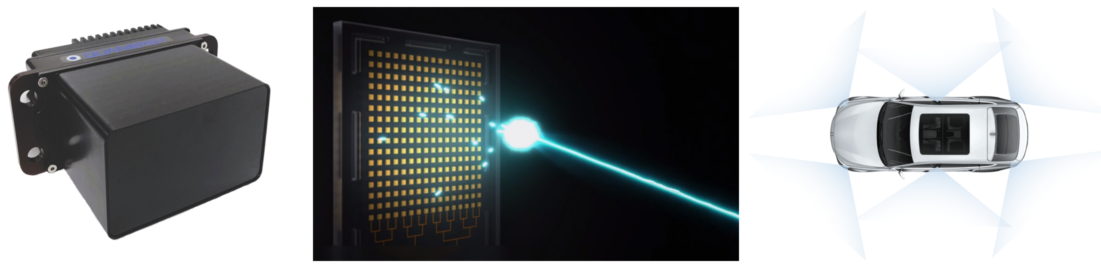

(a) (b) (c)

Fig. 2.2. (a) An illustration of how the solid-state lidar sensor works[1];(b) a schematic diagram of using multiple solid-state lidar units[2]; (c) a illustration of scanning area that each solid-state lidar sensor can see

2.2 Radar

Radar, an acronym of radio detection and ranging, is a system for detecting objects and measuring their location with electromagnetic radiation [21]. Even though the system cannot recognize the color of objects or receive detail information, the system consistently performs the measurement in harsh conditions such as darkness, haze, fog, rain, and snow. For this reason, from autonomous vehicles to space surveillance, the radar system has been extensively used to detect surrounding objects. The system consists of one emitter and one receiver to detect the reflected signal. For radar sensors used in mobile platform such as autonomous vehicles and service robots, the sensors can be classified, depending on the range the sensor can detect. Long-range radar typically detects objects at a distance of up to 250 m, and mid-range radar detects an object at a distance of up to 30 m [22].

2.3 Vision-based 3D shape measurement technologies

For a few decades, high-speed and high-accuracy 3D shape measurement techniques have been used extensively in medicine, manufacturing, and even entertain-

[1] `https://quanergy.com/s3`

[2] `https://www.youtube.com/watch?v=n3S8Io0kZZs`

ment. Additionally, a lot of companies have successfully commercialized 3D sensor modules, such as Microsoft Kinect, Intel RealSense, and Orbbec Astra, as shown in Fig. 2.3, and major cell phone manufacturers have tried to put 3D techniques into their cell phone devices for security and entertainment [4].

(a) (b) (c)

Fig. 2.3. Commercial 3D cameras. (a) Microsoft Kinect[1]; (b) Intel RealSense[2];(c) Orbbec Astra[3].

The two major categories of vision-based 3D imaging technologies are the passive and the active methods. The passive methods do not use any illumination devices to obtain 3D images. The methods only utilize the reflected light from the object to be measured. Standard stereo vision is one of the most widespread and direct methods to reconstruct 3D. Figure 2.4 shows the typical setting of standard stereo vision. There are several advantages of using the stereo-vision for 3D reconstruction. First, it is easy to implement because only cameras are used to retrieve 3D image. Second, it is appropriate for high-speed 3D shape measurement because only a pair of images at the different perspectives are required to reconstruct one 3D image. Therefore, the speed of getting 3D images is the same as the speed of capturing images with the cameras.

From the captured images, the processor finds corresponding pairs of the images by calculating the correlation. Based on the corresponding-pair information, the processor can facilitate 3D reconstruction with triangulation [23, 24]. If the processor

[1] https://en.wikipedia.org/wiki/Kinect

[2] https://www.intelrealsense.com

[3] https://orbbec3d.com

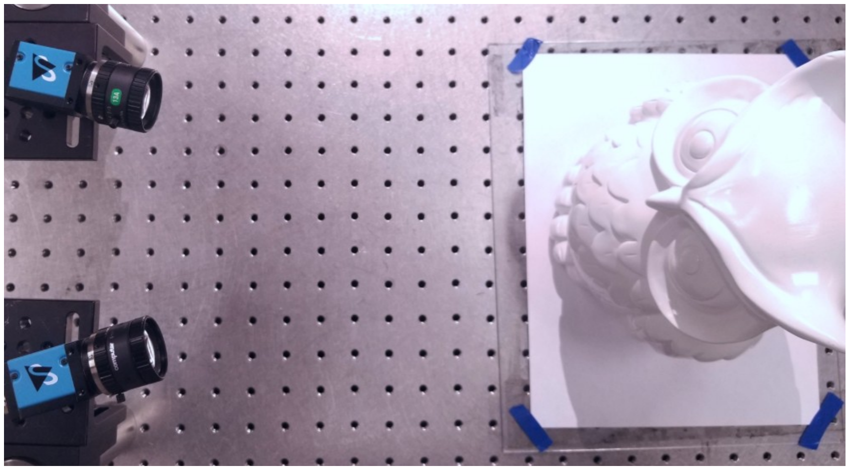

Fig. 2.4. A typical setting of standard stereo vision

tries to find the correspondence by comparing two images from the start, the computational cost is high. To mitigate the problem, the concept of *epipolar geometry* is applied and described in Fig. 2.5. O represents the focal point for the camera and the superscripts ^{l} and ^{r} describe the left camera and the right camera respectively. E^l and E^r are the intersection points between the line $\overline{O^lO^r}$ and the two captured images, which are called as *epipoles*. For example, a pixel P^l has many candidates such as P_1, P_2, and P_3 and one of them should be the corresponding point, depending on the depth in a 3D space. Even though all candidates has different depth information, all these points should be on the same line L^r, which is called *epiploar line*. By applying the same geometric conditions to other points on L^l, every point on the line L^l must correspond to a point on the line L^r. Then, the *epipolar plane* is formed by P^l, O^l, and O^r. The processor simplifies the algorithm to find the corresponding points by searching it based on the epipolar line.

To speed up the procedure of finding corresponding pairs, *image rectification*, which makes the epiploar lines on the same row, is required. With the use of rotation and translation matrices indicating the relationship between two cameras, the images from two cameras can be modified in the direction of aligning epipolar lines. Before rectifying both images, the epipolar lines are not aligned on the same row. By using

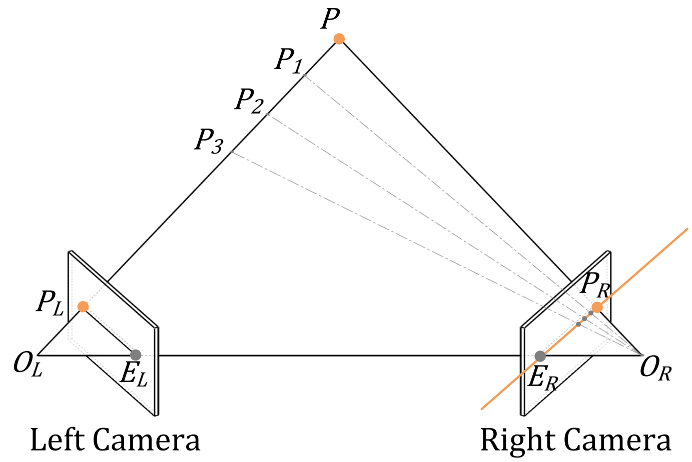

Fig. 2.5. A schematic diagram of epipolar geometry

the calibration data of two cameras, we can obtain the rectified images as shown in Fig. 2.6. As the green horizontal lines shows, it makes the processor easier to find the corresponding points by comparing the pixel value within the horizontal line.

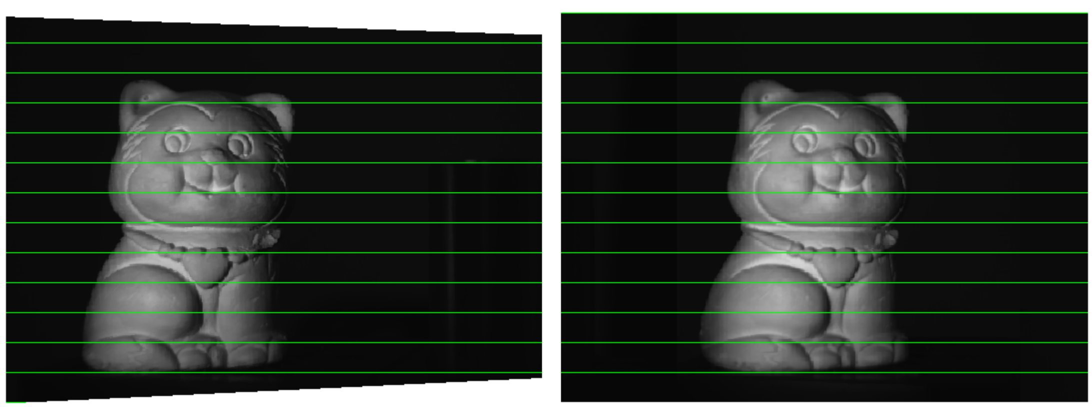

Fig. 2.6. A pair of rectified images for stereo matching, horizontal green lines show representative epipolar lines

Based on the epipolar geometry and the image rectification, numerous algorithms for stereo matching have been developed. Based on the way of the optimization, the algorithms can be classified into two categories: local stereo matching algorithms [25–27] and global stereo matching algorithms [28, 29].

Even if the algorithm reduce the computational work significantly and new-released algorithms speed up the calculation speed effectively, there are inherent limitations in resolution and accuracy. The standard stereo-vision methods rely on the texture value of the images; therefore, if the system tries to reconstruct a 3D image of a flat, white plane, the algorithms may fail to find the correspondence.

On the other hand, the active methods have at least one light emitter to project light to the object to facilitate 3D reconstruction. By using the preset patterns, the processor can easily find the correspondence pairs between optical devices and increase the accuracy and the resolution of the measuring system. The configuration of optical devices could be different, depending on the patterns used for 3D reconstruction. For example, an IR emitter can be used to compensate for the limitations of the standard stereo vision by projecting a statistical pattern on an object. Even if the object to be measured does not have enough feature points for standard stereo vision, the processor already has the information of the pattern and calculates the corresponding pairs quickly and accurately. The statistically random patterns have been successfully adopted in commercial 3D sensors such as Microsoft Kinect V1, Intel RealSense R200, and iPhone X. Figure 2.7 shows the patterns used in these commercial 3D sensors [4]. The advantage of using these random patterns is to achieve relatively higher accuracy and higher resolution than what the standard stereo vision can achieve. Because of the simple-hardware setting, the sensors can be miniaturized easily and commercialized inexpensively. However, these active methods with statistical random patterns to reconstruct 3D images also have the fundamental limitations for high-accuracy and high-resolution 3D shape measurement. The projected light can be interfered with another light source. In other words, the system is sensitive to noise. Additionally, a feature point of the projected pattern on the object takes more than one camera pixel. Therefore, the system standardizes the spatial resolution of the system downward, even if the corresponding pairs can be matched by using the correlation method.

To overcome the limitation in spatial resolution and enhance the accuracy of the measuring system, researchers have used fringe projection techniques in 3D shape

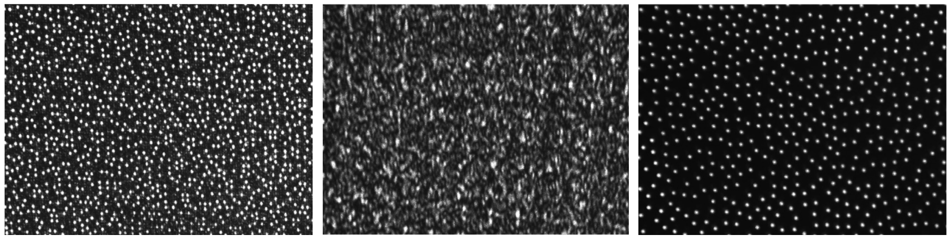

(a) (b) (c)

Fig. 2.7. Statistically random patterns used in commercial 3D sensors. Patterns used in (a) Microsoft Kinect; (b) Intel RealSense; and (c) Apple iPhoneX.

measurement. Instead of using the intensity of surface texture, the processor finds corresponding pairs by searching in *phase domain*, which is continuous and uniquely defined in both horizontal and vertical directions. The patterns for obtaining the phase information repeat changing from black to white gradually for each period, as shown in Fig. 2.8. These are called *fringe patterns* or *sinusoidal structured patterns.*

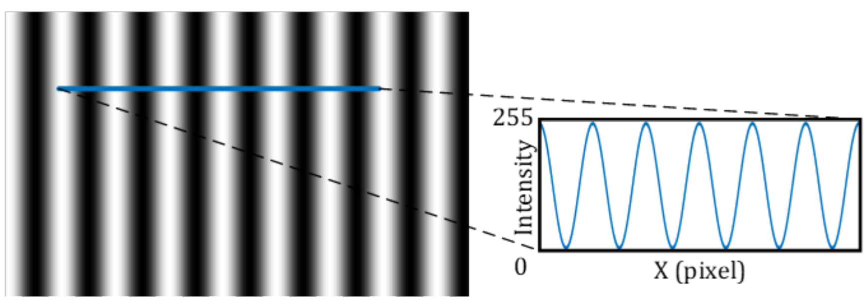

Fig. 2.8. A schematic diagram of a DFP setup

Because the system typically includes at least one digital video projector, the technology is referred to as the *digital fringe projection* (DFP) technique. Fig. 2.9 illustrates the relationship between an object(s) to be measured and the DFP system, including one camera and one projector. When the fringe patterns are projected on the object, the fringes are distorted depending on the geometry of the object. If the object has a flat surface, a distortion of the patterns rarely occurs. Otherwise, if the object has some curves or a rough surface, the stripes on the patterns are distorted. By capturing the distorted patterns on the object, we can calculate the phase information used for 3D reconstruction.

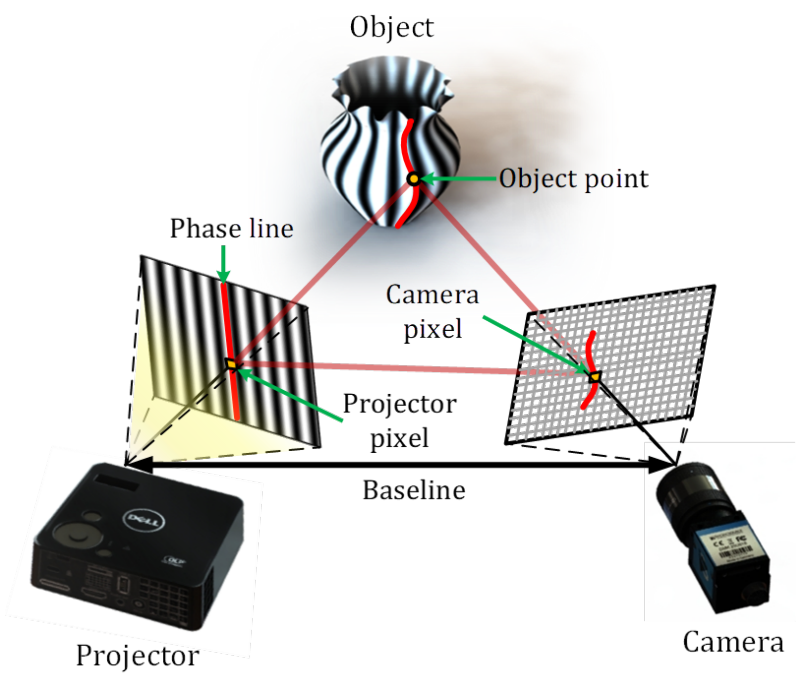

Fig. 2.9. A schematic diagram of a DFP setup

There are many methods related to retrieving the phase from the fringe images. Fourier Transform Profilometry (FTP) is one of the methods for phase retrieval, which utilizes frequency domain to extract the phase information. The FTP-based methods have the merit of high-speed 3D reconstruction because, theoretically, only one image is required to retrieve phase [30,31]. Despite the advantage, the method is very sensitive to noise and surface texture variation. Therefore, many FTP methods using an additional one or more patterns have been developed [32,33]. Still, the FTP methods are mainly adopted to measure relatively smooth surfaces or the object that has not much difference in depth. Instead of the FTP methods, phase-shifting profilometry (PSP) is widely used in 3D shape measurement because of high accuracy, high-spatial resolution, and robustness to noise [34].

The fringe pattern can be mathematically described as,

$$I(x,y) \quad = \quad I'(x,y) + I''(x,y)\cos[\phi(x,y)], \tag{2.1}$$

where $I'(x,y)$ is the average intensity, $I''(x,y)$ the intensity modulation, and $\phi(x,y)$ the phase to be solved for. The fringe patterns for PSP can be described as,

$$I_k(x,y) \quad = \quad I'(x,y) + I''(x,y)\cos[\phi(x,y) - \delta_k], \tag{2.2}$$

where the subscript k means the k-th fringe image, and δ indicates the phase shift. After capturing k images from the camera, the phase can be solved as,

$$\phi(x,y) = -\tan^{-1}\left[\frac{\sum_{k=1}^{N} I_k(x,y)\sin\delta_k}{\sum_{k=1}^{N} I_k(x,y)\cos\delta_k}\right]. \tag{2.3}$$

By the inherent properties of inverse tangent function, the phase ranges from $-\pi$ to π. It means that the phase value for each pixel repeats every period. We often called the phase a *wrapped phase*. To uniquely define the phase value along one axis, phase unwrapping is essential for 3D reconstruction. To unwrap the wrapped phase, we need to add or multiple integer numbers of 2π. The number 2π added for each pixel is referred to as *fringe order*. As a result, the process of determining the fringe order is the phase unwrapping [35]. Numerous phase unwrapping algorithms has been developed recently. We can classify the algorithms into two large groups: spatial phase unwrapping algorithms and temporal phase unwrapping algorithms.

Spatial phase unwrapping algorithms utilize the phase value of surrounding points in the same phase map through a local or global optimization [36–38]. The algorithms assume that the phase map is connected continuously. However, if the difference in phase value is larger than 2π—which means that there is a radical depth change, or objects to be measured are isolated—then it is very challenging to determine correct fringe order.

On the other hand, temporal phase unwrapping algorithms determine the fringe order by capturing additional images. The most representative algorithm is the binary coding method, or encoding the fringe order into a set of binary patterns. Mixing with the phase-shifting method, the method is often called a *hybrid* method [39]. Fig. 2.10 illustrates how the binary coding method unwrap the wrapped phase. Furthermore, more algorithms related to encode the codeword for the fringe order into the patterns have been developed [40, 41].

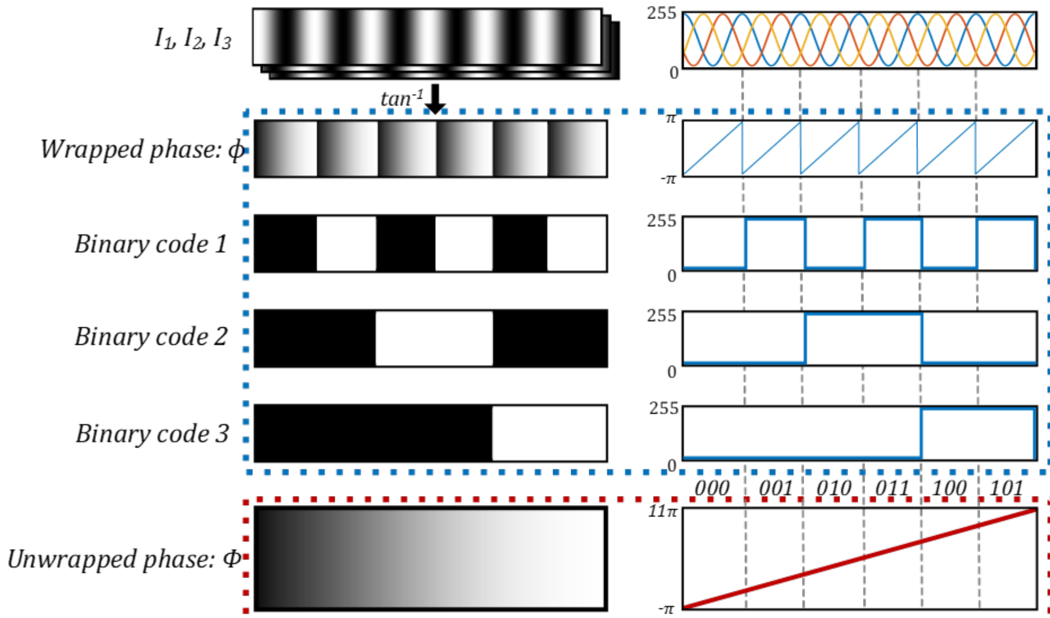

Fig. 2.10. A schematic diagram of binary-coding unwrapping algorithm

Another temporal phase unwrapping algorithm is to utilize multi-frequency for fringe patterns [42]. Two or more sets in different fringe densities of patterns are used for phase unwrapping. If we set fringe period T as the number of pixels in a period of fringe pattern, then the equivalent fringe period T_{eq} can be calculated as,

$$T^{eq} = \frac{T_1 T_2}{|T_1 - T_2|}, \tag{2.4}$$

where T_1 and T_2 are fringe periods for two different frequencies. Then, we can calculate equivalent phase ϕ_{12} for two period, by using

$$\phi_{12} = [\phi_1 - \phi_2] \bmod (2\pi), \tag{2.5}$$

where ϕ_1 and ϕ_2 are phases corresponding to T_1 and T_2 respectively. After calculating multiple phase maps in different frequencies, the equivalent phase which covers the whole projection pattern becomes the *absolute* phase Φ_{eq} which is the final result of integrating all phase maps with Eq. (2.5) as,

$$\Phi_{eq}(x, y) = \phi_{eq}(x, y). \tag{2.6}$$

If only two frequencies are used, ϕ_{eq} is equal to ϕ_{12}. The fringe order k for phase unwrapping can be determined by the precalculated equivalent phase map Φ_{eq} and

$$k(x, y) = \frac{\Phi_{eq}(x, y) \times T_{eq}/T_1 - \phi_1}{2\pi}. \tag{2.7}$$

Because we can obtain the fringe order after calculating the equivalent phase map, the method is often referred to as backward phase unwrapping. The more frequencies fringe patterns have for projection, the less influence of noise the 3D image can be obtained with [43]. Therefore, more than two frequencies are desirable for the robustness of 3D reconstruction. However, for high-speed 3D sensing experiments, utilizing more than two-frequency fringe patterns slows down the speed of 3D reconstruction because the number of frequencies is proportional to the number of fringe patterns for projection to obtain one 3D image [44]. To reduce the number of fringe patterns for one 3D image, An et al. developed a method of using the relationship between the phase value and the 3D coordinate inversely as *geometric-constraints* [45]. By setting an imaginary depth range to be measured and referring the phase value of the imaginary boundaries, the methods can automatically unwrap the phase; thus, it is more suitable for high-speed application. With high-frequency fringe patterns, the system can obtain high-accurate and high-speed 3D shape measurement results.

In the meantime, other researchers have tried to add at least one more optical device to the standard DFP system [46–48]. They developed the DFP systems with two cameras and one DLP projector. The system reconstructed the 3-D model of the object with fringe patterns and a statistical pattern to use the benefits of standard stereo vision and DFP techniques. Instead of using two cameras, a multi-view DFP system was built using mirrors [49]. Because the standard DFP system can reconstruct only the 3-D geometry that the optical devices can see, the loss of data occurs for the occluded area of the object. By setting the mirrors to make the system see the occluded area, the system reconstructed the 3-D geometry of the occluded area, which means that the 360-degree 3D model was achieved.

3. ENHANCED TWO-FREQUENCY PHASE-SHIFTING METHOD

3.1 Introduction

High-speed and high-accuracy three-dimensional (3D) shape measurement is of great interest to numerous applications including in-situ quality control in manufacturing and diseases diagnosis in medical practices.

Among all 3D shape measurement techniques developed, phase-based methods using fringe analysis techniques uniquely stand out due to their measurement speeds and accuracy. Retrieving phase from a sequence of phase-shifted fringe patterns is one of most popular methods since they can recover phase for each point, are less sensitive to surface reflectivity variations etc. Typically, the phase directly obtained from fringe patterns can only provides phase value ranging from $-\pi$ to $+\pi$, and a phase unwrapping algorithm has to be adopted to recover a continuous phase map. Phase unwrapping can be classified into spatial and temporal phase unwrapping categories. The spatial phase unwrapping determines 2π discontinuous locations from the phase map itself and adds or subtracts multiple number of 2π accordingly. Numerous phase unwrapping algorithms have been developed with some being fast but less robust and some being robust but slow; and the principles and various spatial phase unwrapping algorithms have been summarized in Book [36]. Among those spatial phase unwrapping algorithms, the popular ones are reliability-guided phase unwrapping algorithms since they tend to be robust. Different reliability-guided phase unwrapping algorithms have be reviewed in Reference [50]. Regardless the robustness of any spatial phase unwrapping algorithms, they typically only generate a *relative* phase map that is relative to a point for each connected component. Therefore, 3D reconstructed shape using a spatial phase unwrapping usually only provides relative geometry to that point instead of absolute geometry. Furthermore, the majority spatial phase unwrapping algorithms fail if abrupt surface changes introduce more than 2π phase changes from one point to the next point.

Temporal phase unwrapping, in contrast, tries to fundamentally eliminate the problem of spatial phase unwrapping by capturing more images. And one of the popular methods is to use multi-frequency (or wavelength) phase-shifting techniques [43, 51, 52], where fringe patterns with different fringe periods are used to generate equivalent phase map, ϕ^{eq}. If the equivalent phase map ranges from $-\pi$ to π covers the whole range of surface, no phase unwrapping is necessary and thus ϕ^{eq} can be regarded as the unwrapped phase, or $\Phi^{eq} = \phi^{eq}$. Φ^{eq} can then be used to determine fringe order for each point on the high-frequency phase for temporal phase unwrapping.

Multi-frequency phase unwrapping algorithms were developed for laser interferometry systems. Due to the flexibility of digital fringe projection (DFP) techniques, more temporal phase unwrapping algorithms have been developed including gray-coding plus phase-shifting methods [53, 54], spatial coding plus phase-shifting method [55], and phase-coding plus phase-shifting methods [56–58]. Comparing to the two-frequency phase-shifting based temporal phase unwrapping method, the gray-coding methods typically requires more than three additional binary patterns to determine fringe orders; and the method of spatial coding requires the knowledge of neighborhood pixel information, and could fail if the surface is not locally smooth; and phase-coding methods only need three additional fringe patterns, yet it is difficult to differentiate the encoded fringe orders if the noise is large that is the same problem as conventional two-frequency phase-shifting methods.

It is desirable for high-speed applications to use less number of fringe patterns to reconstruct one 3D frame, and thus two-frequency phase-shifting algorithm is preferable. Yet, large noise could completely fail the fringe order determination, as thoroughly discussed by Creath [59]. Conventionally, multi-frequency phase-shifting algorithms are often used in lien of the two-frequency phase-shifting algorithm for applications where noise is severe. This chapter proposes a method to enhance the robustness of the two-frequency phase-shifting method yet not to increase the number of patterns captured. In lien of using more patterns, this proposed method uses geometric constraints of DFP system to reduce the noise impact by allowing the use of more than one period of equivalent phase map to determine fringe order. Experiments demonstrated that noise impact on phase unwrapping can be reduced by a factor of 4 or even higher.

Section 3.2 explains the principles of the proposed out-of-focus camera calibration method. Section 3.3 shows some simulation results to validate the proposed method. Section 3.4 presents experimental results to further validate the proposed method. Lastly, Section 3.5 summarizes the paper.

3.2 Principle

This section thoroughly explains the principle of the proposed two-frequency phase-shifting method. Specifically, we will present the basics of two-frequency phase-shifting algorithm, details the minimum phase generation using geometric constraints of the calibrated DFP system; and explains how to use the minimum phase to enhance the two-frequency phase-shifting method.

3.2.1 Two-frequency phase-shifting algorithm

As aforementioned, phase-shifting algorithms are extensively used in optical metrology. Over the years, numerous phase shifting algorithms have been developed including three step, four step and least squares [60]. For high-speed applications, a three-step phase-shifting algorithm is desirable since it uses the minimum number of patterns to recover phase. For a three-step phase-shifting algorithm with equal phase shifts, three fringe images can be mathematically described as,

$$
\begin{aligned}
I_1(x,y) &= I'(x,y) + I''(x,y)\cos(\phi - 2\pi/3), && (3.1)\\
I_2(x,y) &= I'(x,y) + I''(x,y)\cos(\phi), && (3.2)\\
I_3(x,y) &= I'(x,y) + I''(x,y)\cos(\phi + 2\pi/3). && (3.3)
\end{aligned}
$$

Where $I'(x,y)$ is the average intensity, $I''(x,y)$ is intensity modulation, and ϕ is the phase to be solved for. Solving (3.1)–(3.3) simultaneously leads to

$$\phi(x,y) = \tan^{-1}\left[\frac{\sqrt{3}(I_1 - I_3)}{2I_2 - I_1 - I_3}\right]. \qquad (3.4)$$

The phase obtained from (3.4) ranges from $-\pi$ to π with 2π discontinuities, and this phase is called wrapped phase. The process of removing 2π discontinuities to obtain a continuous phase map is called phase unwrapping. As discussed in Sec. 3.1, there are two types of phase unwrapping methods: spatial and temporal with spatial algorithms being limited to smooth and continuous phase reconstruction and temporal algorithms being more general but requires additional information.

One of the temporal phase unwrapping methods is to use multi-frequency phase-shifted fringe patterns, where fringe patterns with different fringe periods are used to generate equivalent phase map, ϕ^{eq}. If the equivalent phase map ranges from $-\pi$ to π for the whole surface, no phase unwrapping is necessary. Therefore, ϕ^{eq} can be regarded as unwrapped phase $\Phi^{eq} = \phi^{eq}$. Φ^{eq} can be used to determine fringe order for each point on the high-frequency phase for temporal phase unwrapping. For high-speed measurement, a two-frequency phase-shifting algorithm is preferable comparing to three- or more-frequency phase shifting algorithms since it uses less number of images for 3D reconstruction.

From two-frequency phase-shifted fringe patterns, one can obtain two wrapped phase maps $\phi^1(x,y)$ and $\phi^2(x,y)$. The equivalent phase map can be computed as

$$\phi^{eq}(x,y) = \phi^1(x,y) - \phi^2(x,y) \mod 2\pi, \qquad (3.5)$$

here mod is the modulus operation. If the equivalent phase, ϕ^{eq}, does not have any 2π discontinuities, it can be regarded as unwrapped phase Φ^{eq} and be used to unwrap $\phi^1(x,y)$ and $\phi^2(x,y)$ pixel by pixel.

For a DFP system, the frequency of a fringe pattern is actually defined as $1/T$, where T is fringe period in pixel. If the fringe periods used for a two-frequency phase-shifting algorithm are T^1 and T^2, it is straightforward to prove that the equivalent fringe period to generate the equivalent phase is

$$T^{eq} = \frac{T^1 T^2}{T^2 - T^1}, \tag{3.6}$$

assuming $T^2 > T^1$.

Therefore, the condition to use two-frequency phase shifting algorithm for temporal phase unwrapping is that T^{eq} is the whole projection range. In such a case, the fringe order for high frequency $1/T^1$ can be determined by

$$K(x,y) = Round\left[\frac{\phi^{eq}(x,y)\frac{T^{eq}}{T^1} - \phi^1(x,y)}{2\pi}\right], \tag{3.7}$$

to temporally unwrap $\phi^1(x,y)$ by

$$\Phi^1(x,y) = \phi^1(x,y) + K(x,y) \times 2\pi. \tag{3.8}$$

Here *Round()* is to round a floating point number to its closest integer number, and $\Phi^1(x,y)$ is the unwrapped phase of $\phi^1(x,y)$.

The two-frequency phase unwrapping algorithm discussed above works in principle, yet has two major limitations:

1. *Limited frequency choice.* It is well known that using higher frequency (or smaller T) fringe patterns can generate accurate phase, and thus it is preferable to use smaller T for higher accuracy 3D shape measurement. However, the two-frequency phase-shifting algorithm limits its choices. For example, if a three-step phase-shifting algorithm is used, it is preferable to use a fringe period of $n \times 3$ pixels (here n is an integer) to avoid phase shift error. Based on this constraint, in order to generate $T^{eq} = 1024$ pixels, the smallest fringe periods

to use are $T^1 = 54$ pixels and $T^2 = 57$ pixels, which are very large comparing to the desired value of around 30 pixels.

2. *Large noise impact.* From (3.7), one may notice that the equivalent phase ϕ^{eq} is scaled up by a scaling factor of T^{eq}/T^1 to determine fringe order $K(x, y)$. It is important to note that the noise in ϕ^{eq} is also proportionally scaled up by a factor of T^{eq}/T^1. This scaled noise could lead to incorrectly determine fringe order, $K(x, y)$. For example, if the phase noise is 0.2 rad, a scaling factor of 18 could lead to incorrect fringe orders.

Due to the flexibility of digital fringe pattern generation, the DFP methods mitigate the former limitation by directly projecting the equivalent frequency fringe patterns that one single fringe covers the whole projection range (e.g., $T^2 = T^{eq} = 1024$ pixels for a projector resolution of 1024×768) and then use $\phi^2(x, y) = \phi^{eq}(x, y)$ to unwrap ϕ^1. By doing so, it allows the use of higher frequency fringe patterns (e.g., $T^1 = 30$ pixels). The consequence of using such approach is that the noise problem could be amplified since the scaling factor T^{eq}/T^1 could be even larger. For example, if $T^2 = 1024$ and $T^1 = 30$ pixels, the scaling factor is 34; and the phase noise larger than 0.1 rad for a point can lead to a wrong fringe order. As a result, the two-frequency phase-shifting method is not very appealing to practical applications, and three or more frequency phase-shifting algorithms are more extensively used.

One may realize that the fundamental problem associated with the aforementioned two-frequency phase-shifting algorithm is its requirement of T^{eq} is large enough to cover the whole measurement range; and if this strong requirement is relaxed, the two-frequency phase-shifting algorithms could be substantially enhanced.

In this research, we propose to use the geometric constraints of DFP systems to improve the performance of two-frequency phase-shifting algorithms. To understand such an approach, we will introduce the mathematical model of DFP system and how to use such a model to setup constraints for temporal phase unwrapping such as smaller T^{eq} can be used.

3.2.2 DFP system model

In this research, we use a well-known pinhole model to describe an imaging lens. This model essentially describes the relationship between 3D world coordinates (x^w, y^w, z^w) and its projection onto a 2D imaging coordinates (u, v). The linear pinhole model can be mathematically described as,

$$s \begin{bmatrix} u \\ v \\ 1 \end{bmatrix} = \mathbf{A} \begin{bmatrix} \mathbf{R} & \mathbf{t} \end{bmatrix} \begin{bmatrix} x^w \\ y^w \\ z^w \\ 1 \end{bmatrix}. \tag{3.9}$$

Where,

$$\mathbf{R} = \begin{bmatrix} r_{11} & r_{12} & r_{13} \\ r_{21} & r_{22} & r_{23} \\ r_{31} & r_{32} & r_{33} \end{bmatrix}, \tag{3.10}$$

$$\mathbf{t} = \begin{bmatrix} t_1 \\ t_2 \\ t_3 \end{bmatrix}, \tag{3.11}$$

$$\mathbf{A} = \begin{bmatrix} f_u & \gamma & u_0 \\ 0 & f_v & v_0 \\ 0 & 0 & 1 \end{bmatrix}, \tag{3.12}$$

respectively represents the rotation $\mathbf{R}$ and the translation $\mathbf{t}$ from the world coordinate system to the lens coordinate system; and the projection $\mathbf{A}$ from the lens coordinate system to the 2D image coordinate system. s is a scaling factor; f_u and f_v are the effective focal lengths; γ is the skew factor of u and v axes, and for modern cameras $\gamma = 0$; and (u_0, v_0) is the principle point, the intersection of the optical axis with the imaging plane.

For simplicity, let us define the projection matrix $\mathbf{P}$ as

$$\mathbf{P} = \mathbf{A}\begin{bmatrix} \mathbf{R} & \mathbf{t} \end{bmatrix} = \begin{bmatrix} p_{11} & p_{12} & p_{13} & p_{14} \\ p_{21} & p_{22} & p_{23} & p_{24} \\ p_{31} & p_{32} & p_{33} & p_{34} \end{bmatrix}, \tag{3.13}$$

which can be estimated from calibration.

The same lens model is applicable to both the projector and the camera, and the only difference is that the projector is the inverse of a camera. Therefore, if the camera and the projector are calibrated under the same world coordinate system, we have

$$s^p \begin{bmatrix} u^p & v^p & 1 \end{bmatrix}^t = \mathbf{P^p} \begin{bmatrix} x^w & y^w & z^w & 1 \end{bmatrix}^t, \tag{3.14}$$

$$s^c \begin{bmatrix} u^c & v^c & 1 \end{bmatrix}^t = \mathbf{P^c} \begin{bmatrix} x^w & y^w & z^w & 1 \end{bmatrix}^t, \tag{3.15}$$

Here superscript ^{p} represents projector, superscript ^{c} presents camera, and superscript ^{t} represents transpose of a matrix. After calibration, $\mathbf{P^p}$ and $\mathbf{P^c}$ are known.

3.2.3 Temporal unwrapping use minimum/maximum phase maps

For any given calibrated DFP system, the calibration volume is well known, which defines minimum z, z_{min} and maximum z, z_{max}.

From (3.15), if z^w is known, for any given pixel (u^c, v^c), coordinates x^w and y^w can be uniquely solved. Once (x^w, y^w, z^w) coordinates of a given point (u^c, v^c) are known, its corresponding point on the projector (u^p, v^p) can be computed using (3.14). Because the phase on the projector is well defined for any given pixel (even multiple fringe periods), the camera phase map can be built for a given z^w value, and such a phase map does not have any 2π ambiguities. Therefore we can create two phase maps Φ_{min} and Φ_{max} that respectively corresponds to z_{min} and z_{max}.

Figure 3.1 illustrates the basic concepts of using minimum phase, Φ_{min}, to correct 2π discontinuities. Assume the region on the projector that a camera captures at $z = z_{min}$ is shown in the red dashed window, the phase directly obtained from three-phase-shifted fringe patterns has one 2π jump, ϕ_1, as shown in Fig. 3.1(a). However, since such phase is well defined on the projector, the Φ_{min} can be obtained, which is a continuous phase on the projector space, as shown in Fig. 3.1(b). The cross sections of the phase maps are shown in Fig. 3.1(c). This example shows that if the wrapped phase is below Φ_{min}, 2π should be added to the phase to unwrap it. One may also notice that even if the phase is obtained at z_{max}, the condition of adding 2π to ϕ_2 is still the same: when $\phi_2 < \Phi_{min}$.

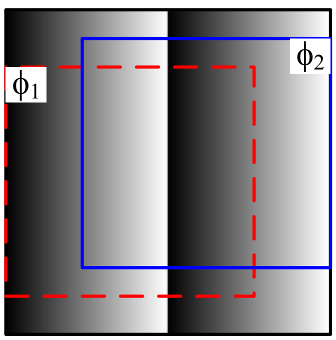

(a)

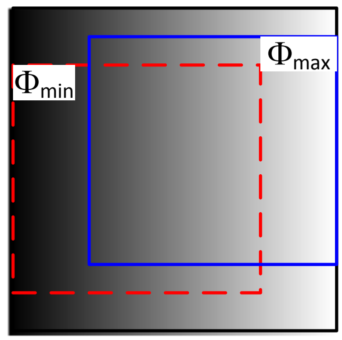

(b)

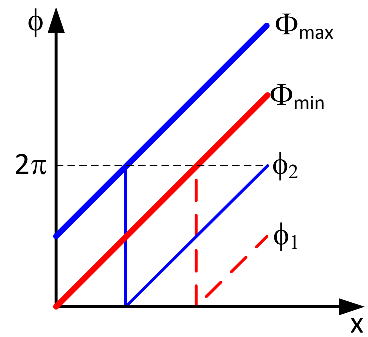

(c)

Fig. 3.1. Conceptual idea of removing 2π jumps of low-frequency phase map by using the minimum phase map determined from geometric constraints. (a) Windowed regions shows phase map that acquired by camera at different depth z: red dashed window shows at z_{min} and solid blue window shows at z_{max}; (b) Corresponding Φ_{min} and Φ_{max} defined on the projector; (c) Cross sections of Φ_{min} and Φ_{max} and the wrapped phase maps with 2π discontinuities.

The above example demonstrates that the equivalent phase ϕ^{eq} does not have to be continuous across the whole area: it is fine to have one 2π jump. This indicates that the scaling factor T^{eq}/T^1 can be half of the required value, leading to reducing the noise impact by a factor of 2.

The question is: can we increase the number of 2π jumps and still properly find them using the geometric constraints (or Φ_{min}) to remove them. Figure 3.2 illustrates the cases for 2, and 3 jumps. Figure 3.2(a) shows a case where there are two 2π jump locations, A and B. Between A and B, the phase difference $\Phi_{min} - \phi_1$ is larger than 0 but less than 2π; but on the right of Point B, the phase difference is larger than

2π. Therefore, 2π should be added to unwrap the point between A and B, and 4π should be added on the right side of Point B.

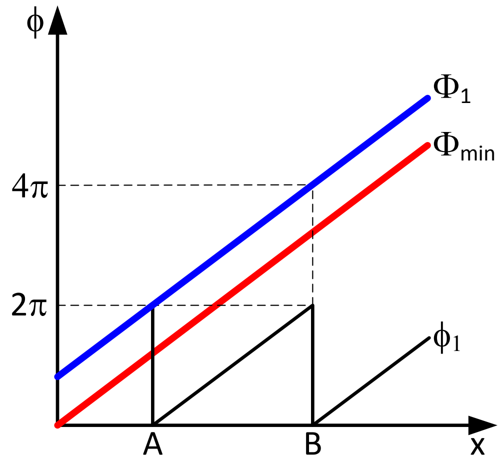

(a)

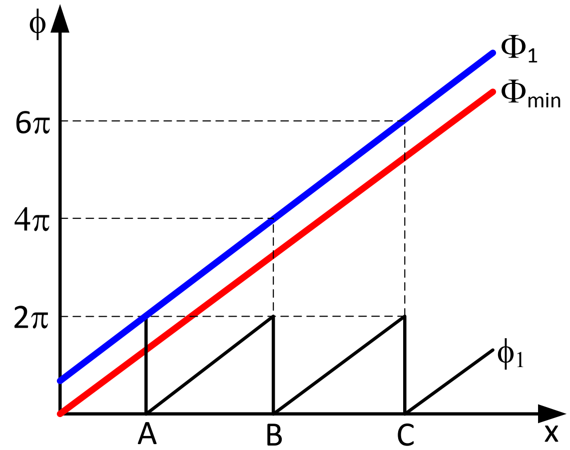

(b)

Fig. 3.2. Determination of number of 2π to be added by using Φ_{min} when low-frequency phase has multiple 2π jumps. (a) Example of having two 2π jumps; (b) Example of having three 2π jumps.

For cases with three jumps shown in Fig. 3.2(b), if $0 < \Phi_{min} - \phi_1 < 2\pi$, 2π (i.e. between A and B) should be added; $2\pi < \Phi_{min} - \phi_1 < 4\pi$ (i.e. between B and C), 4π should be added; and $4\pi < \Phi_{min} - \phi_1 < 6\pi$ (i.e., beyond C), 6π should be added. Similarly approach can be used to determine the number of 2π to be added for the equivalent phase.

As aforementioned, the use of 2π jumps for the equivalent phase for temporal phase unwrapping is to reduce the scaling factor. If N number of jumps are used, the scaling factor T^{eq}/T^1 can will be reduced by a factor of $N + 1$, and thus reduce the noise impact to 1/(N+1) times.

3.3 Simulations

Simulations were performed to demonstrate the viability of the proposed method to improve the two-frequency phase-shifting algorithm. Figure 3.3 shows an example

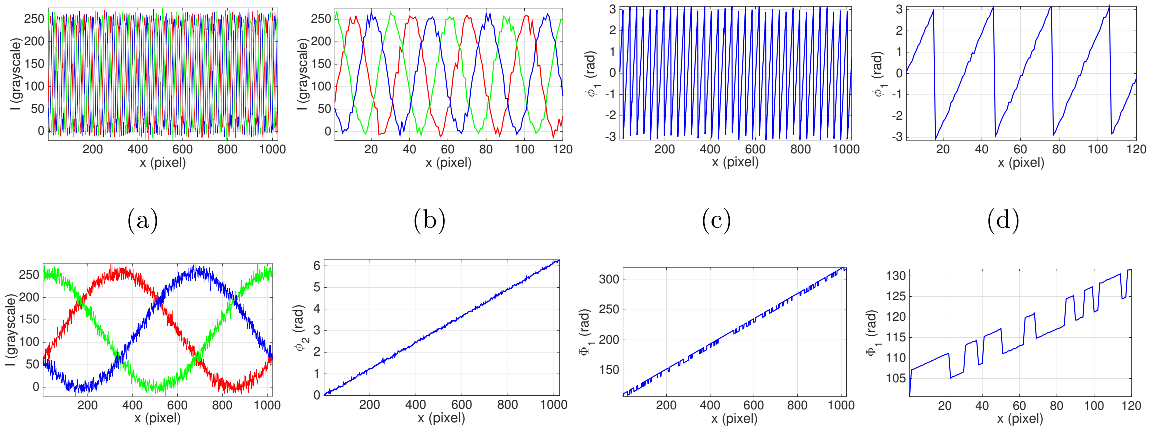

(a) (b) (c) (d)

(e) (f) (g) (h)

Fig. 3.3. Simulation result of standard two-frequency phase unwrapping when the signal to noise ratio (SNR) is not high (for this example SNR = 25). (a) Three high-frequency phase-shifted fringe patterns with phase shifts of $2\pi/3$ and fringe period of $T = 30$ pixels; (b) Zoom-in view of fringe patterns shown in (a); (c) Wrapped phase of the high-frequency fringe patterns; (d) Zoom-in view of the high-frequency phase; (e) Low frequency fringe patterns; (f) Low-frequency phase; (g) Unwrapped high-frequency phase; (h) Zoom-in-view of the unwrapped high-frequency phase.

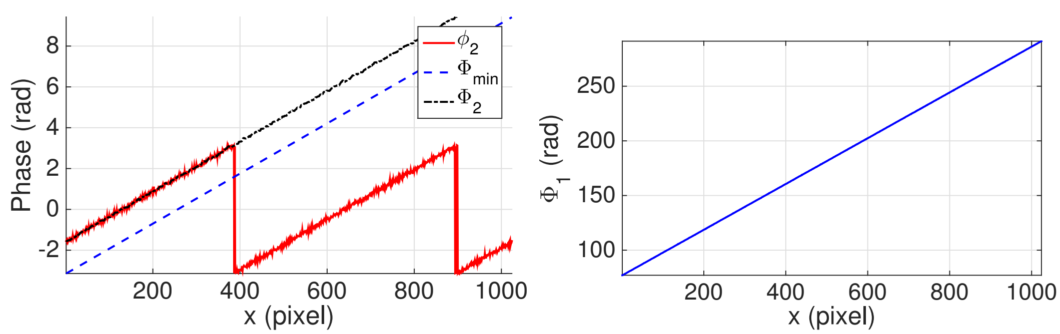

(a) (b)

Fig. 3.4. Example of using one jump on the low-frequency phase and geometric constraints to unwrap the high-frequency phase. (a) Original low frequency phase ϕ_2, the phase at z_{min} from geometric constraints Φ_{min}, and the unwrapped low-frequency phase Φ_2; (b) Unwrapped high-frequency phase Φ_1.

that fails standard two-frequency phase unwrapping when the high-frequency phase has a fringe period of $T^1 = 30$ pixels; and the low-frequency phase has a fringe period of $T^2 = 1024$ pixels. In this simulation, Gaussian noise was added such that the signal to noise ratio (SNR) is 25. Figure 3.3(a) shows three phase-shifted high-frequency fringe patterns; and Figure 3.3(b) shows a close-up view of the fringe patterns, as can be seen the fringe patterns are noisy. Figure 3.3(c) shows the phase can be computed using (3.4), and its zoom-in view is shown in Fig. 3.3(d). The low-frequency fringe patterns and the phase is respectively shown in Fig. 3.3(e) and 3.3(f). Directly applying the conventional two-frequency phase unwrapping will generate the phase map shown in Fig. 3.3(g). Clearly, the phase is not smooth with many points being incorrectly unwrapped. Figure 3.3(h) shows a closed-up view of the unwrapped phase, showing that the incorrectly unwrapped phase points cannot be filtered out by filters since they are many successive points.

We then added one jump to the low-frequency fringe patterns and use the geometric constraints to remove 2π jumps of the low-frequency phase, as shown in Fig. 3.4(a). By using the unwrapped phase with one jump, the high-frequency phase shown in Fig. 3.3(c) can be properly unwrapped, as shown in Fig. 3.4(b).

3.4 Experiment

To verify the performance of the proposed method, we developed a DFP system that includes a complementary metal oxide semiconductor(CMOS) camera (Model: Vision Research Phantom V9.1), a DLP projector (Model: Texas Instruments LightCrafter 4500) and a microprocessor (Model: Arduino Uno). The camera is attached with a 24 mm focal length lens (Model: SIGNA 24 mm f/1.8 EX DG). The camera resolution selected was 1024 × 1024, and the image data was transferred to a computer via an Ethernet cable. The resolution of the projector is 912 × 1140. The microprocessor was used to synchronize the camera with the projector. The system was calibrated using the method discussed in [61]. For all experiments presented in this chapter,

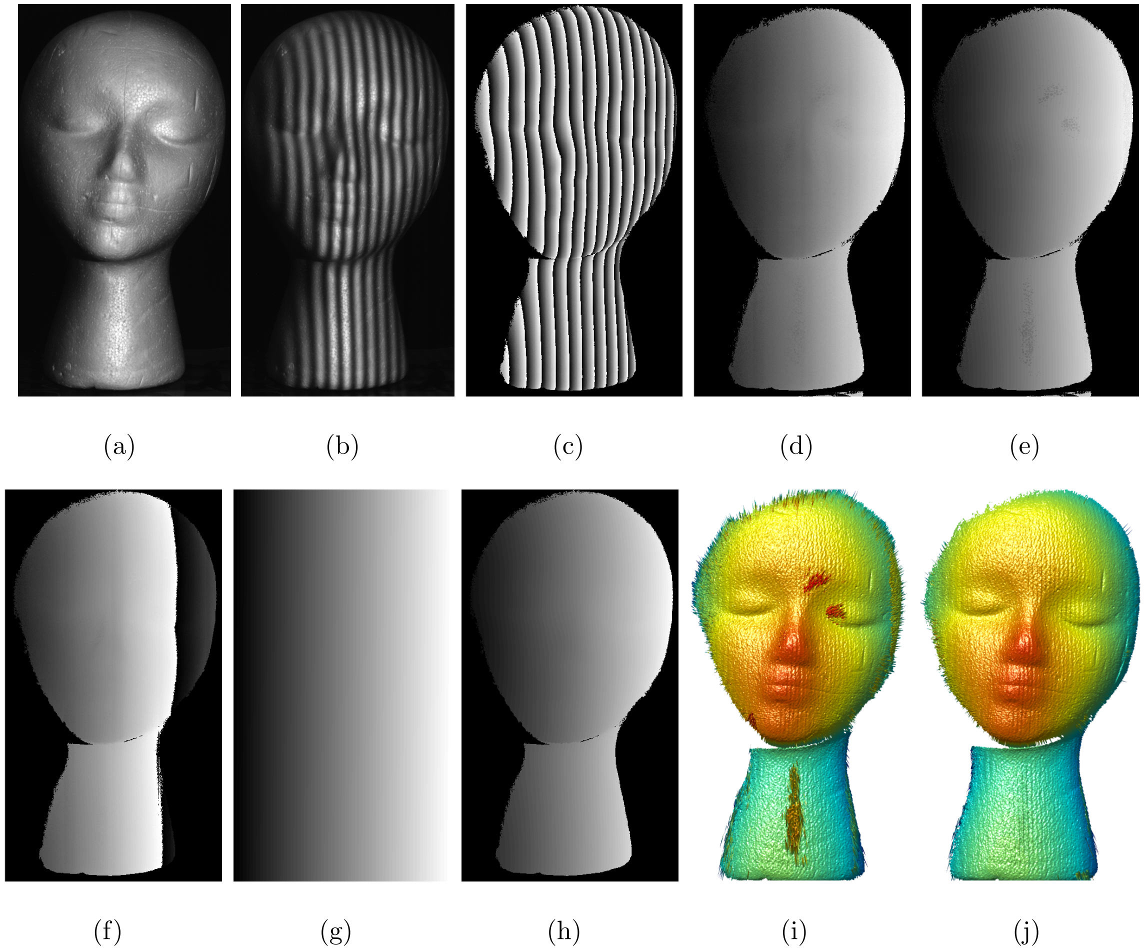

Fig. 3.5. Comparison of the conventional two-frequency phase-shifting algorithm and the proposed enhanced algorithm when the fringe patterns are of high quality. (a) Photograph of the measured statue; (b) One of the captured high-frequency fringe patterns; (c) Wrapped phase from high-frequency fringe patterns; (d) Wrapped phase from low-frequency fringe patterns with fringe period of 1140 pixels; (e) Unwrapped phase using the conventional two-frequency phase-shifting algorithm; (f) Wrapped phase from low-frequency fringe patterns with fringe period of 380 pixels; (g) Minimum wrapped phase Φ_{min}; (h) Unwrapped phase using the proposed method; (i) 3D result using the conventional two-frequency phase-shifting method; (j) 3D result using the proposed two-frequency phase-shifting method.

horizontal fringe patterns are generated by computer and projected by the projector. Since the projector's vertical resolution is 1140 pixels, the equivalent fringe period has to be $T^{eq} = 1140$ pixels in order to temporally unwrap high frequency phase if a conventional two-frequency phase-shifting algorithm is used.

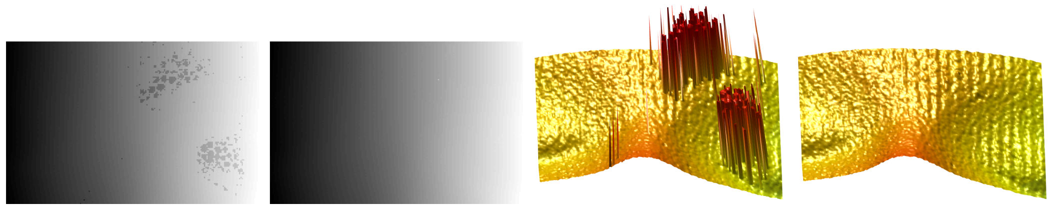

(a) (b) (c) (d)

Fig. 3.6. Close-up views of the results from Fig. 3.5 around the eye region. (a) Zoom-in view of the unwrapped phase map shown in Fig. 3.5(e); (b) Zoom-in view of the unwrapped phase map shown in Fig. 3.5(h); (c) Zoom-in view of 3D result shown in Fig. 3.5(i); (d) Zoom-in view of 3D result shown in Fig. 3.5(j).

We experimentally verified the performance of the enhanced two-frequency phase-shifting method. We first test the case when fringe patterns are of high quality (i.e., high SNR). Figure 3.5(a) shows the photograph of the statue we measured. It is important to note that we did not show the full resolution image of 1024×1024 because the rest areas are simply the background; and we crop the image the same way for all images to for the same of clearer visualizations. In this experiment, the high-frequency fringe patterns use fringe periods of $T^1 = 30$ pixels. One of the high-requency fringe patterns and the wrapped phase map is respectively shown in Fig. 3.5(b) and Fig 3.5(c). If a conventional two-frequency phase-shifting algorithm is applied, the low-frequency fringe patterns have a fringe period of $T^2 = 1140$ pixels, and the corresponding wrapped phase is shown in Fig. 3.5(d). Applying a conventional two-frequency phase-shifting algorithm results in the unwrapped phase shown in Fig. 3.5(e). As one might see, the unwrapped phase is not smooth on the neck and around the right eye regions, indicating some areas of the phase are not correctly unwrapped.

In contrast, if the proposed method is used, the low-frequency fringe pattern can have multiple fringes. For example, we can can use fringe period of $T^2 = 380$

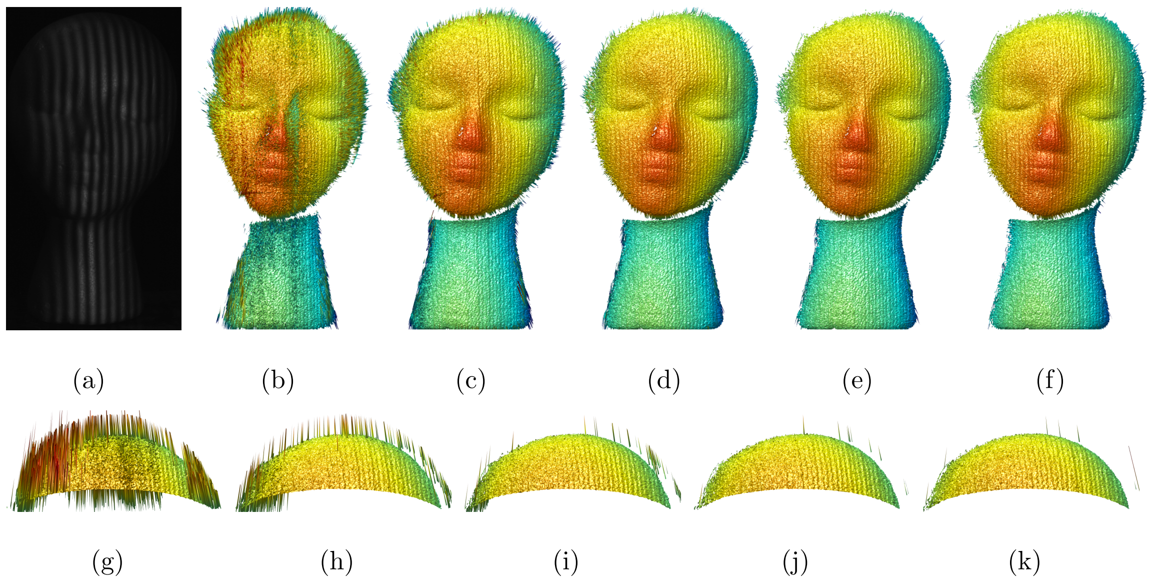

Fig. 3.7. Comparison of the conventional two-frequency phase-shifting algorithm and the proposed enhanced algorithm when the fringe patterns have low SNR. (a) One of the captured high-frequency fringe patterns; (b) 3D result using the conventional two-frequency phase-shifting method; (c)-(f) 3D results using the proposed two-frequency phase-shifting method when low frequency fringe patterns use two (c), three (d), four (e), and five (f) periods of sinusoidal fringes respectively; (g)-(k) Zoom-in views of the same regions for results shown in (b)-(f).

pixels to reduce the noise impact. Figure 3.5(f) shows the wrapped phase map. The minimum phase map determined from geometric constraints of the corresponding region is shown in Fig. 3.5(g). Figure 3.5(h) shows the unwrapped phase map using the proposed method. This phase map is smooth overall. Once the unwrapped phase map are obtained, 3D shape can be reconstructed. Figure 3.5(i) and 3.5(j) respectively shows 3D reconstruction using the conventional two-frequency phase-shifting algorithm and that using our proposed algorithm.

To better visualize differences, Figure 3.6 shows the closed-up view of the unwrapped phase maps and the corresponding 3D reconstructions. 3D result from our proposed method does not have spiky noisy points that are apparent on the result from the conventional algorithm. These experiments clearly demonstrated that even for high-quality fringe patterns, the conventional two-frequency phase-shifting algorithm could still fail to correctly unwrap the phase due to the large scaling factor T^{eq}/T^1. In comparison, the proposed method does not have such a problem.

To further verify the performance of the proposed method, we measured the same statue with low fringe quality to emulate low SNR cases. Figure 3.7(a) shows one of the capture high-frequency fringe patterns, clearly the pattern has low SNR. Figure 3.7(b) shows 3D results from the conventional two-frequency phase-shifting algorithm. The whole surface is poorly measured with spiky points present everywhere, as anticipated. In contrast, if we use the proposed method to perform measurement under exactly the same settings, the 3D results are shown in Fig. 3.7(c)-Fig. 3.7(f) with different number of jumps ranging from 1 to 4. To better visualize the differences, we showed zoom-in views of the overhead area for all these results, as shown in Fig. 3.7(g)-Fig. 3.7(g). They all greatly reduced incorrectly unwrapped points with more jumps providing better results. However, one may notice that, for such a low SNR case, using one jump (or two periods for low-frequency fringe patterns) is not sufficient, but using five periods of fringe patterns can almost eliminate all incorrectly unwrapped points. It should be noted that by using five periods of fringe patterns, the proposed method reduce the noise impact by a fact of five. These experiments further demonstrated that the proposed two-frequency phase-shifting algorithm can indeed greatly enhance the performance of the conventional two-frequency phase-shifting algorithm by using the minimum phase.

3.5 Summary

This chapter has presented a method to substantially improve the conventional two-frequency phase-shifting algorithm by using geometric constraints of the DFP system. We demonstrated that the noise impact can be substantially reduced by allowing the use of more than one period of equivalent phase map to determine fringe order. Both simulation and experiments successfully verified the drastic improvements of the proposed method over the conventional two-frequency phase-shifting algorithm. Since the proposed method does not require more fringe patterns to be captured, it has the advantage of measurement speeds for high-speed applications.

4. SUPERFAST 3D ABSOLUTE SHAPE MEASUREMENT USING FIVE BINARY PATTERNS

4.1 Introduction

High-speed 3D shape measurement using structured light methods has been increasingly employed to capture fast motion due to reduced hardware costs. Yet, it is always beneficial to capture faster motion with the same available hardware technologies.

Typically, a high-speed 3D shape measurement system uses multiple rapidly changing structured patterns to recover one 3D shape. Given a pattern generator, its maximum pattern switching rate is limited by its hardware layout. For example, a now popular DLP Lightcrafter 4500 can switch binary patterns at 4225 Hz, or 8-bit grayscale patterns at 120 Hz. Therefore, using less number of patterns to recover one 3D shape is always of interest for high-speed applications.

Fourier method uses only a single pattern for 3D shape measurement [30], yet it is limited to measuring rather smooth surfaces without complex texture, and only relative 3D geometry since the phase obtained from such a method is not absolute. To increase its robustness, Guo et al. [62] developed modified FTP method that used two fringe patterns. Though successful, it still can only measure relative shape. Li et al. [63] added one more pattern to determine fringe order for 3D absolute shape measurement. However, this method requires the voting process for fringe order determination, making it difficult to measure object with complex surface geometry. Furthermore, comparing with phase-shifting method, the phase accuracy obtained from the Fourier method is much lower. Therefore, for high accuracy measurements, phase-shifting methods are preferable.

By encoding one single marker on carried fringe patterns, Zhang et al. [64] recovered absolute phase only using three phase-shifted fringe patterns. Similarly, Cui et al. [65] developed absolute recovery method by encoding a single line on three phase-shifted fringe patterns. These marker encoding methods work if the surface geometry is smooth since a spatial phase unwrapping algorithm is required.

Methods also developed to recover absolute phase by adding a second camera. Li et al. [66] developed a method to obtain absolute phase with three phase-shifted fringe patterns by using geometric constraint for a dual-camera and a single projector system. Lohry and Zhang [46] developed two-stage method that uses stereo camera to obtain rough disparity map and uses phase to refine the disparity map. Despite some advantages, these techniques use two cameras and one projector. Such a dual-camera and a single projector technique creates more shadow related problems since all three devices must see the point in order to measure the point. Moreover, the high-speed cameras are usually very expensive. Therefore, using a single projector and a single camera for high-speed measurements is still desirable.

For absolute phase measurement, it typically requires more than three fringe patterns for a single-projector and a single-camera system. Liu et al. [42] developed a method that uses five phase-shifted fringe patterns by compositing two-frequency phase information into the same phase-shifted patterns, and the absolute phase is recovered after demodulating the phase. Zuo et al. [67] applied a similar strategy using binary defocusing method with tripolar pulse-width-modulation (TPWM) for kHz 3D shape measurement. However, since these methods encode two frequency phases into the same fringe pattern, the phase-quality is compromised compared to the single frequency phase encoding methods.

It is well known that absolute phase can be obtained by using two sets of phase-shifted fringe patterns with two different frequencies with the equivalent wavelength to cover the whole range of sensing [68]; and for DFP systems, one can also use a wide fringe pattern with a single period of sinusoidal pattern covering the whole range [69].

Yet, due to noise, it is typically difficult for two-wavelength methods to choose very narrow fringe patterns for higher frequency phase [59].

For DFP systems, one can also combine binary patterns with phase-shifted fringe patterns for absolute phase recovery [70]. In essence, this hybrid method uses the binary patterns to determine fringe order for each pixel and unwrap the absolute phase. However, three binary patterns can only generate 8 unique numbers, and thus this method cannot use more than 8 fringe stripes if only six patterns are used. Wang and Zhang [56] proposed a method that encodes fringe order information into the phase of three phase-shifted fringe patterns for absolute phase unwrapping. Such a method has proven successful to use narrow fringe patterns with only six pattern. Yet, these methods use one more pattern for absolute phase retrieval than those methods only using five patterns [42, 67]. To retrieve more accurate absolute phase with higher frequency, Zheng et al. [57] proposed to use six additional patterns to encode fringe order; though successful, it actually increases the number of patterns used (9 total patterns). Apparently, similar concepts can be implemented into three color channels [71], but it is well known that using color is not desirable to measure colorful object. Lately, Xing et al. [72] attempted to use the Newton-Raphson method to address the nonlinear gamma issues of the phase-coding method if the projector's nonlinear gamma is not pre-calibrated.

The above mentioned phase-coding methods all use 8-bit patterns for phase recovery, which is good for slow speed applications. Yet, to capture higher speed motions, faster 3D shape measurement is required. If binary patterns are used, much higher frame rates (kHz) can be achieved especially a DLP projector is used. This chapter presents a method that only uses five binary fringe patterns for pixel-by-pixel and dense absolute phase recovery. Specifically, three dense binary dithered patterns are used to compute the wrapped phase; and the average intensity and two additional binary patterns are used to determine fringe order pixel by pixel in phase domain using the phase-coding method developed by Wang and Zhang [56]. The wrapped phase is temporarily unwrapped point by point by referring to the fringe order. To use narrow fringe patterns and reduce noise impact, we further developed a computational framework by using geometric constraint of the DFP system. Since only binary patterns are required, we demonstrated that superfast 3D shape measurement can be achieved: we developed a system that can capture binary patterns at 3,333 Hz; and since 5 patterns can recover one 3D shape, we achieved a 667 Hz 3D shape measurement rate.

Section 4.2 discusses the principles behind the proposed method. Section 4.3 presents experimental validation; and Sec. 4.4 summarizes this chapter.

4.2 Principle

In this section, we introduce related theoretical background of this research. Phase-shifting algorithm is briefly introduced, and the proposed five pattern absolute phase unwrapping method is detailed, and the proposed computational framework is elucidated.

4.2.1 Three-step phase-shifting algorithm

Over recent decades, a number of strategies for phase-shifting algorithm that are widely known in the field of 3D optical metrology have been rapidly improved. Phase-shifting methods have considerable advantages: robust to noise and surface reflectivity variations, and accurate in pixel-by-pixel 3D coordinate reconstruction. Among all phase-shifting algorithms, the three-step phase-shifting algorithm requires minimum number of fringe patterns for phase calculation. Three patterns can be mathematically described as,

$$I_1(x,y) = I'(x,y) + I''(x,y)\cos[\phi(x,y) - 2\pi/3], \tag{4.1}$$

$$I_2(x,y) = I'(x,y) + I''(x,y)\cos[\phi(x,y)], \tag{4.2}$$

$$I_3(x,y) = I'(x,y) + I''(x,y)\cos[\phi(x,y) + 2\pi/3], \tag{4.3}$$

where $I'(x,y)$ is the average intensity, $I''(x,y)$ the intensity modulation, and $\phi(x,y)$ the phase to be solved for. By means of using an inverse tangent function, the phase can be easily described as,

$$\phi(x,y) = \tan^{-1}\left[\frac{\sqrt{3}(I_1 - I_3)}{2I_2 - I_1 - I_3}\right]. \tag{4.4}$$

Because of the limitation of the arctangent function, the phase obtained from Eq. (4.4) ranges from $-\pi$ to $+\pi$. To retrieve absolute phase, a temporal phase-unwrapping framework is usually needed. In the next section, we will introduce our proposed temporal phase unwrapping method. Phase unwrapping essentially determines fringe order $K(x,y)$ such that 2π discontinuities of the wrapped phase can be properly unwrapped

$$\Phi(x,y) = 2\pi \times K(x,y) + \phi(x,y), \tag{4.5}$$

Here $\Phi(x,y)$ denotes the unwrapped phase map.

Equations (4.1)-(4.3) also give the average intensity information as

$$I'(x,y) = [I_1(x,y) + I_2(x,y) + I_3(x,y)]/3, \tag{4.6}$$

which can be used to determine the texture of the object.

4.2.2 Proposed phase-coding algorithm

We propose a new method that only requires two additional patterns to determine fringe order for each pixel, these two additional fringe patterns directly encode fringe order information as,

$$\Phi_s(x,y) = -\pi + Floor[x/W] \times \frac{2\pi}{N}, \tag{4.7}$$

$$I_4(x,y) = I'(x,y) + I''(x,y)\cos[\Phi_s(x,y)], \tag{4.8}$$

$$I_5(x,y) = I'(x,y) + I''(x,y)\sin[\Phi_s(x,y)], \tag{4.9}$$

where Φ_s is the stair phase map which determines the fringe order depending on where (x,y) is located, N is the number of stairs, $Floor[]$ is the floor operator to determine the truncated integer number, and W is the overall span of the fringe pattern along x direction. In this case, there are 3 unknowns (I', I'', and Φ_s) and 2 equations (Eq. (4.8) and Eq. (4.9)). To uniquely solve for Φ_s and thus fringe order, we combine Eq. (4.6) with these two equations. $\Phi_s(x, y)$ and fringe order $K(x, y)$ can be uniquely solved for each pixel as,

$$\Phi_s(x, y) = \tan^{-1}\left[\frac{I_5 - I'}{I_4 - I'}\right], \tag{4.10}$$

$$K(x, y) = Round\left[N \times \left(\frac{\Phi_s + \pi}{2\pi}\right)\right]. \tag{4.11}$$

It should be noted that $\Phi_s(x, y)$ is the unwrapped phase since one single fringe pattern covers the whole fringe span.

Figure 4.1 shows an example of using the proposed temporal phase unwrapping method. Figure 4.1(a) shows the wrapped phase from three phase-shifted fringe patterns. Figure 4.1(b) shows the real number of fringe order before quantization and the integer number of the fringe order. In this example, Gaussian noise with a signal to noise ratio (SNR) of 25 was added to fringe patterns to emulate the practical system noise. Figure 4.1(c) shows the result after directly applying the fringe order to temporally unwrap the wrapped phase pixel-by-pixel. One can clearly see spiky noise on the unwrapped phase map. Such spiky noise can be reduced by applying a computational framework such as a median filter. Figure 4.1(d) shows the result after the computational framework discussed by Karpinsky et al. [73].

Our experimental data shows that if the noise is larger and/or the phase shifted fringe patterns are narrower (i.e., more stairs are used), the aforementioned computational framework fails to effectively reduce the spiky noise. Unfortunately, for our high-speed measurement application, the noise is quite large and we have to use narrow fringe pattern to achieve high-quality measurement. To address this problem, we have developed an computational framework to significantly reduce noise impact, which will be discussed next.

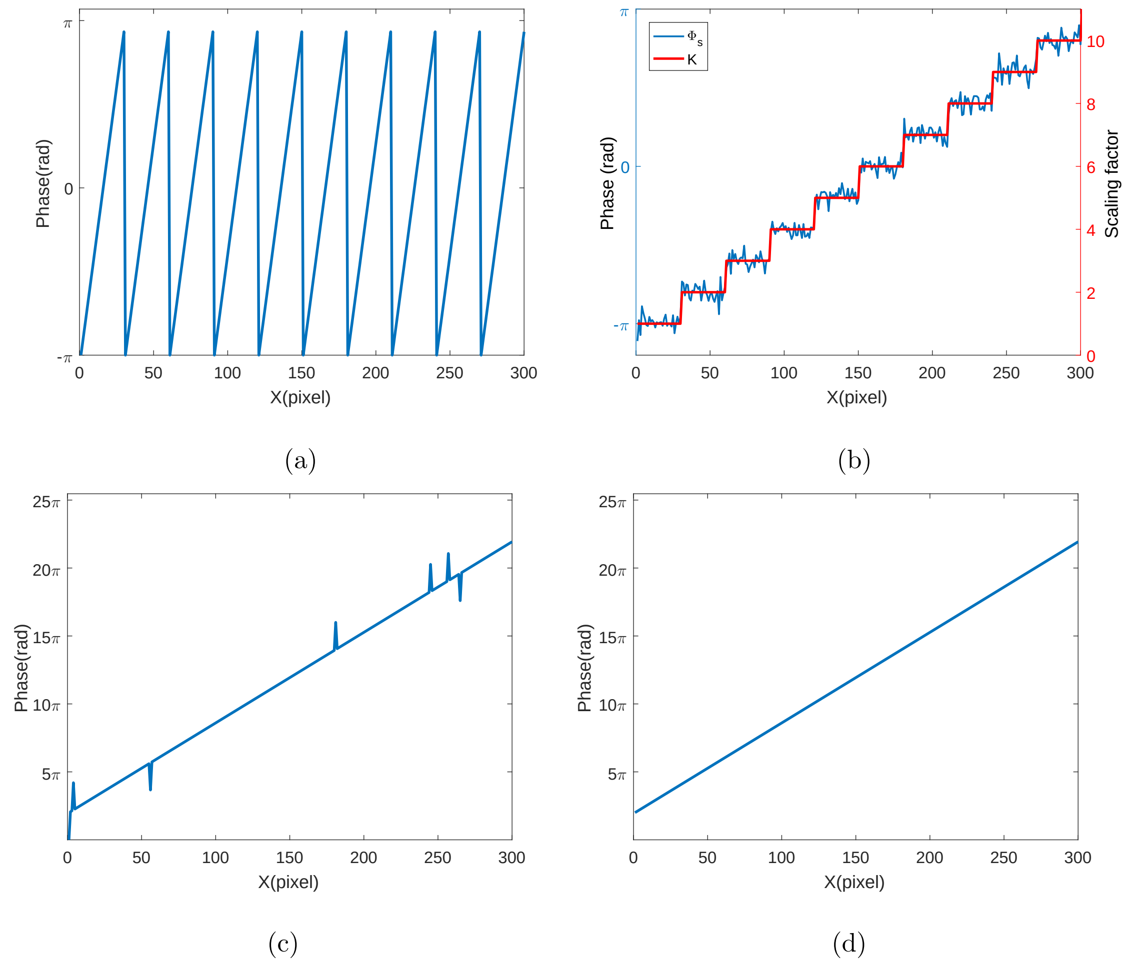

Fig. 4.1. Cross section of ideal image. (a) Wrapped phase map with fringe period of 30 pixels; (b) comparison of the stair phase with the fringe order after rounding off the phase to the nearest integer;(c) absolute phase directly obtained from Eq. (4.11); (d) absolute phase after removing spikes.

4.2.3 Computational framework for reducing noise influence

As aforementioned, to achieve high accuracy, the fringe period needs to be small, and thus the encoded stair height is small, making it more sensitive to noise; and the use of dithered pattern and out-of-focus projector further deteriorates fringe quality. To address such problems, we propose to use the geometric constraints of the DFP system to allow the use of more than one period of patterns (i.e., more than 2π phase range) to encode fringe order. This section details the principle of this computational approach.

To understand the proposed method, DFP system geometric model needs to be discussed. In this research, we utilize the well-known pinhole model to illustrate the imaging lenses of a DFP system. The model mathematically describes the relationship between 3D (x^w, y^w, z^w) world coordinates and 2D (u, v) imaging coordinates as,

$$s\begin{bmatrix} u \\ v \\ 1 \end{bmatrix} = \begin{bmatrix} f_u & \gamma & u_0 \\ 0 & f_v & v_0 \\ 0 & 0 & 1 \end{bmatrix}\begin{bmatrix} r_{11} & r_{12} & r_{13} & t_1 \\ r_{21} & r_{22} & r_{23} & t_2 \\ r_{31} & r_{32} & r_{33} & t_3 \end{bmatrix}\begin{bmatrix} x^w \\ y^w \\ z^w \\ 1 \end{bmatrix}, \tag{4.12}$$

where s is a scaling factor; f_u and f_v are, respectively, the effective focal length in u and v directions; γ is the skew factor of u and v axes, and for research-grade cameras $\gamma = 0$; r_{ij} and t_i, respectively, denote the rotation and translation variables; and (u_0, v_0) is the principle point. We can simplify the matrices as,

$$\mathbf{P} = \begin{bmatrix} f_u & \gamma & u_0 \\ 0 & f_v & v_0 \\ 0 & 0 & 1 \end{bmatrix}\begin{bmatrix} r_{11} & r_{12} & r_{13} & t_1 \\ r_{21} & r_{22} & r_{23} & t_2 \\ r_{31} & r_{32} & r_{33} & t_3 \end{bmatrix} = \begin{bmatrix} p_{11} & p_{12} & p_{13} & p_{14} \\ p_{21} & p_{22} & p_{23} & p_{24} \\ p_{31} & p_{32} & p_{33} & p_{34} \end{bmatrix}, \tag{4.13}$$

where the projection matrix P can be estimated through calibration. The projector and the camera have exactly the same mathematical model, albeit the projector is an output device, as the inverse of a camera. If both projector and camera are calibrated under the same world coordinate system, we have

$$s^p[\ u^p \quad v^p \quad 1\ ]^t = P^p[\ x^w \quad y^w \quad z^w \quad 1\ ]^t, \tag{4.14}$$

$$s^c[\ u^c \quad v^c \quad 1\ ]^t = P^c[\ x^w \quad y^w \quad z^w \quad 1\ ]^t. \tag{4.15}$$

Here superscript p denotes the projector, superscript c the camera, and superscript t the transpose of a matrix. Eq. (4.14) and Eq. (4.15) have six equations and seven unknowns $(s^c, s^p, x^w, y^w, z^w, u^p, v^p)$ for a given camera pixel (u^c, v^c). Therefore, we need one more equation to solve for up to get the corresponding absolute phase, which can be obtained by the linear relationship between absolute phase Φ and u^p,

$$u^p = \Phi \times T/(2\pi), \tag{4.16}$$

where T is a projection pattern's fringe period in pixel. For any given point, if z is known, the corresponding points for each camera pixel, (u^c, v^c), can computed and thus the phase value can be determined,

$$\Phi(u^c, v^c) = f(z, T, P^c, P^p). \tag{4.17}$$

Assume that $z = z_{min}$ which is the minimum depth z for the volume of interest, the virtual absolute phase map, Φ_{min}, corresponding to z_{min} can be generated by using Eq. (4.17). We call Φ_{min} as the minimum phase. Under the circumstance, Equation (4.10) only yields wrapped phase map $\phi_s = \Phi_s \mod (2\pi)$ since more than one period of fringe patterns are used. Since ϕ_s is calculated by simply using Eq. (4.10), the measurement volume is restricted as discussed by An et al. [45]. The wrapped phase can be unwrapped pixel-by-pixel by comparing Φ_{min} to obtain absolute phase Φ_s.

Figure 4.2 illustrates the fundamental concept of using the minimum phase to unwrapped periodical stair phase. Figure 4.2(a) shows the wrapped stair phase map with two periods of fringe patterns. The red dashed windows is the wrapped stair phase map of ϕ_1 when $z = z_{min}$ and the blue window is the phase map of ϕ_s when $z > z_{min}$. Figure 4.2(b) shows the phase map of Φ_{min}. This figure shows that the absolute phase Φ_s can be obtained by adding 2π when $\Phi_{min} > \phi_s$, as illustrated in Figure 4.2(c).

Figure 4.3 shows a case for three periodical fringe patterns. If ϕ_s is located between the point A and B, the difference between Φ_{min} and ϕ_s is greater than zero and less than 2π. Then, 2π should be added on the region. If ϕ_s is located on the right of the point B, 4π should be added to get a correct fringe order map. In other words, if the stair phase satisfies the following condition for an integer number P,

$$2\pi \times (P - 1) < \Phi_{min} - \phi_s < 2\pi \times P, \tag{4.18}$$

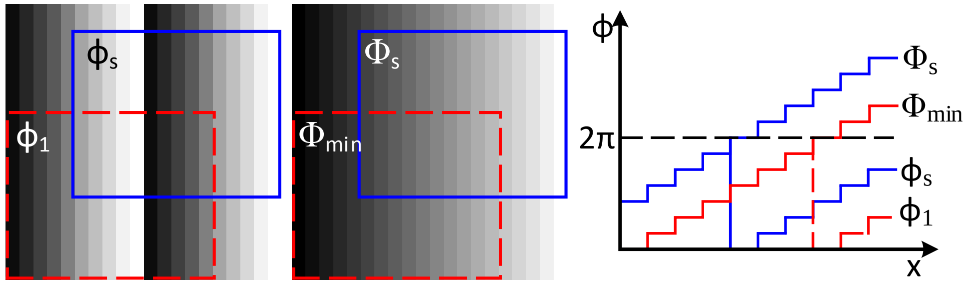

(a) (b) (c)

Fig. 4.2. Conceptual idea of removing 2π discontinuity of stair phase map by using the minimum phase. (a) Wrapped stair phase map by using Eq. (4.10); (b) unwrapped stair phase map after adding 2π where discontinuity occurs; (c) cross section of Φ_{min} and Φ_s and the wrapped phase maps.

or

$$P(x,y) = Ceil\left[\frac{\Phi_{min}(x,y) - \phi_s(x,y)}{2\pi}\right], \tag{4.19}$$

the absolute stair phase Φ_s can be determined as

$$\Phi_s(x,y) = 2\pi \times P(x,y) + \phi_s(x,y), \tag{4.20}$$

and fringe order K as

$$K(x,y) = Round\left[M \times \left(\frac{\Phi_s(x,y) + \pi}{2\pi}\right)\right], \tag{4.21}$$

where $Ceil[]$ is the ceiling operator that gives the closest upper integer number, and M is the number of stairs in one period of the stair phase. We can simplify Eq. (4.21) as

$$R(x,y) = M \times \left[\frac{\Phi_s(x,y) + \pi}{2\pi}\right], \tag{4.22}$$

and

$$K(x,y) = Round[R(x,y)], \tag{4.23}$$

where $R(x,y)$ is the real number to determine the integer number of fringe order K.

In summary, the proposed computational framework can more robustly unwrap the phase by allowing the use of more than one period of fringe patterns to encode

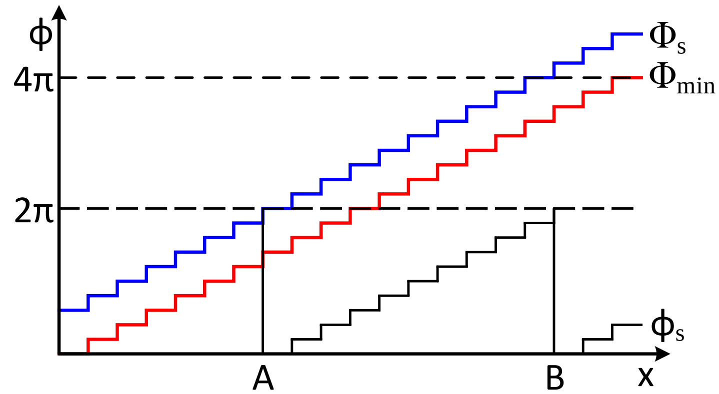

Fig. 4.3. Determination of the number of 2π jumps of the stair phase over two periods.

stair phase map. The key idea is to artificially create a minimum phase map using geometric constraints of the DFP system. The minimum phase map then unwraps the periodical phase stair phase map. Once the periodical stair phase is unwrapped, fringe order K can be determined that can be further used to temporally unwrap the wrapped phase. Because the proposed method allows the use of more than one period of fringe patterns for stair phase encoding, it is more robust to noise, enabling the use of narrower fringe patterns for higher accuracy measurement.

4.3 Experiment

A hardware system was developed to verify the performance of the proposed method. Figure 4.4 shows the photograph of our system. The system consists of a CMOS camera (Model: Vision Research Phantom V9.1), a DLP projector (Model: Texas Instruments LightCrafter 4500) and a microprocessor (Model: Arduino Uno). The camera is attached with a lens (Model: SIGMA 24 mm f/1.8 EX DG) whose focal length is 24 mm and aperture ranges from f/1.8 to f/22. The projector has the resolution of 912 $\times$ 1140 pixels. The microprocessor is utilized to synchronize the camera with the projector. The system is calibrated using the method developed by Li et al. [74].

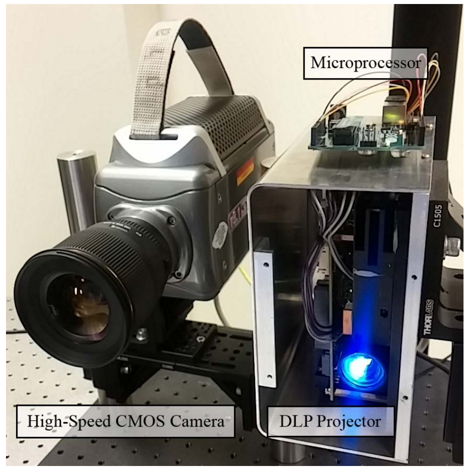

Fig. 4.4. Experimental setup for DFP calibration

We first measured a statue with the proposed method. Figure 4.5 shows the results. In this experiment, the camera resolution was set as 1024 $\times$ 1024 pixels, and the projector sequentially projects five binary dithered patterns at 1kHz, and the camera precisely synchronized with the projector captures each projected patterns. The phase-shifted fringe patterns have a fringe period of 30 pixels, and the stair phase encoded patterns have a fringe period of 1140 pixels. Figure 4.5(a) shows the image of the sculpture. We cropped all images in a same way for better visualization. Figure 4.5(b)-4.5(f) show five captured fringe patterns. From three phase-shifted fringe patterns shown in Figs. 4.5(b)-4.5(d), we computed the wrapped phase map, as shown in Fig. 4.5(g). Combining the averaged image, $I'(x, y)$, with two additional fringe patterns shown in Figs. 4.5(e)-4.5(f), we obtained the stair phase map $\Phi_s(x, y)$ as shown in Fig. 4.5(h). The fringe order of the wrapped phase can be calculated by using Eq. (4.11). Figure 4.5(i) shows the fringe order map. Once fringe order is determined, the phase can be unwrapped pixel by pixel. Figure 4.5(j) shows the unwrapped phase map. Due to the dithering effect and random noise of the system, the spiky noise is very severe. To visualize such a problem, we recovered 3D geometry of the object from the unwrapped phase. Figure 4.5(k) shows the result. It is obvious that it is very difficult to remove all spiky noise by filtering.

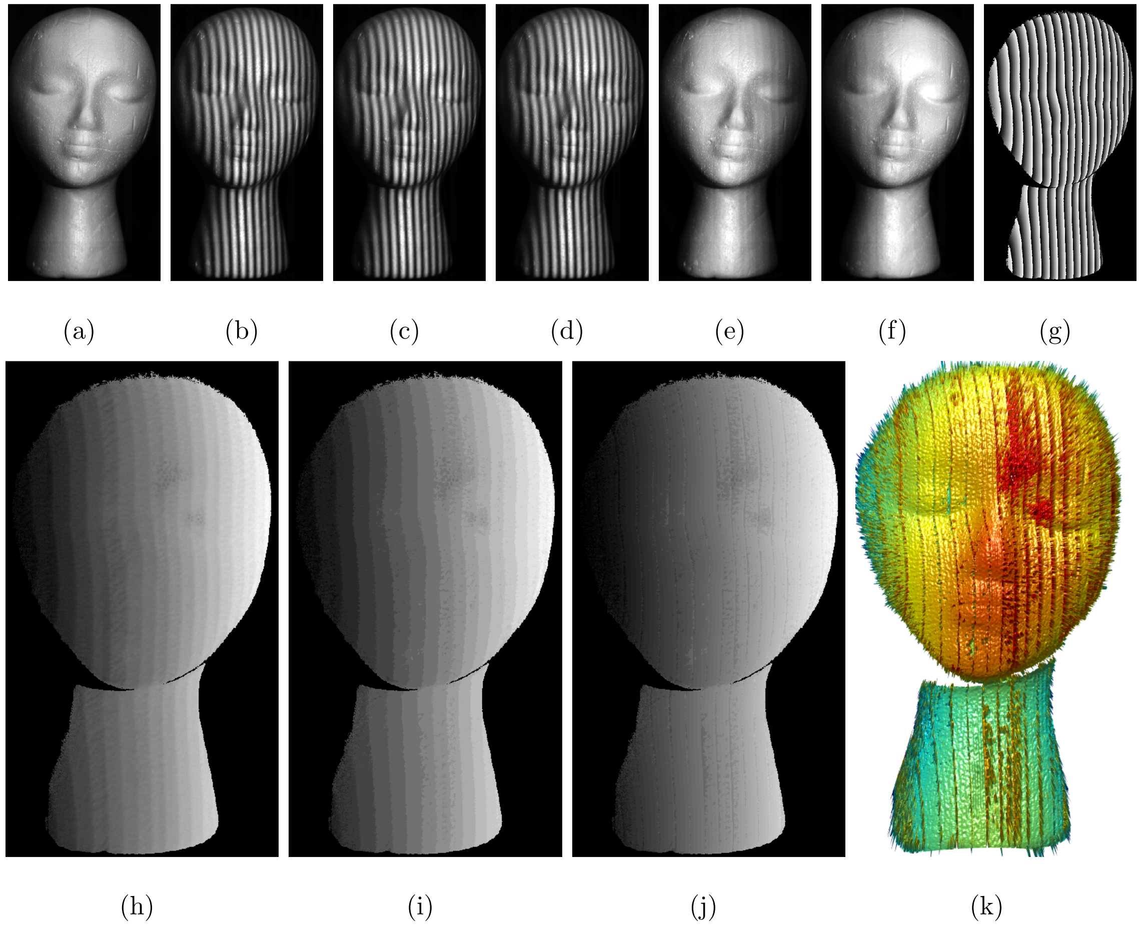

Fig. 4.5. Experimental captured data of the proposed method with a fringe period of 1140 pixels for the stair phase. (a) Photograph of the measured statue; (b)-(d) three phase-shifted high-frequency fringe images; (e)-(f) two phase-shifted low-frequency fringe images; (g) wrapped phase from high-frequency fringe patterns; (h) absolute stair phase map Φ_s; (i) fringe order map K; (j) unwrapped phase Φ; (k) 3D reconstruction result.

In comparison, we employed our proposed method to encode the stair phase. Instead of using one single fringe period, we used 2 periodical fringe patterns. Figures 4.6(a)-4.6(b) show those two fringe patterns. The phase map obtained by directly applying Eq. (4.10) is shown in Fig. 4.6(c), which still has 2π discontinuities, as expected. We then generated the minimum phase map Φ_{min}, as shown in Fig. 4.6(d), that was further used the unwrap the stair phase map. Figure 4.6(e) shows the un-

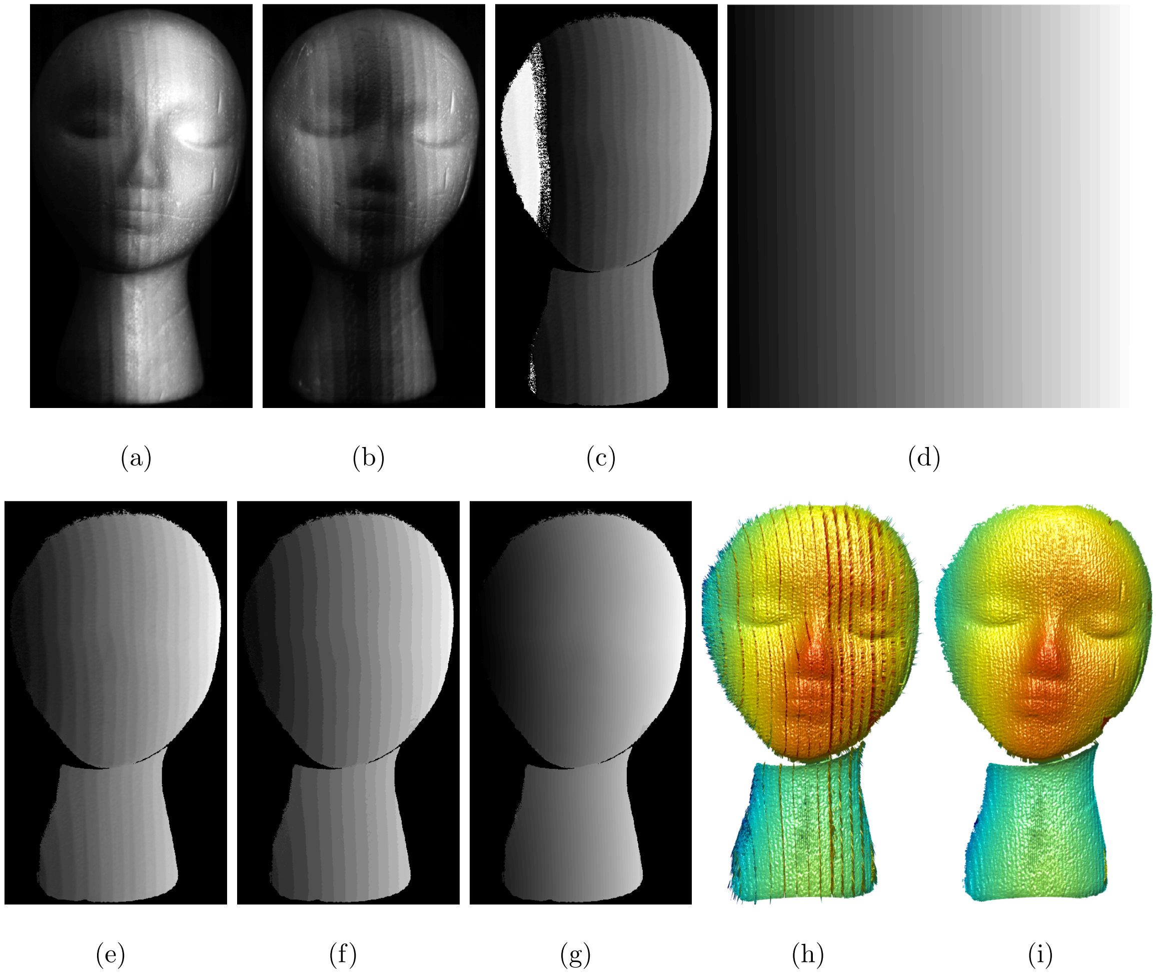

Fig. 4.6. Experimental captured data of the proposed method using geometric constraints. (a)-(b) two stair-shaped patterns (I_4 and I_5) for ϕ_s with a fringe period of 570 pixels; (c) wrapped stair phase ϕ_s with a 2π discontinuity; (d) the artificial minimum phase map when $z = z_{min}$; (e) unwrapped stair phase Φ_s using the geometric constraints; (f) fringe order map K; (g) unwrapped phase Φ; (h) 3D reconstruction result using the proposed method without applying any filter; (i) filtered 3D reconstruction result.

wrapped stair phase map using the proposed method. This stair phase map is then used to generate fringe order map, shown in Fig. 4.6(f), and temporally unwrap the phase map shown in Fig. 4.6(g). Figure 4.6(h) shows the reconstructed 3D shape. Compared with the result shown in Fig. 4.5(k), the spiky noise is substantially reduced, which can then be further removed by applying the computational framework developed by Karpinsky et al. [73]. Figure 4.6(i) shows the final result, which is fairly smooth, proving that the proposed method can successfully recover 3D shape of an object.

To show the difference between the proposed method and the conventional method clearly, we compared one cross section of the data. R was computed using Eq. (4.22), from which fringe order can bed determined using Eq. (4.23). Figure 4.7(a) and Figure 4.7(c) respectively show Φ_s using the conventional method and the proposed method. The red line describes the region where the cross section is to be compared. Figure 4.7(b) shows the graph of R and corresponding integer number K in the conventional method. In the middle of the graph, the noise become severe and the fringe order fluctuates depending on the noise effect. In comparison, R in Figure 4.7(d) which is obtained from the proposed computational framework is stable enough to determine the fringe order correctly. Despite some fluctuating noise, fringe order can still be correct correctly obtained. These two graphs verify that the proposed method is more robust to determine fringe order.

To demonstrate the capability of high-speed 3D shape measurement and absolute phase recovery. We simultaneously measured tow moving hands. This experiment, we set the camera resolution as 672×768. The projector projects and the camera captures at 3,333 Hz with an exposure time of 300 μs. Since five images are used to recover one 3D geometry, 3D measurement speed is actually 667 Hz. Figure 4.8 shows the measurement results. Figure 4.8(a) shows one of the frames we captured, and Figure 4.8(b) shows one of the fringe patterns for that frame. Figure 4.8(c) and associated video shows the sequence results for this experiment. This experiment successfully demonstrated that our proposed method can measure multiple isolated objects at high speed.

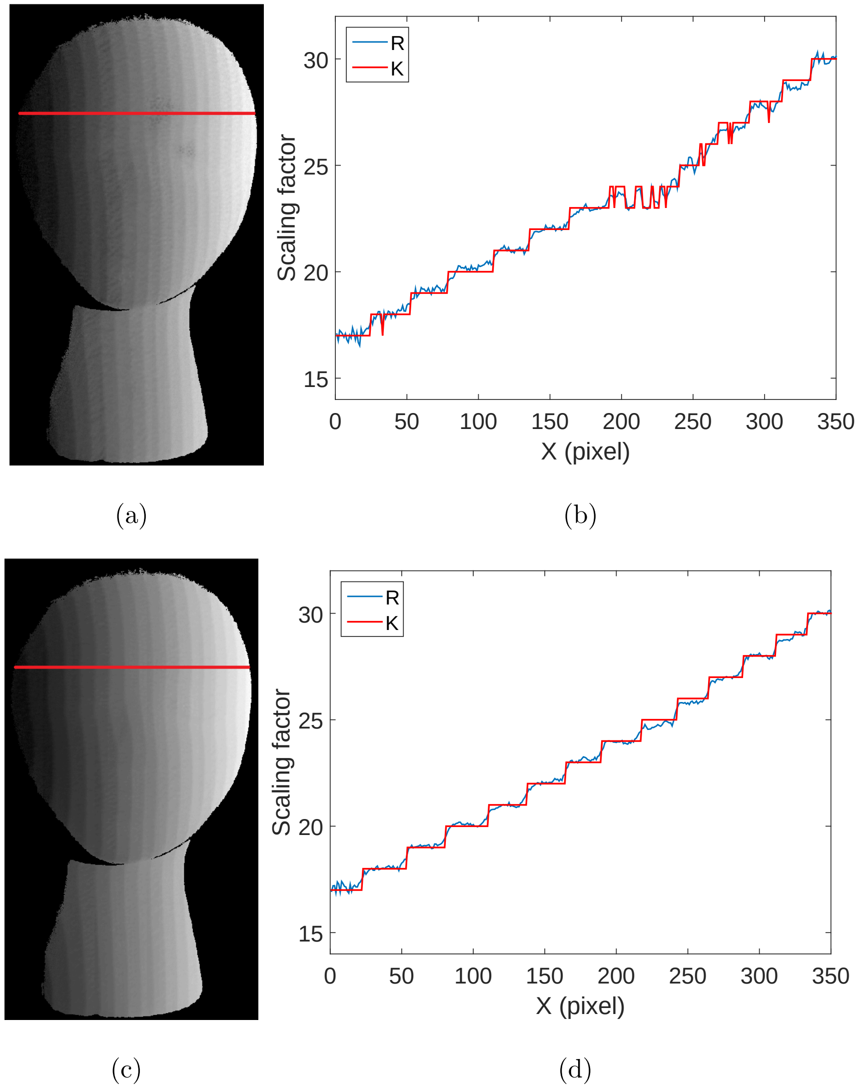

Fig. 4.7. Images of the stair phase and graphs of a cross section to compare the real number with its quantized number. (a) Absolute stair phase map by using the conventional method; (b) cross section of the red line on (a) to describe R and corresponding K of the conventional method; (c) absolute stair phase map by using the proposed method; (d) cross section of the red line on (c) to describe R and corresponding K of the proposed method.

4.4 Summary

This chapter has presented a superfast 3D absolute shape measurement method using five binary patterns. The proposed method uses binary dithering technique for

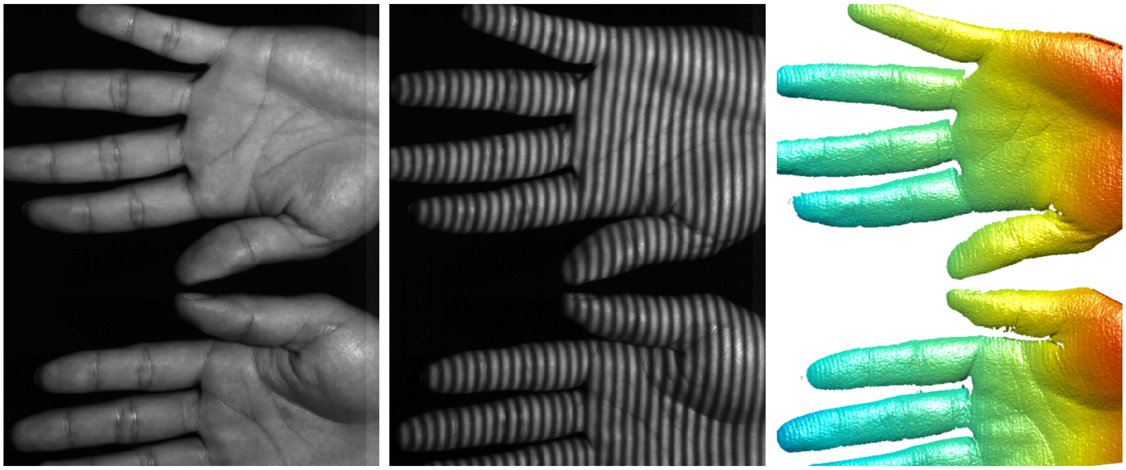

(a) (b) (c)

Fig. 4.8. Measurement result of capturing hands in high-speed. (a) Photograph of two hands; (b) one of three phase-shifted fringe patterns; (c) 3D reconstruction result.

high speed image projection, and reduces the number of frames by using the average intensity. We demonstrated that the noise of patterns due to dithering and random noise can be substantially reduced with the computational framework we developed. Our experimental results demonstrated that high-quality 3D shape measurement can be realized at a speed of 667 Hz.

5. HIGH-SPEED THREE-DIMENSIONAL ABSOLUTE SHAPE MEASUREMENT WITH THREE BINARY PATTERNS

5.1 Introduction

High-speed 3D shape measurement is of great interest to many applications. Numerous high-speed 3D shape measurement techniques have been developed. One of the approaches to achieve high-speed measurement is Fourier transform profilometry (FTP) [30]. FTP can reconstruct 3D geometry with a single pattern and thus achieve the highest possible measurement speed. However, FTP method does not work well when the object has complex surface geometry or texture because it is difficult to separate the carrier phase signal and the background (DC). Qian [75] developed the windowed Fourier transform (WFT) method that greatly improved the robustness of the FTP, yet the DC signal impact still remains, albeit at a less degree. To reduce the influence of DC signal, Guo et al. [62] developed a modified FTP method that uses two fringe patterns to completely eliminate the DC component. However, overall, the aforementioned methods can only recover relative phase and thus for relative 3D shape measurement.

To achieve absolute 3D shape measurement, Li et al. [76] proposed a method that added one more pattern to the modified FTP method. The third pattern contains slits that encode fringe order information for absolute phase unwrapping. However, such a method may not work well if surface geometry is complex because the voting process requires the use of many pixels within a window. Furthermore, all FTP methods requires the filtering process and the filter selection affects measurement quality. To overcome these limitations, this chapter propose a method that uses the same number of patterns (i.e., three) for pixel-by-pixel absolute phase unwrapping without the filtering process. The proposed method adopts Hilbert transform method for phase retrieval and geometric constraint based method for robust absolute phase unwrapping.

Phase information can also be recovered by applying the Hilbert transform. For example, Zweig and Hufnagel [77] employed the Hilbert transform profilometry (HTP) to directly retrieve phase from the original fringe image and Hilbert transformed image, assuming that the DC signal remains constant per line. Sutton et al. [78] increased the HTP capability by allowing varying DC signal through the development of a Laplacian pyramid algorithm to filter out the DC signal. Gdeisat el al. [79] further proved that if the object has abrupt depth change or shadow regions, HTP is superior to FTP. Similar to FTP, the DC signal also has significant impact to the recovered phase quality. To our knowledge, the state-of-the-art methods cannot recover absolute phase pixel by pixel using Hilbert transform and three patterns.

This chapter thus presents a method that can perform high-accuracy 3D shape measurement using only three patterns with one camera and one projector. To recover absolute phase, the proposed method employs the following procedures are: (1) take the difference between the sinusoidal fringe patterns and the DC pattern; (2) apply Hilbert transform to the difference images to generate two phase maps; (3) employ the geometric constraint based phase unwrapping method to unwrap the low-frequency phase map [80]; (4) unwrap the high-frequency phase map using the unwrapped low-frequency phase map; and (5) reconstruct 3D shape using the absolute phase. Since only three patterns are required, high-speed 3D shape measurement can be achieved. We developed a prototype system that can capture 2D images at 6,000 Hz, achieving 2,000 Hz 3D shape measurement speed.

Section 5.2 discusses the principle behind the proposed method. Section 5.3 presents experimental validation; and Sec. 5.4 summarizes the paper.

5.2 Principle

In this section, we will introduce technologies used in the proposed method including the Hilbert transform, enhanced two-frequency phase unwrapping method, as well as the computational framework of the proposed method to explain the procedures of 3D reconstruction.

5.2.1 Hilbert transform

Hilbert transform is a specific linear operator making a real function $\mu(t)$ to another real function $\mathcal{H}(\mu)(t)$ by using convolution,

$$\mathcal{H}(\mu)(t) = \frac{1}{\pi}\int_{-\infty}^{\infty}\frac{\mu(\tau)}{(t-\tau)}d\tau. \tag{5.1}$$

In frequency domain, one property of the Hilbert transform mathematically is

$$\mathcal{F}(\mathcal{H}(\mu)(\omega)) = \delta_{\mathcal{H}}(\omega) \times \mathcal{F}(\mu)(\omega), \tag{5.2}$$

where $\mathcal{F}(\cdot)$ means Fourier transform and

$$\delta_{\mathcal{H}}(\omega) = \begin{cases} i = e^{i\pi/2}, & \text{if } \omega < 0 \\ 0, & \text{if } \omega = 0. \\ -i = e^{-i\pi/2}, & \text{if } \omega > 0 \end{cases} \tag{5.3}$$

The Hilbert transform induces a phase shift of $\pi/2$ for negative frequency component and $-\pi/2$ for positive frequency components. For example, if the Hilbert transform is applied to the real cosine signal $\cos(\omega\mathrm{t})$, it is converted to the sine signal, $\sin(\omega\mathrm{t})$. For fringe analysis, a sinusoidal fringe pattern can be mathematically described as,

$$I(x,y) = A(x,y) + B(x,y)\cos\left[\phi(x,y)\right], \tag{5.4}$$

where $A(x,y)$ is the average intensity, $B(x,y)$ is the intensity modulation, $\phi(x,y)$ is the phase to be solved for. To retrieve the phase by using the Hilbert transform, the DC component of the fringe pattern should be removed in advance. The proposed method directly uses the average intensity $A(x, y)$ to calculate the difference map by subtracting the DC component from the fringe image before applying the Hilbert transform, which can be described as,

$$I_{DC}(x, y) = A(x, y), \tag{5.5}$$

$$I_d(x, y) = I(x, y) - I_{DC}(x, y) = B(x, y)\cos[\phi(x, y)], \tag{5.6}$$

where the subscript $_d$ means the difference map. Then, we can apply the Hilbert transform as,

$$I_d^* = \mathcal{H}\left[I_d(x, y)\right] = B(x, y)\sin\left[\phi_L(x, y)\right], \tag{5.7}$$

where the superscript * means the Hilbert transformed image. According to aforementioned property, the phase of the transformed image has been shifted in $\pi/2$. Then, the phase can be retrieved by using an arctangent function,

$$\phi(x, y) = \tan^{-1}\left[\frac{I_d^*}{I_d}\right]. \tag{5.8}$$

The phase obtained from Eq. (5.8) ranges from $-\pi$ to $+\pi$. To solve 2π discontinuities, the process of numbering each period to add multiples of 2π is required, which is called phase unwrapping.

$$\Phi(x, y) = 2\pi \times K(x, y) + \phi(x, y), \tag{5.9}$$

here $K(x, y)$ is fringe order, the multiples of 2π to be added to the wrapped phase. If the wrapped phase is unwrapped by adding multiples of 2π with uniquely defined fringe order $K(x, y)$, the unwrapped phase is regarded as absolute phase. In the next section, we will introduce a method for retrieving absolute phase map by determining fringe order $K(x, y)$ using geometric constraints.

5.2.2 Enhanced two-frequency phase unwrapping method

This method used predefined geometric constraints to determine the fringe order $K(x, y)$ for solving 2π discontinuities mentioned in the previous section [80]. A standard DFP system consists of a single camera and a single projector, which are calibrated under the same coordinate system and follows a linear pinhole model. The pinhole model of each optical device can be mathematically described as,

$$s^c \left[u^c v^c 1\right]^t = \mathbf{P^c} \left[x^w y^w z^w 1\right]^t , \tag{5.10}$$

$$s^p \left[u^c v^c 1\right]^t = \mathbf{P^p} \left[x^w y^w z^w 1\right]^t , \tag{5.11}$$

where $\mathbf{P}$ means a 3×4 projection matrix, superscript ^{c} denotes camera, and superscript ^{p} denotes projector, and ^{t} denotes the transpose operation of a matrix. The projection matrices $\mathbf{P}^c$ and $\mathbf{P}^p$ indicate the relationship between 3D world coordinate and 2D image plane and these matrices are estimated by calibration [74]. After determination of the matrices $\mathbf{P}^c$ and $\mathbf{P}^p$, Eqs. (5.10) and (5.11) provide 6 equations and have 7 unknowns (s^c, s^p, x^w, y^w, z^w, u^p, v^p) for a camera pixel (u^c, u^v). To solve all unknowns uniquely, one additional constraint is required. The absolute phase Φ provides us with one more constraint to reconstruct 3D geometry (x^w, y^w, z^w).

On the other hand, if we set an artificial ideal plane at $z = z^w$, each pixel on the camera sensor can be uniquely matched to a pixel on the projector sensor with its predefined phase value. The artificial generated phase map is called as minimum phase map, Φ_{min}, which is determined by z_{min}, fringe period T and projection matrices $\mathbf{P^c}$ and $\mathbf{P^p}$,

$$\Phi_{min}(u^c, v^c) = f(z_{min}; T, \mathbf{P^c}, \mathbf{P^p}). \tag{5.12}$$

Then, the fringe order can be determined within a given depth range as

$$K(x, y) = ceil\left[\frac{\Phi_{min} - \phi}{2\pi}\right], \tag{5.13}$$

where $ceil[]$ means an operator that returns the closest upper integer value. Although the method using geometric constraints recovers the phase accurately, there is a limitation that the unwrapped phase is correct when the object is in a specific depth range. Assuming the angle between the principle axis of the projector and the camera is θ and the spatial span of one projected fringe period is Δy, we can calculate the maximum depth range as,

$$\Delta z_{max} = \Delta y / \tan\theta. \tag{5.14}$$

Therefore, if we used a narrow fringe pattern for absolute phase retrieval, it is obvious that the available depth range for 3D shape measurement is very restricted. To overcome the limited depth range problem for the narrow fringe pattern, the proposed method used another set of fringe patterns at different frequency. By repeating the same procedures using Eqs. (5.6)-(5.8), we can obtain two-frequency phase. With these two-frequency phase and the geometric constraints, we can apply the enhanced two-frequency phase unwrapping method [81]. First, the low-frequency phase is unwrapped with the geometric constraints by using Eqs. (5.9) and (5.13), which provide larger depth range than the depth range which the high-frequency can have. The high-frequency phase can be unwrapped by referring the unwrapped low-frequency phase. The fringe order of the high-frequency can be defined as,

$$K(x,y) = Round\left[\frac{\Phi^L(x,y)\frac{T^L}{T^H} - \phi^H(x,y)}{2\pi}\right], \tag{5.15}$$

where the superscript ^{L} means the low-frequency, ^{H} the high-frequency, and Φ the unwrapped phase.

In summary, we implemented a hybrid approach based on two major principles mentioned above to reconstruct 3D. Figure 5.1 illustrates a schematic diagram of the computational framework of the proposed method. We used only three patterns to retrieve absolute phase, which are one high-frequency (i.e. fringe period = 18 pixels) pattern, one low-frequency (i.e. fringe period = 108 pixels) pattern and one DC component pattern. To obtain two different frequency phase maps, the Hilbert transform was applied to each difference map between the fringe pattern and its DC component. Then, the absolute phase for 3D shape measurement can be robustly retrieved by using the enhanced two-frequency unwrapping method.

5.3 Experiment

We designed a high-speed 3D shape measurement system to evaluate our proposed method. The system consists of a CMOS camera (Model: Vision Research Phantom 340L) and a DLP projector (Model: Wintech PRO 6500). The camera lens (Model:

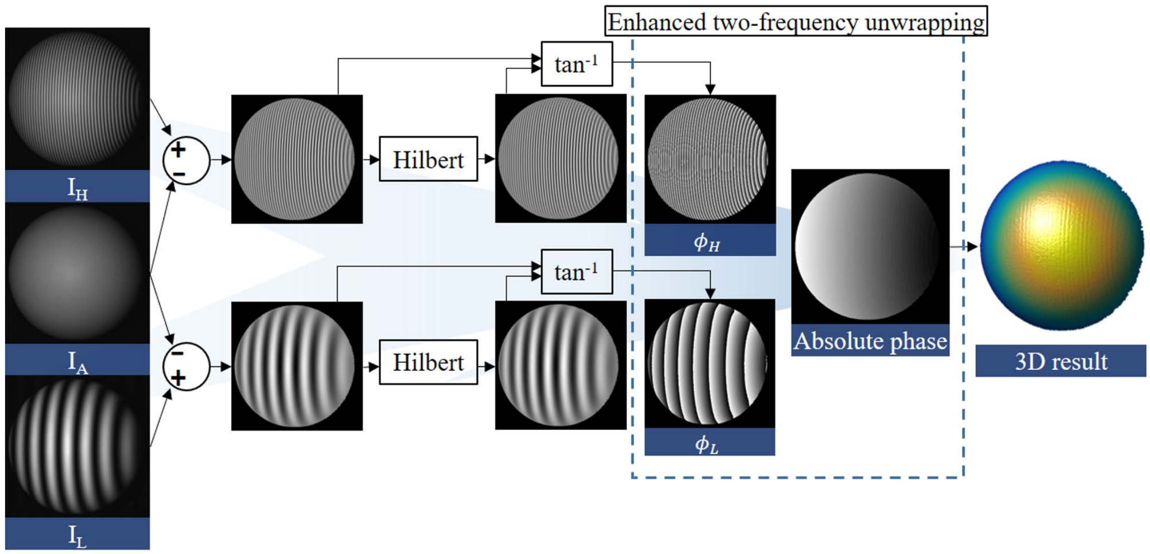

Fig. 5.1. Computational framework of the proposed method.

SIGMA 24 mm f/1.8 EX DG) has a 24 mm focal length and an aperture ranging from f/1.8 to f/22. The projector and camera are precisely synchronized with a microprocessor (Model: Arduino Uno) to project and capture the fringe images simultaneously. The image resolutions for the camera and the projector are 640 $\times$ 800 and 1920 $\times$ 1080 respectively. All images are cropped in the same way for better visualization. For all experiments, binary optimized dithered patterns were used for measuring dynamic motions [82]. The high-frequency pattern has 18-pixel fringe period and the low-frequency pattern has 108-pixel fringe period. Figure 5.2 shows the photograph of the system. We calibrated the system using the method developed by Li et al [74].

First, we measured a smooth sphere with a diameter of 200 mm for static object experiment. We set the exposure time of the camera and projector as 500 μs. Figures 5.3(a)- 5.3(c) show the DC component, the low-frequency fringe image, and the high-frequency fringe image respectively. Prior to applying the Hilbert transform, the difference map was obtained by subtracting the DC component from each fringe pattern using Eq. (5.6) and the result for low-frequency is shown in Fig. 5.3(d). Then, we

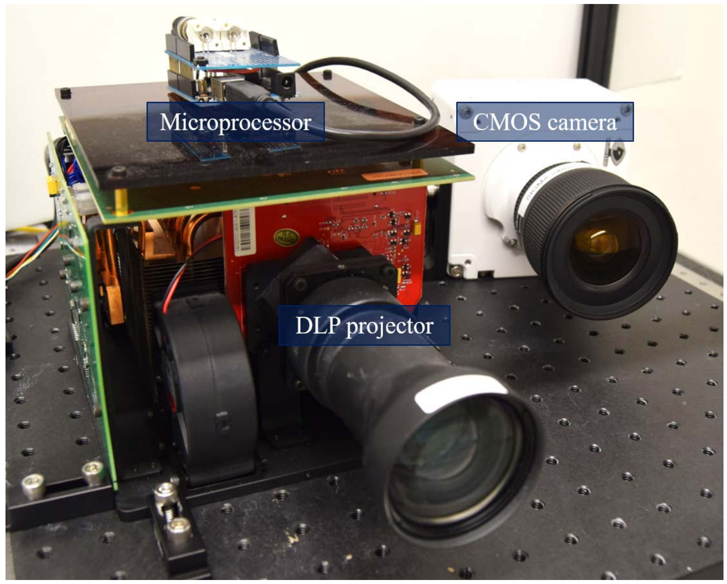

Fig. 5.2. Experimental setup for DFP system.

generated the Hilbert transformed image shown in Fig. 5.3(e). With these captured and transformed patterns, we calculated the wrapped phase for low-frequency using Eq. (5.8), as shown in Fig. 5.3(f). The same phase-retrieval procedures were applied to high frequency and the high-frequency wrapped phase is shown in Fig. 5.3(g). For absolute phase retrieval, we implemented the two-frequency phase unwrapping method [81]. To unwrap the wrapped phase, the method utilized the geometric constraint, which is an artificial plane at the predefined minimum depth, z_{min}. Figure 5.3(h) shows the absolute phase. For better visualization, the mask was applied to Figs. 5.3(d)-5.3(h) to remove the background. The 3D result is shown in Fig. 5.3(i).

Then, we measured a plaster statue, which has complex geometry shown in Fig. 5.4(a). Figure 5.4(b) shows the low-frequency fringe image and Fig. 5.4(c) shows the high-frequency fringe image. The same procedures were implemented on the images of the statue captured by the high-speed measurement system. As shown in Fig. 5.4(d), the 3D result shows the details of the sculpture. The 3D result verifies that the proposed method using the hybrid approach with Hilbert transform and the

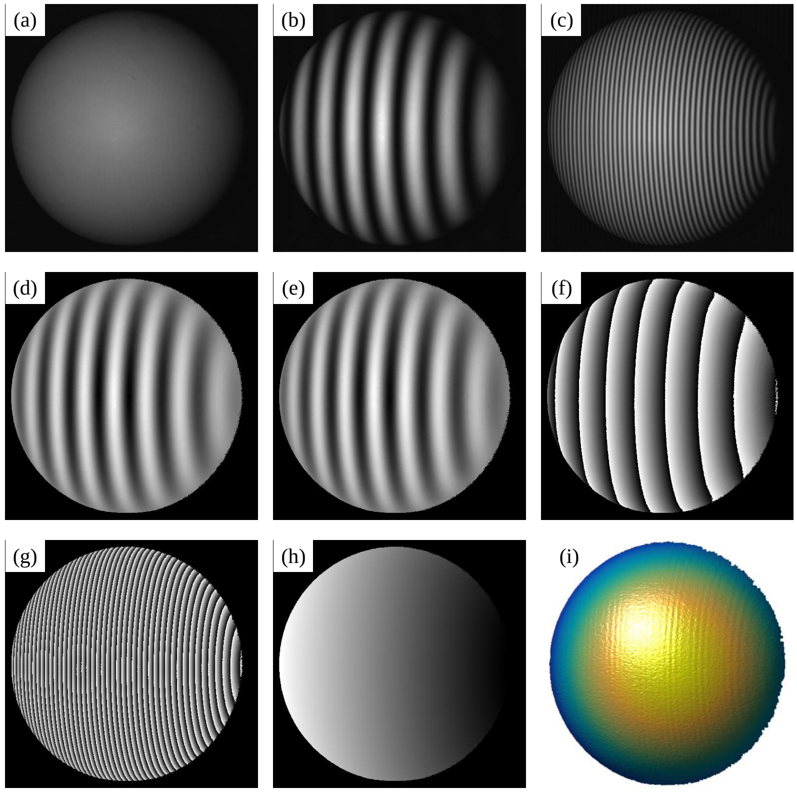

Fig. 5.3. Experimental results of a uniform sphere using the proposed method. (a) DC component fringe image; (b) low-frequency fringe image; (c) high-frequency fringe image; (d) difference map of low-frequency fringe image; (e) Hilbert-transformed map of low-frequency; (f) low-frequency wrapped phase; (g) high-frequency wrapped phase; (h) unwrapped phase map using geometric constraints; (i) 3D reconstruction result.

enhanced two-frequency unwrapping method reconstructs the 3D geometry accurately with only three patterns.

To demonstrate the performance of our proposed method for dynamic applications, we did the high-speed 3D shape measurement with fast-moving objects. The flapping robotic bird (Model: XTIM Bionic Bird Avitron V2.0) was used for dynamic motion experiments. We set the speed of the flapping wing as 11 cycles per second. For the high-speed 3D measurement system, we set the capturing speed at 6,000 Hz, which is same as the projection speed. The exposure time of the camera is 160 μs. We

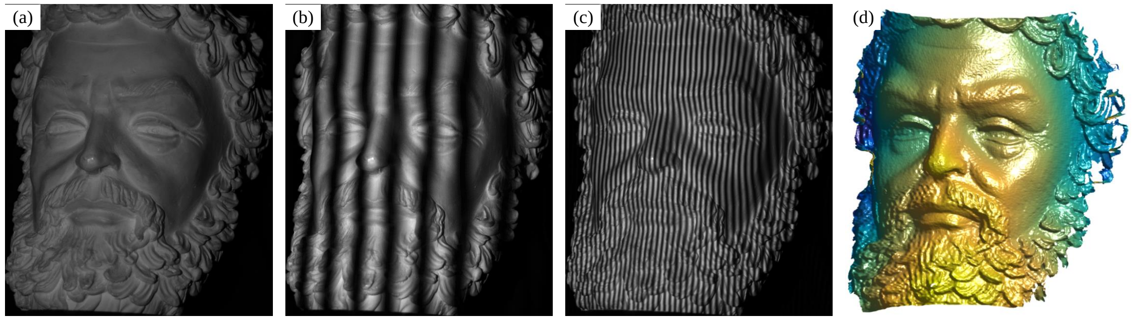

Fig. 5.4. Experimental results of a complex sculpture using the proposed method. (a) DC component of the measured statue; (b) low-frequency fringe image; (c) high-frequency fringe image; (d) 3D reconstruction result.

got the 3D capturing speed of 2,000 Hz under the settings, since we used only three patterns to reconstruct one 3D geometry. Figure 5.5(a) shows a representative image used for 3D reconstruction. Figures 5.5(b)-5.5(d) shows the reconstructed 3D results using a set of three patterns. The dynamic 3D result is shown in its associated video (Video 1). We also measured falling balls to evaluate the proposed method. The same settings and computational framework were applied to the experiment. Figure 5.6(a) shows a representative image and Figs. 5.6(b)-5.6(d) are 3D results. The 3D result with multiple balls is in its associated video (Video 2). As mentioned before, the proposed method reduces motion induced error caused by the time lapse between the captured images, since only one fringe image and the DC component are required to retrieve the wrapped phase at one frequency. Experimental results of the dynamic motions successfully proved that the proposed method accurately reconstructed 3D geometries at high speed.

5.4 Summary

This chapter has presented a high-speed 3D absolute shape measurement method using only three patterns. The proposed method used the Hilbert transform to obtain phase information directly from one fringe image and the DC component. Also,

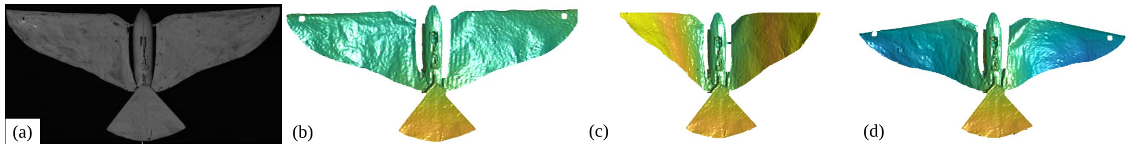

Fig. 5.5. Measurement result of a flapping bird robot in high-speed. (a) DC component of the fringe images at the specific moment; (b)-(d) 3D reconstruction results (Video 1, MPEG, 5.9 MB).

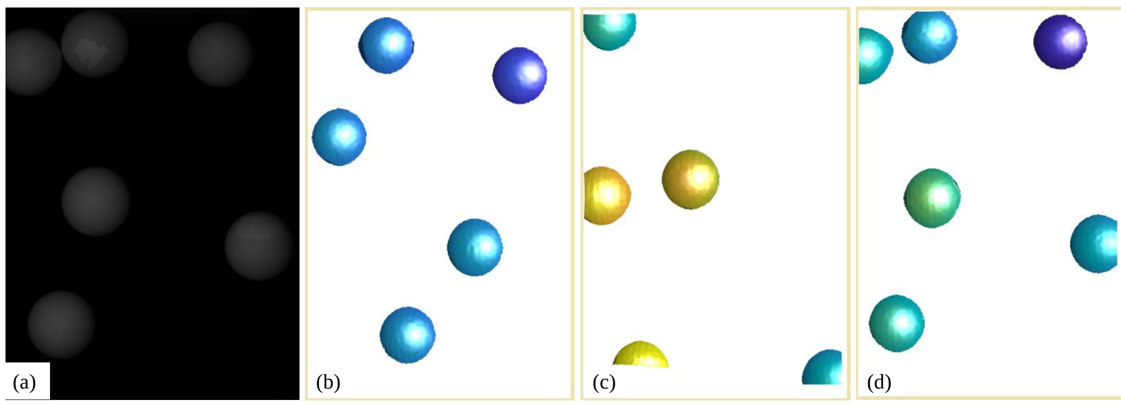

Fig. 5.6. Measurement result of falling multiple balls in high-speed. (a) DC component of the fringe images at the specific moment; (b)-(d) 3D reconstruction results (Video 2, MPEG, 3.8 MB).

the absolute phase can be retrieved accurately using the enhanced two-frequency unwrapping method. To maximize the projection speed and get higher accuracy, we used optimized binary dithering technique. Our dynamic experimental results demonstrated that high-quality 3D shape measurement can be realized at a speed of 2,000 Hz.

6. HIGH-SPEED AND HIGH-ACCURACY 3D SURFACE MEASUREMENT USING A MECHANICAL PROJECTOR

6.1 Introduction

Due to high resolution, high speed, and flexibility of implementation, 3D shape measurement techniques using DFP and phase-shifting algorithms have been extensively used in science, engineering, as well as industrial applications [83].

Phase-shifting algorithms are widely used for 3D reconstruction through fringe analysis because of their accuracy, speed, and robustness to noise. However, a typical phase-shifting algorithm can only provide the phase value ranging from $-\pi$ to π with 2π discontinuities, and such phase is often referred as wrapped phase. A phase unwrapping algorithm has to be implemented to remove those 2π discontinuities to create a smooth phase before 3D reconstruction. In the history, numerous phase unwrapping algorithms have been developed but they can be generally classified into two categories: spatial and temporal unwrapping algorithms. The spatial unwrapping algorithm analyzes the wrapped phase map itself and determines the number of 2π to be added to a point assuming the object surface is smooth at least on one path [36,50]. Since spatial phase unwrapping does not require any additional information acquisition, such a method does not affect 3D data acquisition speeds. However, regardless the robustness of a spatial phase unwrapping algorithm, it is fundamentally limited to measure "smooth" object (e.g., no abrupt geometry changes, or isolated patches). Temporal phase unwrapping algorithms, in contrast, solve the discontinuity problem by acquiring additional information temporally. There are numerous temporal unwrapping algorithms including two- [59], or multi-frequency [52] phase-shifting, and the gray-coding plus phase-shifting [53]. Since temporal phase unwrapping algorithms do not require surface to be smooth, they can be used to measure arbitrary objects. However, the measurement speed is slowed down because the requirement of additional information acquisition at different time.

To address the speed limitations of conventional temporal phase unwrapping methods, researchers have attempted to simultaneously capture images from a different perspective and utilized the secondary camera images to provide cues for phase unwrapping [84–90]. Such methods use geometric constraints along with other knowledge of the system or the object to determine the number of 2π to be added for each point. Though successful, the phase unwrapping process is typically very slow in nature due to the backward and forward checking [91].

On the other hand, texture-based standard stereo-vision techniques have been well developed, and numerous global or semi-global stereo-matching algorithms [92–97] have developed to find the corresponding point. For example, the cost-based matching approach calculate the cost on the texture difference between a region near a source point on one image and the small region near a target point on the other image [25], and the corresponding point is determined by minimizing or maximizing the cost function. The stereo-matching algorithm typically generates a disparity map, a map that stores the pixel shift of a corresponding pairs from one camera image to the other camera image. The disparity map is then used to reconstruct 3D coordinates for each point based on the calibrated parameters of the stereo vision system. Since it only uses two cameras, the stereo-vision technique has obvious advantages: the simplicity of hardware configuration and straightforward calibration for the system [98]. However, hinging on natural texture variations to establish corresponding points, the accuracy of stereo-vision techniques varies from one object to another; and the measurement accuracy is not high if an object has no obvious distinctive features.

Lohry and Zhang [46] developed a 3D shape measurement technique that embraced the advantages of a standard stereo-vision technique (e.g., speed and simplicity) and those of the phase-shifting method (e.g., accuracy). In lieu of relying on nature texture images, such a method projects a locally unique statistical pattern along with the sinusoidal fringe patterns to increase to the robustness of stereo matching, and then uses the phase constraint to improve the accuracy of stereo matching. In particular, Lohry and Zhang employed the Efficient LArge-scale Stereo (ELAS) algorithm [99] to obtain rough disparity map and then a local linear regression approach to refine the disparity map for more accurate 3D reconstruction. Instead of using the linear regression method for refinement, Song et al. [100] developed an algorithm to refine the rough correspondence by interpolating two points: one point obtained from the standard stereo-vision algorithm that uses texture images and the other point obtained from phase map. Gai et al. [101] projected a separate speckle pattern to generate corresponding pairs and chose a proper correlation window size to remove outliers. Liu and Kofman [102] proposed to insert a background offset value into fringe patterns to provide clues for better correct corresponding point establishments. Furthermore, they used binary pattern to reduce the probability of incorrect corresponding point determination. These additional research effort could improve measurement speed, robustness, or/and accuracy, yet it is difficult for any of these approaches to achieve sub-pixel level accuracy.

As mentioned earlier, the DFP techniques has the advantage of speed, accuracy, flexibility, yet they all use a silicon-based digital projection devices such as liquid crystal display (LCD) or DLP projectors. The silicon based projection devices can only operate properly within a limited spectrum light range and a certain level light power. For example, the DLP projection system uses the silicon-based DMD, if the wavelength of light is over 2,700 nm or below 300 nm, the transmission rate drops significantly [103].

To overcome the spectrum limitation of DFP techniques, Heist et al. [104] developed a 3D shape measurement system using two cameras and one mechanical projector with a rotating wheel. The rotating wheel has open and close slots to represent ON/OFF of the light. By properly defocusing lens, aperiodic sinusoidal patterns can be generated on the object surface. Since the projector does not use the silicon-based device for pattern generation, the light spectrum of the GOBO projector can be substantially broadened for applications such as 3D thermal imaging [105]. However, 3D shape measurement is realized by capturing a sequence phase-shifted fringe patterns, and then applying the stereo-matching algorithm to a pair of phase maps captured from different perspectives. Even though high speed data acquisition was realized, such a method did not precisely synchronize the projector with the camera and thus precise phase shifts cannot be ensured. Furthermore, the correspondence establishment still largely relies the computationally intensive backward-and-forward checking.

To further embrace the broad spectrum band of the mechanical projection technology, yet mitigate the limitations of the method developed by Heist et al. [104], this chapter presents a method that can achieve both high-speed and high-accuracy 3D shape measurement. The major difference between the proposed method and that developed by Heist et al. [104] are: (1) we use a rotating wheel with equally spaced ON/OFF structures that create periodical sinusoidal fringe patterns; (2) our cameras are precisely synchronized with the projector such that fringe patterns with precise phase shifts can be acquired for precise phase reconstruction; (3) we insert a transparent film with locally unique statistical patterns such that the stereo matching can be more efficiently established using a standard stereo-vision algorithm (e.g., ELAS algorithm); and 4) we develop a novel computation framework that can achieve subpixel stereo matching accuracy by using the phase constraint. Our prototype hardware system can accurately measure both single and multiple isolated objects, and the same hardware prototype system can potentially achieve 10,000 Hz 3D shape measurement speeds regardless the number of phase-shifted fringe patterns required for one 3D reconstruction.

Section 6.2 explains the principle behind the proposed method. Section 6.3 presents experimental results to verify the performance of the proposed method. Section 6.4 discusses the advantages and shortcomings of the proposed method, and finally Sec. 6.5 summarizes the paper.

6.2 Principle

6.2.1 Least squares algorithm

Due to their speed, accuracy, and resolution, phase-shifting based 3D shape measurement techniques have been extensively used in the field of 3D optical metrology [60]. Assume the intensity of k-th fringe image can be described as,

$$I_k(x, y) = I'(x, y) + I''(x, y) \cos[\phi(x, y) - \delta_k], \quad (6.1)$$

where $I'(x, y)$ is the average intensity, $I''(x, y)$ the intensity modulation, and $\phi(x, y)$ the phase to be solved for, and δ_k the phase-shift value. Theoretically, only three patterns are required to compute phase per pixel if the phase-shift values between fringe patterns are precisely known. Yet, using more fringe patterns can increase phase quality and, to various degree, tolerate phase error introduced by non-sinusoidality, imprecise phase shift, etc. The phase can be retrieved by applying a least square algorithm for equally phase-shifted fringe patterns (i.e., $\delta_k = 2\pi k/N$),

$$\phi(x, y) = -\tan^{-1}\left[\frac{\sum_{k=1}^{N} I_k(x, y)\sin\delta_k}{\sum_{k=1}^{N} I_k(x, y)\cos\delta_k}\right]. \quad (6.2)$$

Due to the use of an arctangent function in Eq. (6.2), the obtained phase value ranges from $-\pi$ to π with 2π discontinuities . In general, a spatial or temporal phase unwrapping algorithm should be employed to remove 2π discontinuities and create smooth phase called unwrapped phase that can then be used for 3D reconstruction. As discussed before, the spatial phase unwrapping algorithm [36, 50] determines 2π discontinuities by assuming the smoothness of the surface and thus cannot be used to measure a single object with abrupt geometry changes or simultaneously measure multiple isolated objects. Temporal phase unwrapping algorithms, in contrast, can fundamentally eliminate the limitation of spatial phase unwrapping algorithms. Yet, they slow down the measurement speed by requiring the acquisition of additional images, which is not desirable for high-speed applications.

In the meantime, N phase-shifted fringe patterns can be used to obtain $I'(x,y)$ by

$$I'(x,y) = \left[\frac{\sum_{k=1}^{N} I_k(x,y)}{N}\right]. \tag{6.3}$$

$I'(x,y)$ is often regarded as the texture image, the photograph of the object without fringe stripes. The texture image can be used for visualization, or providing additional information for analysis.

6.2.2 Phase-shifted sinusoidal fringe pattern generation with a mechanical projector

As discussed in Sec. 6.1, we developed a mechanical projector for high-speed 3D shape measurement. Figure 6.1 shows the system configuration. It includes a fiber light source, a rapidly rotating wheel , a statistical pattern transparent film, and two lenses (Lens 1 and 2). The fiber light passes through Lens 1 to create a bright area on the rotating wheel that is an optical chopper (Model: Thorlabs MC2000). The rotating wheel has two optical proximity sensors to sense the slot speed and generates a square wave that is represents the timing of the slot rotation. The rotating wheel has evenly spaced open and close slots that respectively pass through (ON) or block (OFF) the light to create structured patterns on the wheel. The lens (Lens 2) is projection lens that creates the image of the structured patterns on the object. The structured patterns become pseudo sinusoidal if the the object is properly placed at a out-of-focus depth position of Lens 2. Due to the use of a transparent film with statistical pattern on the optical path, the structured patterns formed on the object are modulated by such a statistical pattern. The rationale of adding statistical pattern will be detailed in Subsec. 6.2.4

Since the wheel is rotating, phase-shifted fringe patterns are naturally generated if sampled at a different time. For high-accuracy measurement, capturing precisely phase-shifted fringe patterns is critical. In this research, we achieve high-accuracy

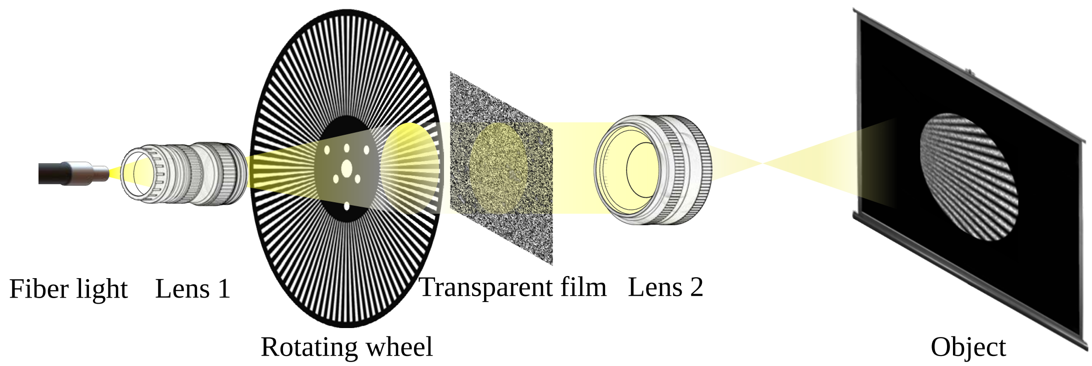

Fig. 6.1. Schematic diagram of the mechanical projection system.

and high-speed 3D shape measurement through precise synchronization between the projector and the camera. A high-performance microprocessor (Model: Raspberry pi 2) takes the square wave generated by the mechanical projector and calculates the trigger signal period as

$$T^c = T^s/N, \tag{6.4}$$

where T^s is the period of square wave representing the projection period of each slot, T^c is period of the trigger signal sent to the cameras, N is the number of phase-shifted fringe patterns necessary for one 3D reconstruction. Assuming the angular velocity of the rotating wheel is ω, and there are M number of evenly spaced slots on the wheel, the slot speed can be calculated as,

$$f^s = \frac{\omega}{2\pi \times 60} \times M$$

in Hz. The microprocessor generates a periodical pulse trigger signal that is sent to both high-speed cameras for image acquisition.

Figure 6.2 illustrates the timing chart of the proposed system. For example, if a slot speed $f^s = 1,000$ Hz, or $T^s = 1$ ms, is setup for the projector, the 1,000 Hz square wave is generated by the projector (i.e., $500\mu s$ ON and $500\mu s$ OFF slot time). If a three-step phase-shifting algorithm ($N = 3$) is used, the trigger signal period, from Eq. (6.4) is approximately $T^c = 333\mu s$; and thus three equally spaced pulses are generated within 1 ms. Similarly, if a four-step phase-shifting algorithm

($N = 4$) is used, four equally spaced pulses are generated within 1 ms period, or $T^c = 250\mu s$. In general, the camera exposure time t^{exp} should not be longer than the trigger pulse period, i.e., $t^{exp} \leq T^c$. This timing chart indicates that, as long

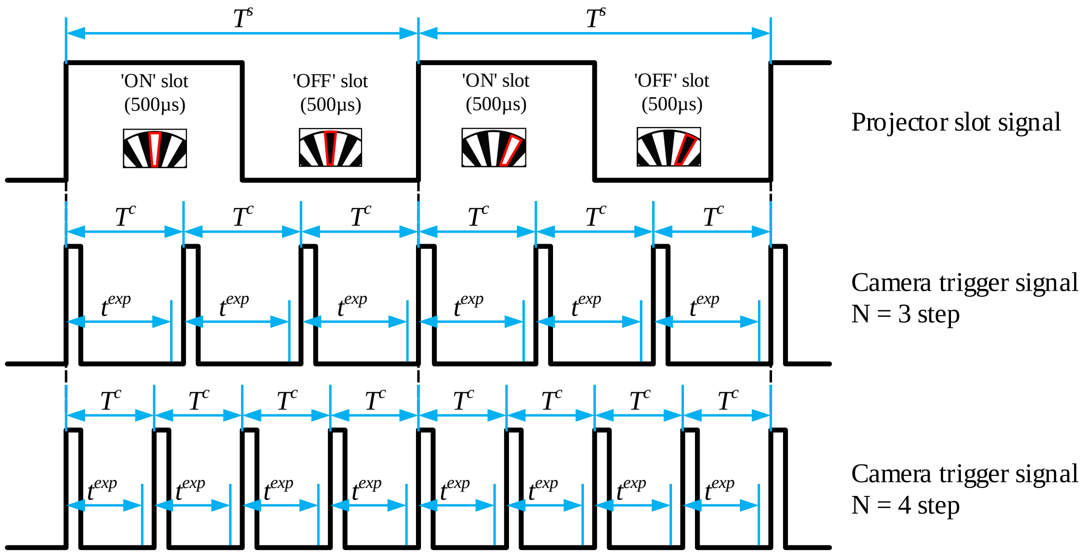

Fig. 6.2. Timing diagram for the proposed high-speed 3D shape measurement system. Here T^s represents the period of the slot projection; T^c represents the period of the signal generated by the microprocessor to trigger both high-speed cameras; t^{exp} represents the exposure time of the camera; and N represents the number of phase-shifted fringe patterns required for one 3D reconstruction.

as the camera's sampling speed is high enough, the time required to capture one 3D frame is solely determined by the slot period T^s, and is independent of the number of phase-shifted fringe patterns required for one 3D reconstruction. In contrast, for a standard DFP system, if the projector's image refreshing rate is fixed, the time required to capture one 3D frame is proportional to the number of fringe patterns required for 3D reconstruction, resulting in a slower measurement speed for higher accuracy measurement when more fringe patterns are required. Therefore, for high-speed and high-accuracy 3D shape measurement applications, our proposed technique is advantageous.

6.2.3 Computational framework to achieve sub-pixel matching accuracy

Figure 6.3 shows the overall computational framework that we developed in this research. Two high-speed cameras precisely synchronized with the projector capture two sets of phase-shifted fringe patterns of the object from different perspectives. Applying Eq. (6.3) to the captured fringe images by each camera yields one texture image from each perspectives. We apply a standard stereo-matching algorithm, i.e., the ELAS algorithm [99], to generate a rough disparity map (a map representing the corresponding point) that can be used to reconstruct a coarse 3D shape of the object. Each set of phase-shifted fringe patterns can also generate a wrapped phase map by applying a phase-shifting algorithm. Theoretically, if a corresponding point is precise, the wrapped phase should be identical, and thus we apply this wrapped phase constraint to refine the rough disparity to achieve sub-pixel correspondence accuracy for higher accuracy 3D reconstruction.

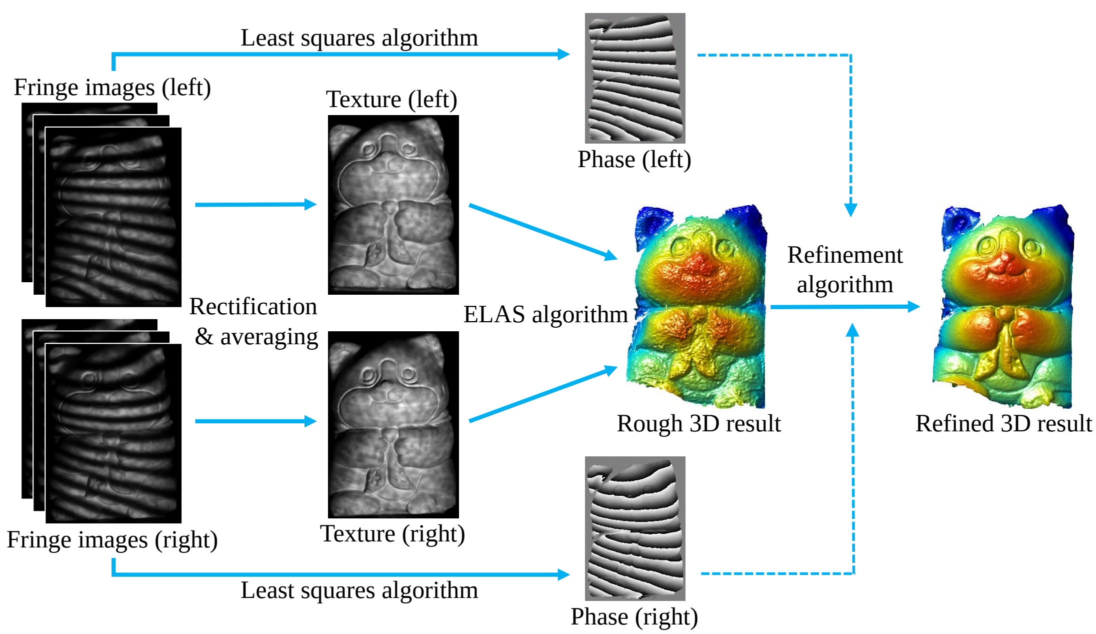

Fig. 6.3. Computational framework of our proposed 3D reconstruction method.

This subsection details the proposed computational framework. We will also briefly explain the epipolar geometry that is critical to understand the proposed method.

6.2.4 Epipolar geometry

The standard stereo-vision algorithm typically uses the *epipolar geometry* to increase the robustness and speed of the stereo matching. Epipolar geometry essentially describes the intrinsic projective geometric constraints of the stereo-vision system. Figure 6.4 illustrates the fundamental concept of the epipolar geometry. O^l and O^r describe the focal point for the left camera lens and the focal point for the right camera lens, respectively. E^l and E^r are the points of intersection of the line $\overline{O^l O^r}$ with two image planes, and these points are called *epipoles*. For a pixel P^l on the left camera image, the corresponding pixel on the right camera can be one of the points, P_1, P_2, P_3, depending on the depth information in a 3D space. Even though each point corresponds to a different depth, all these points must fall on the same line on the right camera image L^r, which is called *epipolar line*. With similar geometric relationships, all points on the line L^l can only be matched to points on line L^r, and the plane formed by P^l, O^l, and O^r is called *epipolar plane*. Therefore, applying epipolar geometry constraint essentially simplifies the complex two-dimensional searching problem to be a simple one-dimensional searching problem, and thus increases the searching speed and could enhance the robustness of the algorithm.

To further improve the correspondence searching speed, the stereo images are rectified such that the matching point only occurs on the same row; and this procedure is often referred as *image rectification*. Image rectification essentially translates and rotates the original images to align those epipolar lines (e.g., make L^l and L^r on the same line) using the stereo-vision system calibration data. Figure 6.5 shows an example of the image rectification. Figure 6.5(a) shows the original image captured by the left camera. After rectification, the image is slightly distorted, as shown in

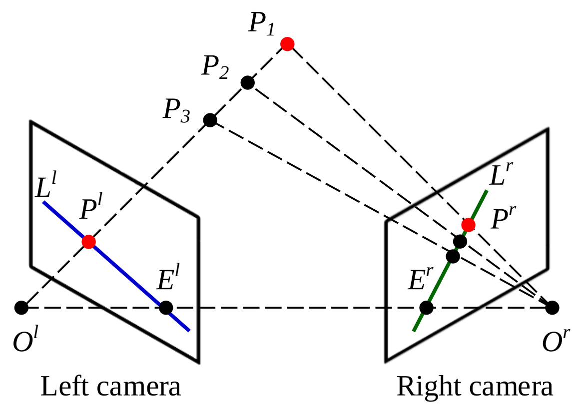

Fig. 6.4. Illustration of epipolar geometry for a stereo-vision system.

Fig. 6.5(b). Similarly, the image captured by the right camera can also be also rectified. Figure 6.5(c) shows the result after putting these two rectified images together, where the green horizontal lines $(v_1, v_2, \ldots)$ represent the epipolar lines. To search for the correspondence point for a given point the left camera image, one only have to search the points on the same green line on the right image.

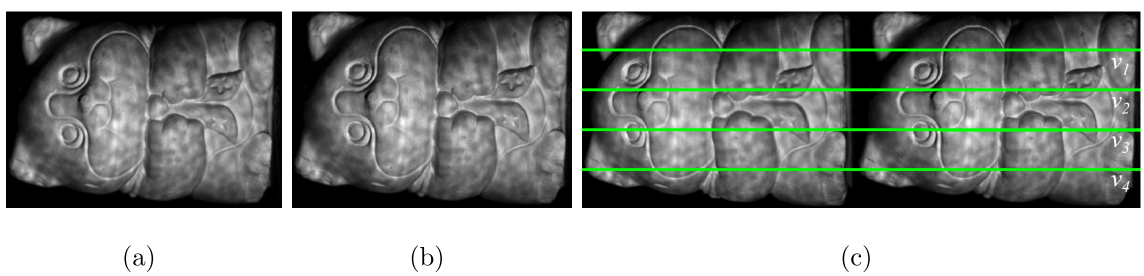

Fig. 6.5. Image rectification to facilitate correspondence searching. (a) Texture image captured by the left camera; (b) rectified image of (a); (c) a pair of rectified images for stereo matching, horizontal green lines $(v_1, v_2, \ldots)$ show representative epipolar lines.

Even though the epipolar geometry makes the searching process simpler and more robust, it may not be enough to determine the exact corresponding pairs from the nature texture if the object does not have texture variations. To alleviate this problem, Lohry and Zhang [46] proposed to encode a statistical pattern into the phase-shifted patterns to make the projected texture locally unique. Different from the DLP projector which can generate those encoded images digitally, we printed out the statistical pattern on a transparent film and placed next to the spinning wheel on the optical path, as shown in Fig. 6.1.

6.2.5 Refinement algorithm

Although using epipolar geometry makes it easier to find the corresponding pairs, and encoding additional statistical pattern onto the projected fringe patterns further increases the robustness, one of the fundamental limitation of the standard stereo-vision algorithm is that it is difficult to achieve correspondence at a scale much smaller than the feature size, not to say at a sub-pixel level. As a result, applying the standard stereo-vision algorithm only gives coarse measurement. As explained earlier, the phase value obtained from phase-shifted patterns can be used as an additional constraint to improve correspondence accuracy and thus 3D shape measurement accuracy.

The step of using phase constraint to further improve correspondence point determination accuracy is called *refinement*. The proposed refinement algorithm is fundamentally based on the assumption that if the pairs correspond to each other, the phase values calculated by the images taken by both cameras must be the same. Therefore, the phase maps can be used to refine the rough disparity map. The following steps describe how phase is used to achieve sub-pixel corresponding accuracy:

- *Step 1: Find rough corresponding point using epipolar geometry.* By employing the ELAS algorithm and using epipolar constraints, we determine the corresponding point on the right camera image for a given point on the left camera image acquired simultaneously. As described previously, the standard stereo-vision algorithm only provides a rough disparity map, or roughly determines the corresponding points.

  Figure 6.6 illustrates an example of the roughly corresponding point $P^r(u_0^r, v)$ on the right camera image for a given point $P^l(u^l, v)$ on the left camera image;

and we call Point $P^r(u_0^r, v)$ as the rough disparity point corresponding to Point $P^l(u^l, v)$. Apparently, the matching point must be on an epipolar line v.

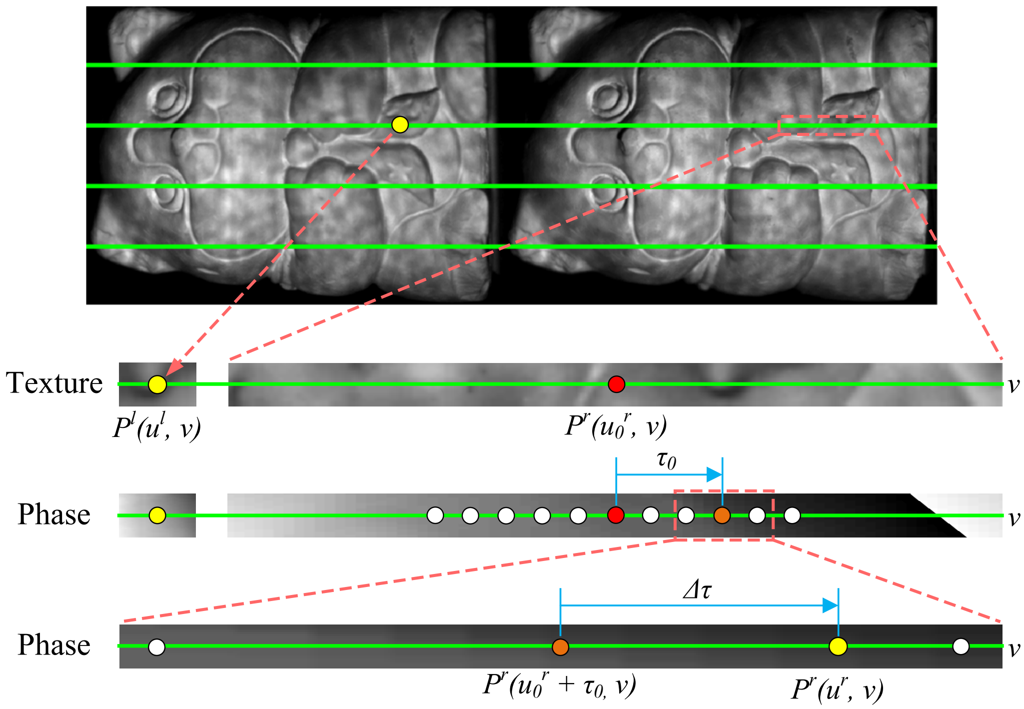

Fig. 6.6. Graphical illustrations of the proposed disparity map establishments on one epipolar line v. The first row image shows two rectified images; the second row image illustrates the rough corresponding point establishment using the standard stereo-vision algorithm on the rectified texture image; the third row image illustrates that first step of refinement by applying the phase constraint, e.g., the initial corresponding point $P^r(u_0^r, v)$ is shifted by τ_0 to $P^r(u_0^r + \tau_0, v)$; and the bottom row image shows the last refinement stage by subpixel interpolation, further move $P^r(u_0^r + \tau_0, v)$ by $\Delta\tau$ to the ultimate matching point $P^r(u^r, v)$.

- *Step 2: Apply phase constraint to more precisely locate the corresponding point.* The rough disparity map obtained from Step 1 can be refined by applying the phase constraint. Because the texture image and the phase image are perfectly aligned, the rough disparity point determined from the previous step has underline corresponding phase value for the same point. Assume for the disparity value between Point $P^l(u^l, v)$ and Point $P^r(u_0^r, v)$ determined from texture image is $d_0 = u_0^r - u^l$. The precisely matching point could be on the left or on the right of the (u_0^r, v). In this research, we search ± 5 pixels and determine the more precisely corresponding point $P^r(u^r + \tau_0, v)$ by satisfying

$$\left[\phi^r(u^r + \tau_0, v) - \phi^l(u^l, v)\right] \cdot \left[\phi^r(u^r + \tau_0 + 1, v) - \phi^l(u^l, v)\right] \leq 0, \tag{6.5}$$

where τ_0 is the additional disparity shift along u^r direction on the epipolar line v.

- *Step 3: Determine sub-pixel accuracy correspondence through linear interpolation.* After applying Step 2, now the true precisely corresponding point for Point $P^r(u^r, v)$ should be within $[u^r + \tau_0, u^r + \tau_0 + 1]$; and the subpixel shift $\Delta\tau$ can be determined by linearly interpolating these two points using

$$\Delta\tau = \frac{\phi^l(u^l, v) - \phi^r(u^r + \tau_0, v)}{\phi^r(u^r + \tau_0 + 1, v) - \phi^r(u^r + \tau_0, v)}. \tag{6.6}$$

Combining the initial disparity d_0, the additional shift after applying the phase constraint τ_0, and the subpixel shift $\Delta\tau$, we can calculate the precise disparity d between the left camera point and the corresponding right camera point as,

$$d = d_0 + \tau_0 + \Delta\tau = u_0^r - u^l + \tau_0 + \Delta\tau. \tag{6.7}$$

Once the precise disparity map is established, 3D coordinates for each pixel can be calculated using a standard stereo-vision 3D reconstruction algorithm.

6.3 Experiment

We developed a prototype system to verify the performance of the proposed method. Figure 6.7 shows the photograph of the hardware setup. Our system consists of two high-speed cameras (Model: Phantom 340L) with each being attached to a lens (Model: SIGMA 24 mm f/1.8 EX DG), and one mechanical projector whose principle was described in Subsec. 6.2.2. We used an optical chopper system (Model: Thorlabs MC2000) to create structured patterns. The optical chopper system controls the slot speed of the rotating wheel (Model: Thorlabs MC1F100) that has 100 equally spaced slots. We used a halogen lamp and an optical fiber (Model: Thorlabs OSL2RFB) as the light source for the projection system. Additional two lenses (Model: Nikon AF 50mm f/1.8D, and Fuji Fujinon 75mm f/1.8) are placed on the optical path to decide the field of view and the number of periodical fringes. Two cameras were used to capture the projected fringe patterns from slightly different perspectives. A microprocessor (Model: Raspberry pi 2) and the function generator (Model: Tektronix AFG 3022B) were used to generate the external signal to precisely synchronize the cameras with the projector. We printed out a statistical pattern on a transparent film and positioned right behind the rotating wheel to facilitate the correspondence determination by a standard stereo-vision algorithm. We set the camera resolution to be 1024 × 1024 for all static object experiments, and 512 × 512 for dynamically moving object experiments.

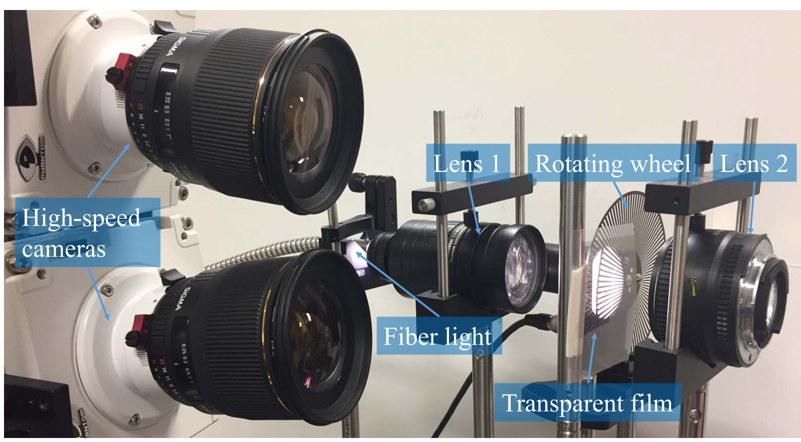

Fig. 6.7. Photograph of experimental hardware system setup.

We first measured a sphere (i.e., a ping-pong ball) to evaluate the measurement accuracy of our proposed method. Figures 6.8 and 6.9 show the experimental results. Figure 6.8(a) shows one of the three phase-shifted fringe patterns captured by the left camera, and Fig. 6.8(b) shows the texture image by averaging three phase-shifted fringe images. The texture image contains a statistical pattern since the light goes through the printed transparent film with a statistical pattern on. The wrapped phase was also obtained from these three phase-shifted fringe images, as shown in Fig. 6.8(c). The same procedures were applied to those fringe patterns captured by the other camera at the same time. Figures 6.8(d)-6.8(f) show the corresponding results.

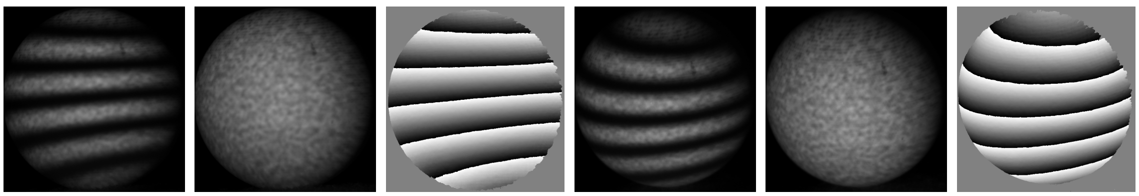

(a) (b) (c) (d) (e) (f)

Fig. 6.8. Measurement results of a ping-pong ball. (a) One of three phase-shifted fringe patterns captured by the left camera; (b) the texture image obtained by averaging three fringe patterns captured by the left camera; (c) wrapped phase map from those images captured by the left camera; (d)-(f) corresponding images for the right camera.

We applied the ELAS algorithm to those two texture images shown in Fig. 6.8(b) and Fig. 6.8(e) to generate a rough disparity map, from which we reconstructed one 3D model as shown in Fig. 6.9(a). This figure shows that even though the sphere surface is smooth, the reconstructed 3D geometry from the rough disparity map rough. We further employed our proposed disparity map refinement computational framework to generate a more accurate disparity map. Figure 6.9(b) shows the 3D result reconstructed from the refined disparity map, showing obvious improvements over the result without employing our proposed computational framework.

We further evaluated the measurement accuracy by comparing our measured result with an ideal sphere. We adopted a least square algorithm to fit the measured data with an ideal sphere having a diameter of 40 mm (the size of ping-pong ball). Figure 6.9(c) shows an image that overlays the ideal fitted sphere with the measured data. We then took the difference between the ideal sphere and the measured data,

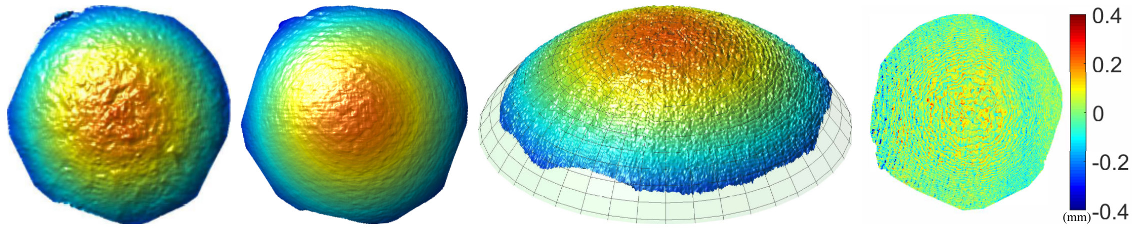

(a) (b) (c) (d)

Fig. 6.9. Measurement results of a ping-pong ball shown in Fig. 6.8. (a) 3D reconstruction using the rough disparity map generated by the ELAS algorithm; (b) 3D reconstruction result from refined disparity map after applying our proposed refinement algorithm; (c) overlays of the ideal fitted sphere and the measured data; (d) difference map between the fitted ideal sphere and the measured data (rms error of approximately 6 μm, and the standard deviation of approximately 78 μm).

and Fig. 6.9(d) shows the result. The mean measurement error is approximately 6 μm, and the standard deviation of the measurement error is approximately 78 μm, demonstrating that our proposed method can indeed achieve high-accuracy measurement.

We also measured a statue with complex surface geometry to further verify the performance of our proposed method. Figure 6.10(a) shows the photograph of the statue we measured, Fig. 6.10(b) shows one of three phase-shifted fringe images, and Fig. 6.10(c) shows the texture image calculated by averaging three phase-shifted fringe images. Similarly, we applied the ELAS algorithm to generate a rough disparity map that was used to reconstruct the rough 3D geometry, shown in Fig. 6.10(d). Figure 6.10(e) shows the 3D result reconstructed from the disparity map obtained by applying the phase constraint to determine the pixel that has the closest phase value. Figure 6.10(f) shows the final result after employing the proposed sub-pixel level refinement procedure. Comparing with the result shown in Fig. 6.10(d), the result obtained from our proposed method, once again, substantially improved measurement quality.

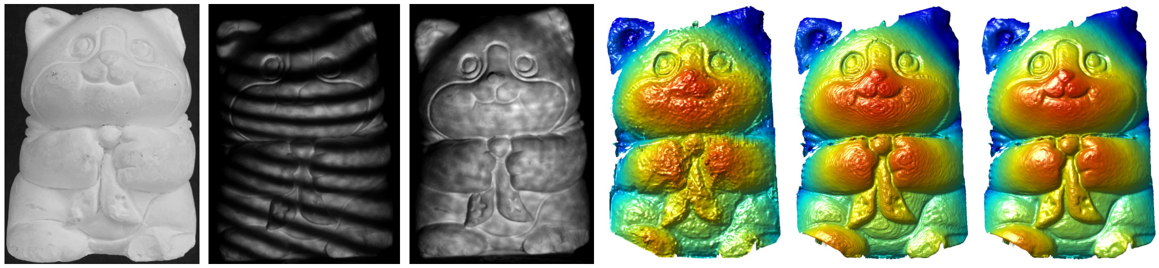

(a) (b) (c) (d) (e) (f)

Fig. 6.10. Measurement results of a statue with complex geometry. (a) Photograph of the sculpture; (b) one of three phase-shifted fringe patterns captured by the left camera; (c) the corresponding texture image; (d) 3D reconstruction using the rough disparity map generated by the ELAS algorithm; (e) 3D reconstruction by applying the phase constraint; (f) 3D reconstruction using our proposed sub-pixel level refinement algorithm.

Figure 6.11 shows the closed-up views of those results shown in Fig. 6.10 to better visualize the differences. This figure clearly shows that the proposed sub-pixel level refinement algorithm indeed gives the best quality 3D data.

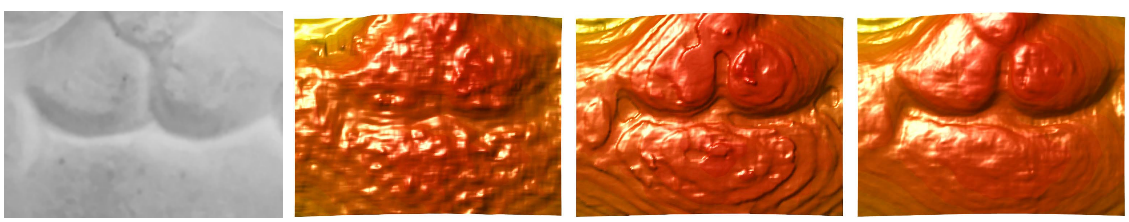

(a) (b) (c) (d)

Fig. 6.11. Closed-up views of the results from Fig. 6.10 around the mouth region. (a) Zoom-in view of Fig. 6.10(a); (b) zoom-in view of Fig. 6.10(d); (c) zoom-in view of Fig. 6.10(e); (d) zoom-in view of Fig. 6.10(f).

Furthermore, we simultaneously measured two isolated objects to demonstrate that our proposed method can actually recover absolute phase for absolute 3D shape measurement. Figure 6.12(a) shows the photograph of these two objects. Figure 6.12(b) and 6.12(c) respectively shows the 3D result reconstructed from the rough disparity map, and that from the refined disparity map after applying our proposed computational framework. This experiment successfully demonstrated that our proposed method can indeed be used to measure absolute 3D geometry of multiple isolated objects.

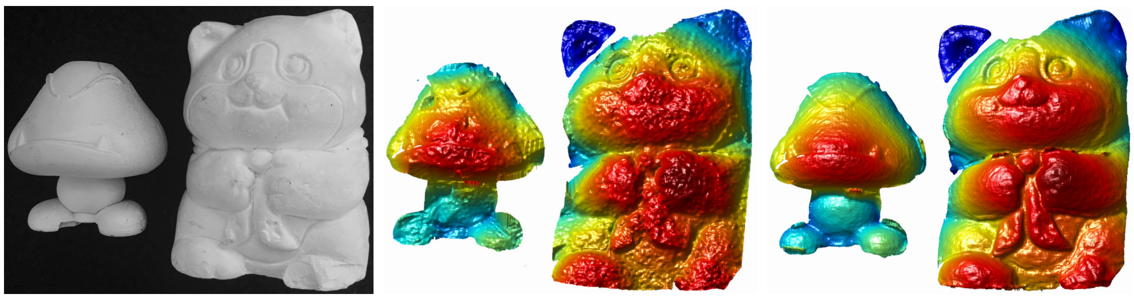

(a) (b) (c)

Fig. 6.12. Measurement results of multiple isolated objects. (a) Photograph of the objects; (b) 3D reconstruction using the rough disparity map; (d) 3D reconstruction using the refined disparity map.

Lastly, we conducted an experiment to demonstrate the capability of high-speed 3D shape measurement. In this experiment, we set the camera resolution as 512×512, the exposure time as 105 μs, the slot speed as 3,000 Hz, and the $N = 3$ step phase-shifting algorithm for phase calculation (e.g., the cameras actually capture images at $3,000 \times 3 = 9,000$ Hz). Figure 6.13 shows a few representative 3D frames, and the associated Visualization 1 includes the entire sequence of recording. This experiments confirmed that our proposed method can be used for high-speed applications. It should be noted that although the slot speed of the projection system can go up to 10,000 Hz for our particular system setup, we chose 3,000 Hz for this experiment because the limited fiber light power.

It is important to note that comparing with the static measurement results shown in Fig. 6.10(f), the high-speed measurement quality is obviously lower. We believe this reduced measurement quality could be introduced by the following factors: (1)

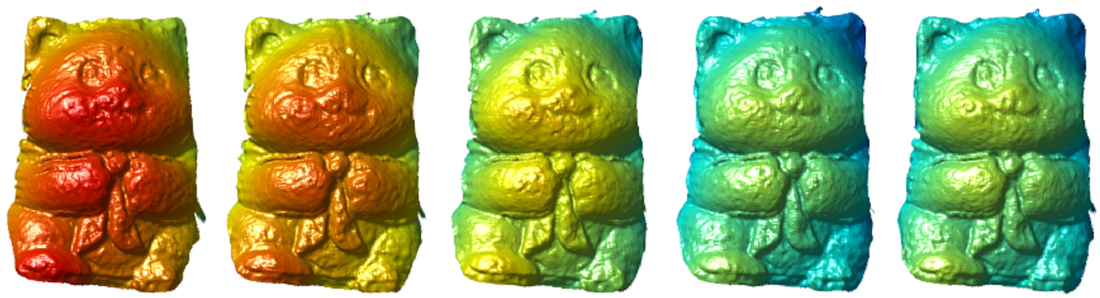

Fig. 6.13. Experimental results of measuring a rapidly moving object. Five representative frames from a sequence of recording shown in the associated with Visualization 1

the lower resolution cameras we used for high-speed measurement, i.e., 1024 $\times$ 1024 camera resolution was used for static measurements whilst 512 $\times$ 512 was used for high-speed measurements; (2) the camera noise is larger for high-speed measurements due to the reduced exposure time; (3) the fringe quality generated by the spinning wheel was low because the fringe stripes are very wide and are nonsinusoidal even after defocusing, as shown in Fig. 6.8(a), 6.8(d) and 6.10(b); (4) the phase quality produced from the left camera could be different from that produced by the right camera because of their different perspectives; and (5) the phase-based interpolation may not be precise due to the circular nature of the fringe patterns.

6.4 Discussion

The proposed high-speed and high-accuracy 3D shape measurement technique has the following major advantageous features:

- *High measurement speed.* The proposed technique can always achieve the same 3D measurement speed as the speed of the projector (10,000 Hz in our case) regardless the number of phase-shifted fringe images required for one 3D reconstruction as long as the camera speed is high enough. In contrast, if the projector's refresh rate is fixed, the measurement speed of a conventional DFP system decreases when the number of phase-shifted fringe images used for one 3D reconstruction increases .

- *High measurement accuracy.* The proposed method can also achieve high measurement accuracy because (1) phase-shifted fringe patterns are precisely captured through precise synchronization between the cameras can the projector; (2) a statistical pattern is used to enhance the robustness of the initial rough disparity map calculation; and (3) a novel rough disparity map refinement computational framework is developed to achieve sub-pixel level disparity map determination accuracy.

- *Broad light spectrum.* Since the mechanical projection device uses a metal plate with ON and OFF slots, a broad spectrum of light can be used to generate desired fringe patterns for 3D shape measurement. In contrast, the conventional DFP systems use a silicon-based projectors (e.g., LCD, or DLP), and the spectrum of light is greatly restricted to the region that silicon can properly function.

However, the proposed method is not trouble free. Unlike the state-of-the-art DLP based high-speed 3D shape measurement techniques, this proposed method requires two high-speed cameras to realize absolute 3D shape measurement mainly because it is more difficult to precisely calibrate the mechanical projection device than the DLP projector, and is also more difficult to generate different frequency fringe patterns for absolute phase recovery.

6.5 Summary

This chapter has presented a method for high-speed and high-accuracy 3D shape measurement using a mechanical fringe projection system. In lieu of using a silicon-based projection device such as a DLP or LCD projector, the proposed fringe projection system uses the metal-based pattern generation mechanism that allows the use of a much broader light spectrum of light for 3D shape measurement. The proposed technique achieved both high-speed and high-accuracy 3D shape measurement through precisely synchronizing the cameras with projector, and developing a novel computational framework for sub-pixel disparity map generation. We developed a prototype hardware system that can accurately measure both single and multiple isolated objects. The same hardware prototype system could potentially achieve 10,000 Hz 3D shape measurement speeds regardless the number of phase-shifted fringe patterns required for one 3D reconstruction.

7. INFLUENCE OF PROJECTOR PIXEL SHAPE ON ULTRAHIGH-RESOLUTION 3D SHAPE MEASUREMENT

7.1 Introduction

With recent advancements of the 3D shape measurement field and the increasingly availability of affordable commercial 3D sensors, 3D shape measurement techniques have been rapidly impacting in fields ranging from biomedical engineering, manufacturing, robotics, and entertainment [106].

Among existing 3D shape measurement techniques, DFP has been especially popular because of its achievable high measurement accuracy, and high spatial resolution [4]. A typical DFP system consists of one projector that projects fringe patterns onto the object and one camera that receives the fringe patterns scattered by the object surface. Instead of using intensity, a DFP system uses the carrier phase of fringe image(s) for 3D shape recovery. To achieve high quality measurement, high quality phase has to be recovered. As such, DFP techniques can achieve camera pixel level spatial resolution with the fundamental assumption that high-quality sinusoidal fringe patterns can be captured.

There are basically two ways to create sinusoidal fringe patterns [107]: defocus 1-bit binary images and directly use 8-bit sinusoidal images. The latter is straightforward in terms of concept and implementation, but has three major limitations: (1) nonlinear gamma influence of the projector; (2) requirement of a large number of pixels to represent a accurate sinusoidal profile; (3) precise synchronization requirement between the projector and the camera. Typically, narrower fringe patterns could produce higher SNR phase and thus better measurement quality. Therefore, it is desirable to use narrow fringe patterns for 3D shape measurement system. However, using multiple level grayscale images to produce sinusoidal patterns may not be preferable due to the Limitation #2. The binary defocusing technique, in contrast, can use smaller number of pixels to produce sinusoidal patterns through defocusing, and thus has been extensively studied for high-quality 3D shape measurement.

Since achieving higher speed and higher measurement resolution is increasingly needed whilst simultaneously maintaining a large field of view (FOV). It is more practical to use a smaller camera pixel size in object space because realizing higher projector resolution is more costly. In a typical DFP system, the projector pixel size and the camera pixel size are comparable in the object space, the shape of projector pixel is typically not considered. However, to achieve ultrahigh resolution, the camera pixel size is much smaller than the projector pixel size (e.g., the camera pixel size is 1/10 of the projector pixel size), the shape of the projector pixel might no longer be negligible.

There are two types of DMDs developed for DLP projectors: rectangular shaped pixels and diamond-shaped pixels. Our research found that, when the camera pixel size is much smaller than the projector pixel size in order to achieve ultrahigh resolution 3D shape measurement, the diamond-shaped DMD pixels cannot be used to achieve high-quality 3D shape measurement. We believe that this is caused by the sampling effect of mismatched pixel shape from the computer generated pixel to the projected pixel. This chapter evaluates the performance of the DFP system for ultrahigh resolution 3D shape measurement using two different types of projectors. Both simulations and experiments demonstrated that a projector with rectangular shaped pixels is more suitable for ultrahigh resolution (e.g., camera pixel is 1/5 of the projector pixel) 3D shape measurement.

Section 2 explains the basic principle of phase-shifting algorithms. Section 3 shows simulation results. Section 4 presents experimental results. Section 5 summarizes this chapter.

7.2 Phase-shifting algorithm

Because of high-speed, high-accuracy, and robustness to noise, phase-shifting algorithms have been extensively adopted for 3D optical metrology [60]. For an N-step phase-shifting algorithm with equal phase shifts, the $k-th$ fringe pattern can be mathematically described as,

$$I_k(x,y) \;=\; I'(x,y) + I''(x,y)\cos[\phi + 2k\pi/N], \tag{7.1}$$

where $I'(x,y)$ is the average intensity, $I''(x,y)$ is the intensity modulation, $phi(x,y)$ is the phase to be solved for, and $k = 1, 2, \ldots, N$. The phase can be calculated as,

$$\phi(x,y) = -\tan^{-1}\frac{\sum_{k=1}^{N} I_k(x,y)\sin(2k\pi/N)}{\sum_{k=1}^{N} I_k(x,y)\cos(2k\pi/N)}. \tag{7.2}$$

Due to the use of an arctangent function, the phase value obtained by Eq. 7.2 ranges from $-\pi$ to π with 2π discontinuities, which is often regarded as *wrapped phase*. To recover a continuous phase map, a phase unwrapping algorithm is required. The phase unwrapping algorithm adds or subtracts integer multiples of 2π to remove 2π discontinuities for each pixel. There are two different categories of phase unwrapping algorithms: spatial phase unwrapping [108,109] and temporal phase unwrapping [4]. The former can only provide the relative phase information because the algorithm is typically based on a reference point in the phase map. In contrast, a conventional temporal phase unwrapping method requires more patterns to determine the proper number of 2π for each pixel to unwrap the wrapped phase, whilst some recent geometric constraint based algorithms can also unwrap the phase without temporally acquiring more images [46,80,84–86,88–90]. In this research, we used the gray-coding method, which is one of the temporal phase unwrapping algorithms, to obtain the unwrapped phase map [40]. Once the unwrapped phase is obtained, 3D information can be recovered if the system is calibrated [110].

7.3 Simulation

For a 3D shape measurement system employing the binary defocusing method, a DLP projector is preferable due to its achievable high contrast and high speed [4]. DLP projectors has two types of pixels: the diamond-shaped pixels and the rectangular shaped pixels, as shown in Fig. 7.1(b) and 7.1(a). The rotation axis of the rectangular pixel is the middle line of the rectangular pixels and the rotation axis of the diamond-shaped pixel is along the diagonal line. The definition of a projected image is clear for a projector with rectangular shaped pixels because the one-to-one mapping is precisely along each row and each column, as shown in Fig. 7.1(c). However, the definition of a projected image for a projector with diamond-shaded pixels is not a precisely one-to-one mapping, as shown in Fig. 7.1(d). The different mapping process could introduce differences during the resampling process when the projected image is captured by the camera, especially when the camera pixel size is much higher than the projector pixel size in object space. Therefore, this research endeavors to study such an influence on ultrahigh resolution 3D shape measurement.

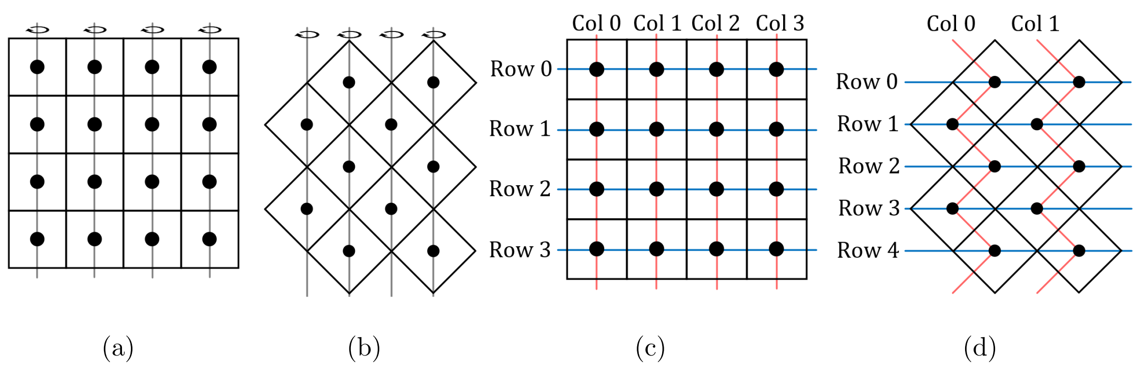

Fig. 7.1. Illustration of two different types of DLP projectors. (a) Rectangular shaped pixels and the rotation axis; (b) diamond-shaded pixels and the rotation axis; (c) row and column definition of rectangular-shaped pixels; (d) row and column definition of diamond-shaped pixels.

We first analyzed the phase quality by comparing the phase error between two different pixel shapes with respect to projector-to-camera pixel size ratios. We employed the binary defocusing technique with a fringe pitch as 12 and a phase shift number of 12 (i.e., $N = 12$). Figure 7.2(a) shows one of computer generated phase-shifted binary patterns for a projector with rectangular-shaped pixels. Figure 7.2(b) shows one of computer generated phase-shifted binary patterns for a projector with diamond-shaped pixels. It is obvious that the diamond-shaped pixels produce a pattern with saw-tooth edging artifacts, whilst the pattern produced by rectangular-shaped pixels does not have such artifacts.

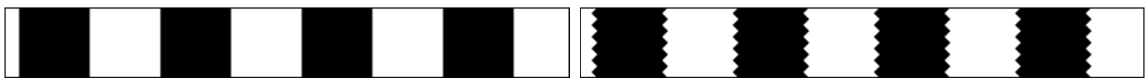

(a) (b)

Fig. 7.2. Ideal binary patterns with different projector pixel shapes. (a) One of the binary patterns for a projector with rectangular-shaded pixels; (b) one of the binary patterns for a projector with diamond-shaded pixels.

These phase-shifted patterns were blurred by applying a Gaussian filter with a size of 5×5 pixels then resampled with a much smaller camera pixel size (i.e. one projector pixel corresponds to many resampled camera pixel). Figure 7.3(a) shows the resampled image of the blurred pattern shown in Fig. 7.2(a) when the projector pixel size is 16 times of the camera pixel size. The resampled phase-shifted patterns are then used to compute the wrapped phase, as shown in Fig. 7.3(c). The wrapped phase is further unwrapped and compared against the ideal phase to determine the error. Figure 7.4(b) shows the error map when the projector-camera pixel size ratio is 16:1. We then calculated the rms value of the error map, 0.123 rad for this case, to quantify the phase quality.

We employed a similar process to analyze the phase error for the projected image with a rectangular shaded pixels. Figures 7.3(b) shows the resampled blurred pattern shown in Fig. 7.2(b) when the projector pixel size is 16 times of the camera pixel size. Figure 7.3(d) shows the wrapped phase map, and Fig. 7.4(a) shows the error map with a rms error of 0.167 rad when the projector-camera pixel size ratio is 16:1.

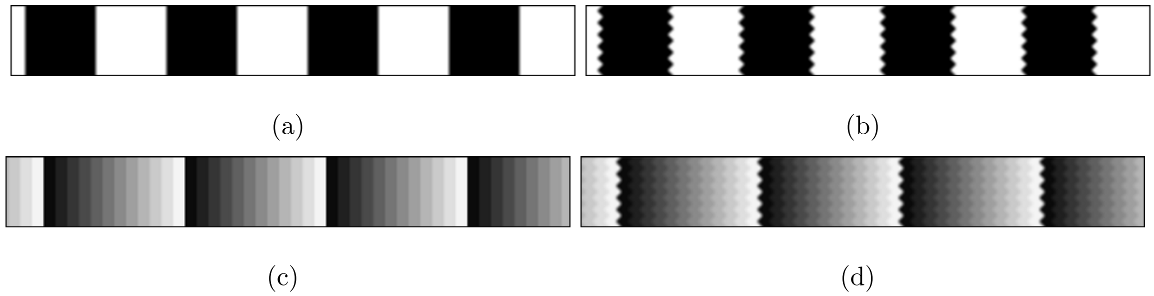

Fig. 7.3. Simulations for ultrahigh resolution captured system. (a) One of the captured fringe images for the projector with rectangular-shaped pixels; (b) one of the captured fringe images for the projector with diamond-shaped pixels; (c) wrapped phase map for the captured fringe images for the projector with rectangular-shaped pixels; (d) wrapped phase map for the captured fringe images for the projector with diamond-shaped pixels.

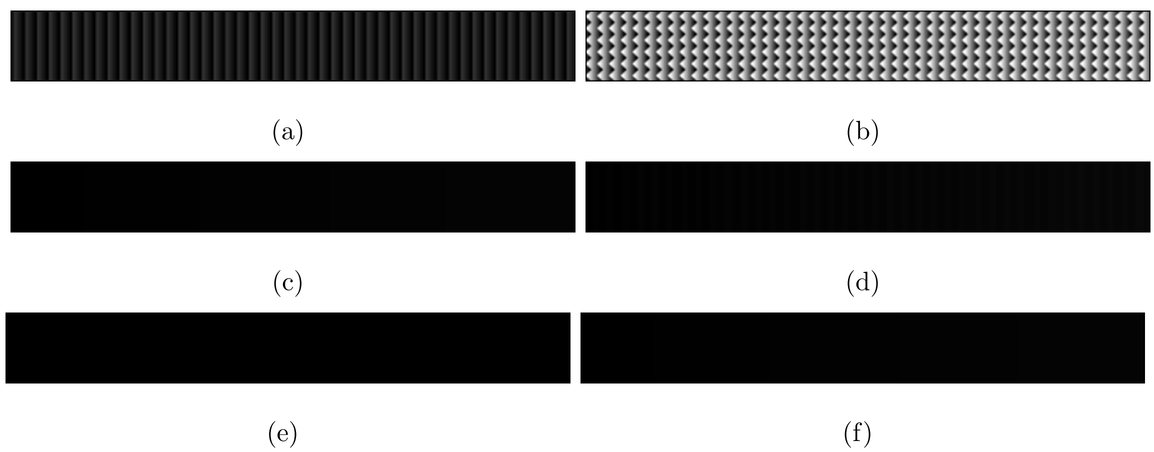

Fig. 7.4. Representative phase error maps with different projector-to-camera pixel size ratios. For all images, purely black represents absolute phase error of 0 rad, and purely white represents absolute phase error of 0.57 rad. (a) Phase error map for the captured fringe images for the projector with rectangular-shaped pixels (rms 0.12 rad) when projector-camera pixel size ratio is 16:1; (b) phase error map for the captured fringe images for the projector with diamond-shaped pixels (rms 0.17 rad) when projector-camera pixel size ratio is 16:1; (c)-(d) phase error maps results when the projector-camera pixel size ratio is 2:1; (e)-(f) phase error maps results when the projector-camera pixel size ratio is 1:1.

Clearly, the phase rms error is much larger than that obtained using the projector with rectangular-shaped pixels.

We then analyzed the phase error for different camera pixel sizes. We basically combined $m \times m$ pixels of the resampled patterns with the projector pixel size being 16 times of the camera pixel size and recomputed the phase rms error. Figure 7.4 shows some representative error maps with different projector-to-camera pixel size ratios, and Fig. 7.5 summarizes the comparing phase rms errors for both types of projectors. Clearly, when the projector pixel size is similar to that of the camera pixel size, these two types of projectors do not have significant difference, as expected. However, when the projector pixel size is much larger than the camera pixel size (e.g., 5 times), the phase rms error for the projector with rectangular shaded pixels is much smaller than that for the projector with diamond-shaded pixels. Furthermore, one may notice that the difference quickly increase when the projector to camera pixel size ratio is between 2 and 5, and then the separation remain quite large when the ratio is larger than 5 or so.

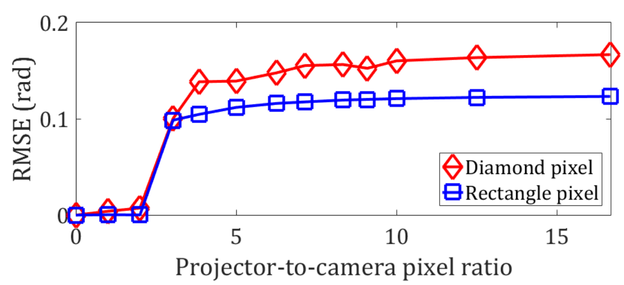

Fig. 7.5. Simulation results of two projector types with different projector-to-camera pixel ratio with binary patterns.

In addition, we ran simulation on ideal sinusoidal fringe patterns instead of blurred binary patterns. Figure 7.6(a) shows one of sinusoidal fringe patterns for the projector with diamond-shaped pixels. Figure 7.6(b) shows one of sinusoidal fringe patterns for the projector with rectangular shaped pixels. We followed the same process to analyze the phase error, and the corresponding phase error maps are shown in Fig. 7.6(c) and Fig. 7.6(d) respectively.

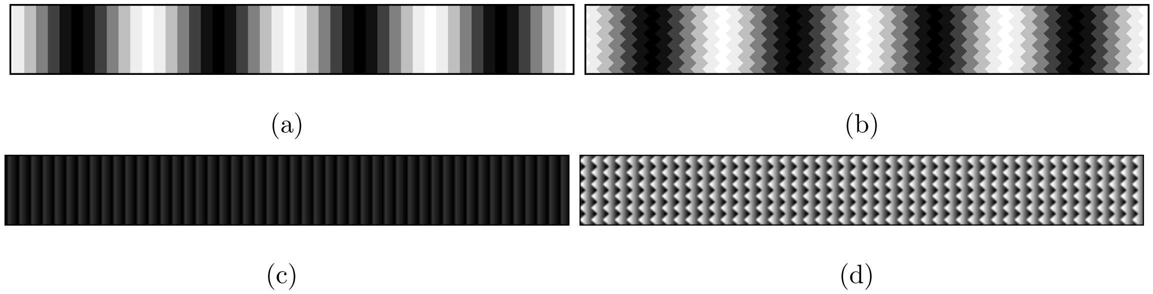

Fig. 7.6. Comparing simulation results when the projected fringe patterns are sinusoidal. (a) One of the captured fringe images for the projector with rectangular-shaped pixels; (b) one of the captured fringe images for the projector with diamond-shaped pixels; (c) phase error map for the captured fringe images for the projector with rectangular-shaped pixels; (d) phase error map for the captured fringe images for the projector with diamond-shaped pixels.

Figure 7.7 shows the comparing result when the projector pixel size varies from 1 to 16 times of the camera pixel size. Once again, the projector with diamond shaped pixels produce significantly larger error than that of the projector with rectangular shaped pixels when the projector pixel size is much larger than the camera pixel size.

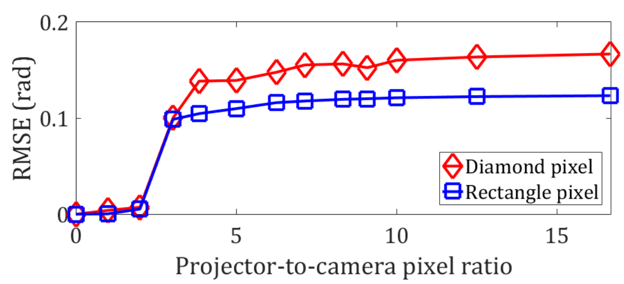

Fig. 7.7. Simulation results of two projector types with different projector-to-camera pixel size ratios when projected patterns are sinusoidal patterns.

7.4 Experiment

We developed two DFP systems to experimentally evaluate these two type of projectors. Figure 7.8 shows photographs of the systems: the first system (*System I*) used a DLP projector with rectangular-shaped pixels (model: Texas Instrument LightCrafter 6500), and the second system (*System II*) used a DLP projector with diamond-shaded pixels (model: Texas Instrument LightCrafter 4500). The projector in the first system has a resolution of 912 $\times$ 1140 and the projector in the second system has a resolution of 1920 $\times$ 1080. Both systems include the same model camera (model: FLIR Grasshopper USB 3.0). The camera was attached with a 25 mm lens (model: Kowa LM25HC-V) whose resolution was set as that has a pixel size of 3.45 $\mu m \times 3.45$ μm, and the camera resolution was set as 2048 $\times$ 1536. The camera pixel size is 3.45 $\mu m \times 3.45$ μm, the LightCrafter 4500 projector pixel size is 7.64 $\mu m \times 7.64$ μm, and LightCrafter 6500 projector pixel size is 5.5 $\mu m \times 5.5$ μm. Both systems used the microprocessor (model: Arduino Uno) to synchronize the camera with the projector. For all experiments, the projector used only green channel and the projection and capturing speed was set as 20 Hz.

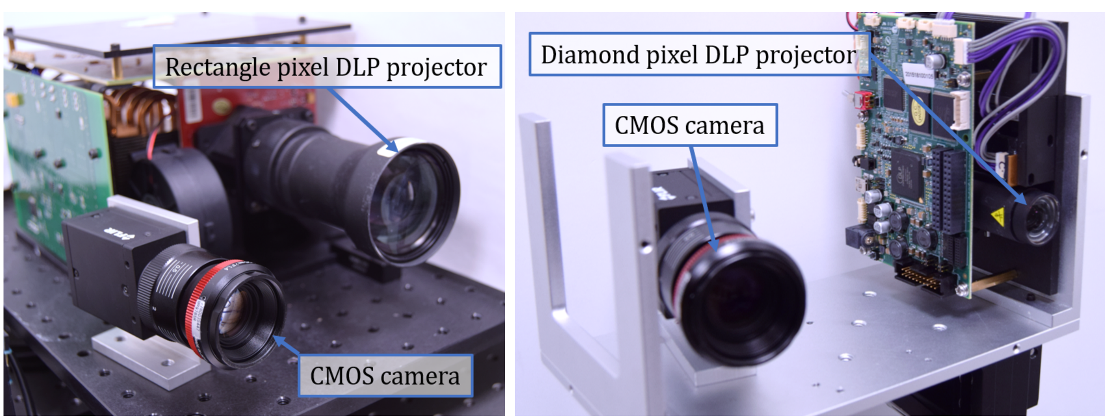

(a) (b)

Fig. 7.8. Photographs of experimental system setups. (a) *System I*: system using a projector with diamond-shaped pixels; (b) *System II*: system using a projector with rectangular-shaped pixels.

We carried out experiments to evaluate performance of these two systems with varying projector-to-camera pixel ratios. We first measured a flat white plane using 12 phase-shifted fringe patterns with a fringe period of 12 pixels. The projector was slightly defocused to reduce the impact of high order harmonics. The projector was positioned further away such that each projector pixel is equivalent to approximately 16 camera pixels on the plane. For these experiments, the camera was attached with 25 mm lenses (model: Kowa LM25HC-V). We captured the phase-shifted fringe patterns and gray coded patterns for absolute phase retrieval. Figure 7.9(b) shows one of phase-shifted fringe patterns projected by the projector with diamond-shaped pixels, and Fig. 7.9(d) shows zoom-in view that clearly depicts the diamond pixel shape. Figure 7.9(a) shows one of the phase-shifted fringe patterns projected by the projector with rectangular shaped pixels images, and Fig. 7.9(c) shows zoom-in view that shows the rectangular pixels.

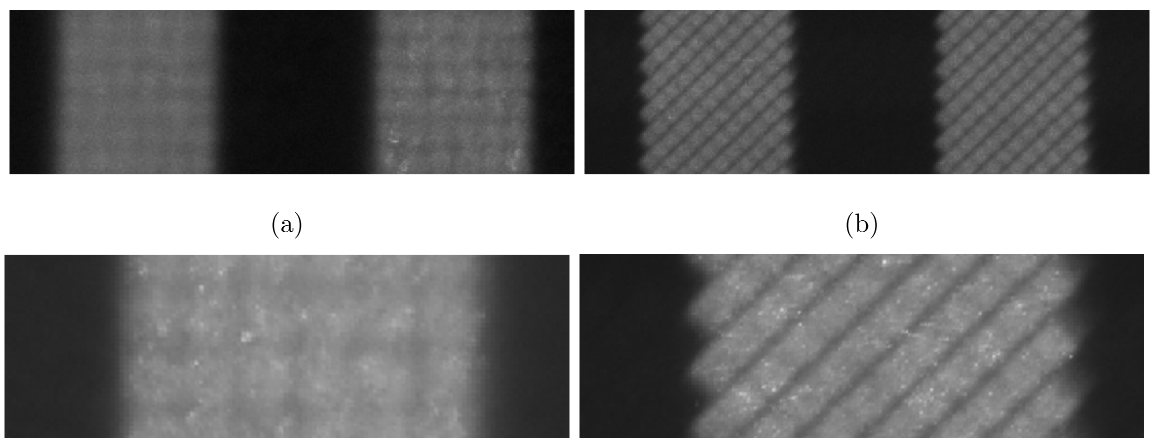

(a) (b) (c) (d)

Fig. 7.9. Representative captured images. (a) One of the captured fringe images from *System I*; (b) one of the captured fringe images from *System II*; (c) zoom-in view of the pattern shown in (a); (d) zoom-in view of the pattern shown in (b).

We obtained absolute phase map from these captured fringe patterns and then calculated the phase error map by subtracting the reference plane. The reference plane was created by applying a Gaussian filter with a size of 21 $\times$ 21 pixels to the unwrapped phase map. Figure 7.10(b) shows the error map of *System I* when the projector pixel size is 16 times of the camera pixel size. Figure 7.10(a) shows the error map of *System II* when the projector pixel size is 16 times of the camera pixel size. Once again, we combine $m \times m$ pixels of the camera captured images to artificially create smaller projector-to-camera pixel size ratios. Figure 7.10 shows some representative phase error maps.

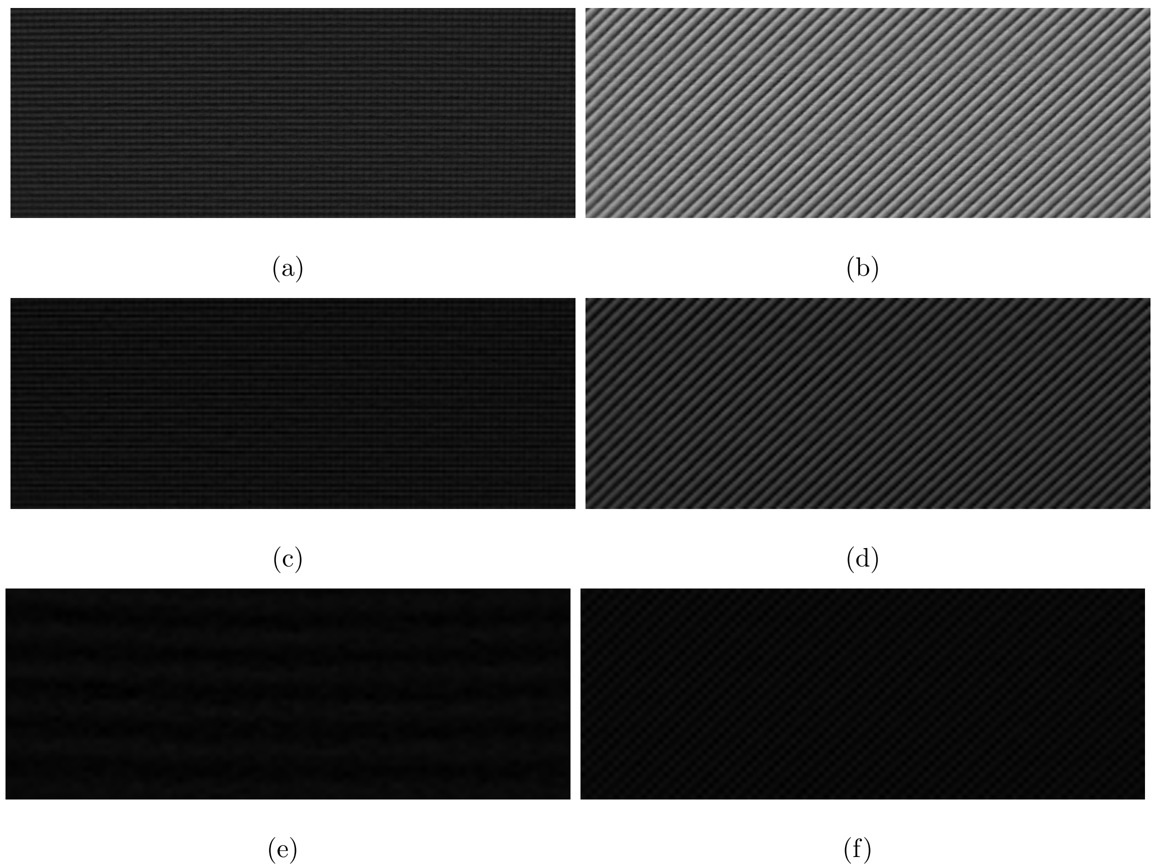

Fig. 7.10. Phase error analysis for the flat plane experiments. (a) Phase error map of *System I* when projector-camera pixel ratio is 16:1; (b) Phase error map of *System II* when projector-camera pixel ratio is 16:1; (c)-(d) phase error maps results when the projector-camera pixel size ratio is 2:1; (e)-(f) phase error maps results when the projector-camera pixel size ratio is 1:1.

Figure 7.11 shows phase rms error for both systems with respect to the projector-to-camera pixel ratio. This once again demonstrated that the DFP system using a projector with diamond-shaped pixels has lower quality phase than the system using projector with a rectangular shaped projector when the projector pixel size is much larger than the camera pixel size. Furthermore, when the projector to camera pixel size ratio ranges from 1 to 3, the error difference rapidly increases, and remain relatively large when the ratio is larger than 5.

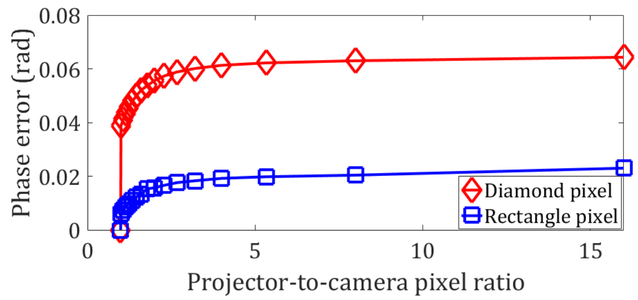

Fig. 7.11. Experimental result of two projector types with respect to different projector-to-camera pixel size ratios.

We then measured a sphere with a diameter of 40 mm using both systems. For these experiments, the camera was attached with 25 mm lenses (model: Kowa LM25HC-V). We configured both systems to ensure that the the projector pixel size is approximately 8 times of the camera pixel size. Figure 7.12(a) shows the photograph of the sphere captured by *System I*. Figure 7.12(b) shows one of the captured fringe patterns. We then employed the phase-shifting algorithm to obtain absolute phase map, and the absolute phase map is further converted 3D geometry by using the reference plane based method [111]. Figure 7.12(c) shows the final 3D reconstruction. To better visually compare the measurement results, we generated a close-up view of the 3D reconstruction, as shown in Fig 7.12(d). Figure 7.12(e)-7.12(h) respectively shows the photograph of the object captured by *System II*, one of the fringe patterns, and the corresponding 3D reconstruction, and the close-up view of 3D reconstruction.

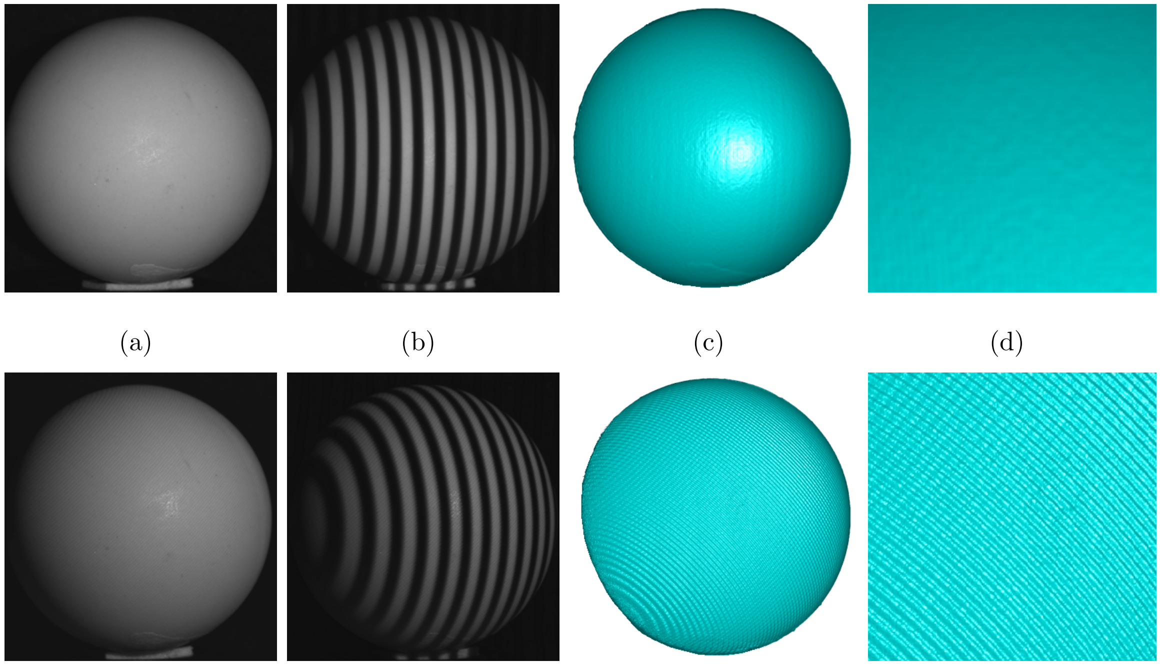

(a) (b) (c) (d)

(e) (f) (g) (h)

Fig. 7.12. Experimental result of a sphere. (a) Photograph captured by the first system; (b) one of the fringe images captured by *System I*; (c) 3D result by *System I*; (d) zoom-in view of (c); (e) photograph captured by *System II*; (f) one of the fringe images captured by *System II*; (g) 3D result by *System II*; (h) zoom-in view of (g).

We measured a statue with more complex 3D surface geometry when the projector pixel size is approximately 16 times of the camera pixel size. Figure 7.13 shows the measurement results. Figure 7.13(a) shows photograph statue captured by *System I*. Figure 7.13(b) shows 3D reconstruction, and Fig. 7.13(c) shows the corresponding close-up view. Similarly, we measured the same statue with *System II*, and the corresponding results are shown in Fig. 7.13(d) and Fig. 7.13(e).

Lastly, we reconfigured the system with different projector-to-camera pixel size ratios (approximately 2:1 and 1:1), and measured two complex 3D objects. For the 1:1 ratio systems, the camera was attached with a 8 mm lens (Model: Computar M0814-MP2), and for the 2:1 ratio systems, the camera was attached with a 16 mm lens (Model: Computar M1614-MP2). Figure 7.14 shows the corresponding

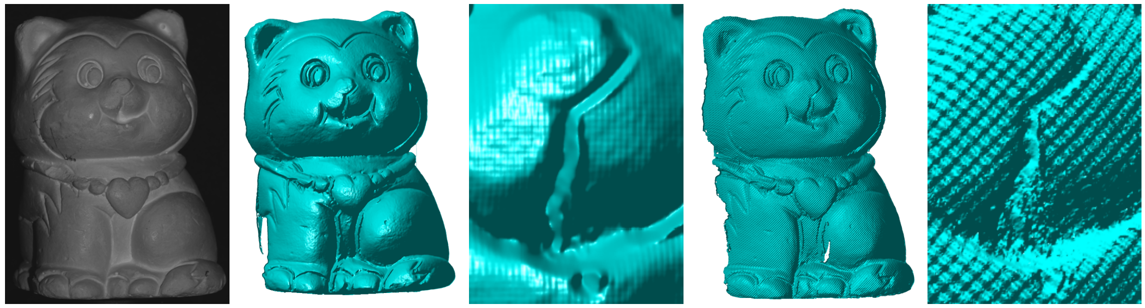

(a) (b) (c) (d) (e)

Fig. 7.13. Experimental results of a statue. (a) Photograph captured by *System I*; (b) one of the fringe images captured by *System I*; (c) 3D result with *System I*; (d) zoom-in view of (c); (e) photograph captured by *System II*; (f) one of the fringe images captured by *System II*; (g) 3D result with *System II*; (h) zoom-in view of (g).

results. The comparing data shows that when the projector-to-camera pixel ratio is approximately 2:1, the result obtained from *System I* is better than that obtained from *System II*; whilst the data quality is similar when the projector-to-camera pixel size ratio is approximately 1:1. All the simulation and experimental results confirmed that (1) when the camera pixel is much smaller than the projector pixel in object space, 3D shape measurement quality obtained from a system using a projector with rectangular shaped pixels is much higher than that obtained from a system using a projector with diamond-shaped pixels; (2) the projector-camera pixel size ratio has less influence on measurement quality for a DFP system using a projector with rectangular shaped pixels than using a projector with diamond shaped pixels; and (3) overall, the DFP system using a projector with rectangular pixels produces much smoother 3D geometry with higher measurement accuracy.

7.5 Summary

This chapter evaluated the performance of DLP projectors with two different shaped pixels for ultrahigh-resolution 3D shape measurements. Our simulation and

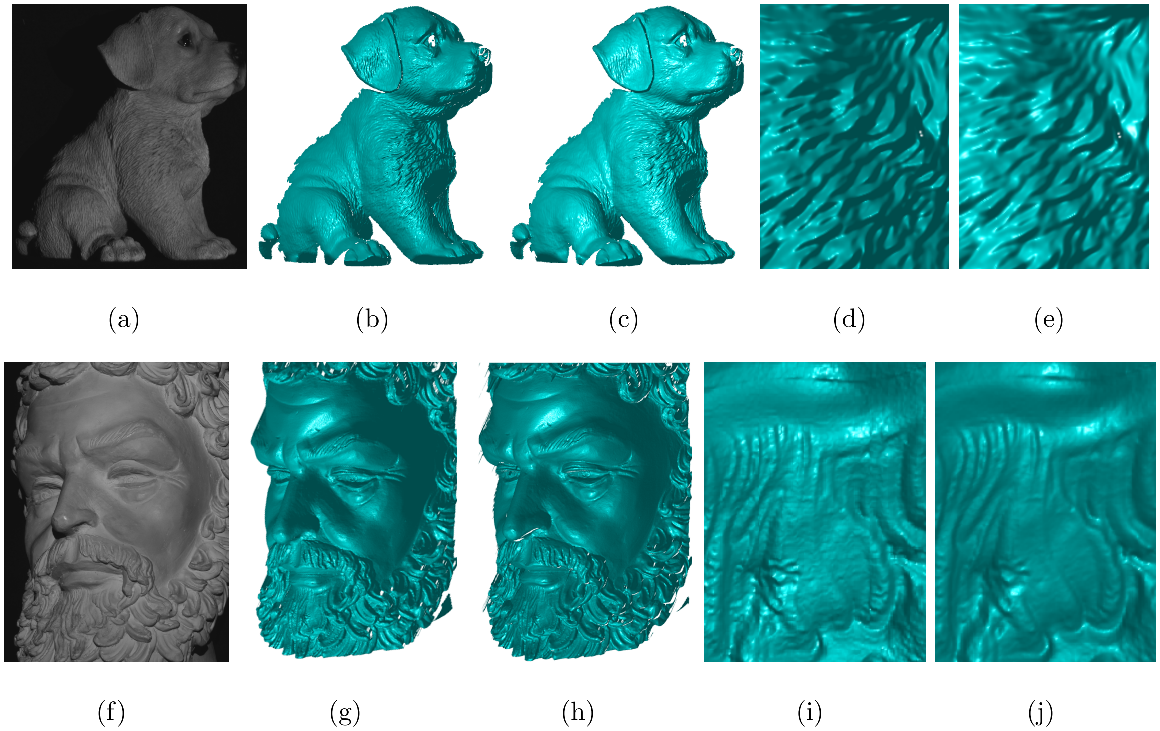

Fig. 7.14. Experimental results of complex 3D objects with different projector-to-camera pixel size ratios. (a) Photo of the object measured with projector-to-camera pixel size ratio of 2:1; (b) 3D result with *System I*; (c) 3D result with *System II*; (d) close-up view of (b); (e) close-up view of (c); (f) Photo of the object measured with projector-to-camera pixel size ratio of 1:1; (g) 3D result with *System I*; (h) 3D result with *System II*; (i) close-up view of (g); (j) close-up view of (h).

experimental results demonstrated that if the camera pixel size is similar to the projector pixel size, the pixel shape has negligible influence on measurement quality. However, if a single projector pixel corresponds to a lot more camera pixel, the diamond shaped projector pixels introduce measurement artifacts that reduces measurement quality. Therefore, in general, it appears when employed in a DFP system, the projector with rectangular pixels outperforms that with diamond-shaped pixels .

8. SUMMARY AND FUTURE DIRECTIONS

8.1 Summary of Contributions

In unstructured environments, it is difficult for robots to acquire accurate 3D data based on electromagnetic tools because they are exposed to many disturbances. To overcome the environmental limitations, this research has made the following contributions:

- **Developed a novel method to enhance the robustness of conventional the two-frequency phase-shifting method by using geometric constraints.**

  A multi-frequency phase-shifting method is one widely used method for temporal phase unwrapping. Two-frequency phase-shifting is commonly used for high-speed 3D sensing, but it is sensitive to noise. On the other hand, three- or more-frequency phase-shifting algorithms are preferred for accurate 3D results. The limitation of the conventional two-frequency method is that the fringe order for absolute phase is calculated after multiplying a scaling factor to the phase. Therefore, to cover the whole projection range and obtain high-accuracy results, a large scaling factor is used. However, because this scaling factor also affects the noise with the same ratio as the valid data, using the two-frequency method for high-accuracy has been undesirable. This research proposed a method that utilizes the geometric constraints of the DFP system and unwraps the phase within a certain phase range to reduce the noise substantially without additional patterns. If we set an artificial depth range where the object can be placed, the absolute phase on the object does not exceed the phase range based on the artificial depth range. Then, the fringe order of the phase can be determined by the difference between the retrieved phase and the artificial phase map. This research has been published in *Applied Optics* and was discussed in Chapter 3.

- **Developed a novel method to retrieve 3D absolute phase by reducing the number of patterns for one 3D image.**

  The proposed research suggests reducing the number of patterns to do high-speed 3D sensing. The number of patterns is an important factor to determine the speed of 3D reconstruction because the patterns are captured sequentially by a camera, which means that the number of patterns is proportional to the time taken to capture a set of images for one 3D image. By integrating texture image of the object with a phase coding method, a total of five binary patterns including three fringe patterns are used to get an absolute phase map for 3D reconstruction. Specifically, three dense binary dithered patterns are used to compute the wrapped phase, and the average intensity is combined with two additional binary patterns to determine fringe order pixel by pixel in phase domain. In addition, geometric constraints are used to reduce the noise in the patterns. By doing experiments with a high-speed camera, the sensing system captured 3,333 images per second and about 666 three-dimensional data of the object achieved in a second. This research has been published in *Optics and Lasers in Engineering* and was introduced in Chapter 4.

  Other research presents a method that reconstructs absolute 3D shape using three binary patterns: one DC, one low-frequency, and one high-frequency fringe pattern. The procedures are to (1) take the difference between the sinusoidal fringe patterns and the DC pattern, (2) apply Hilbert transform to the difference images to generate two phase maps, (3) employ the geometric constraint-based phase unwrapping method to unwrap the low-frequency phase map, (4) unwrap the high-frequency phase map using the unwrapped low-frequency phase map, and (5) reconstruct 3D shape. We developed a prototype system that can capture 2D images at 6,000 Hz, achieving 2,000 Hz 3D shape measurement speed.

This research has been published in *Optical Engineering* and was introduced in Chapter 5.

- **Developed a custom-designed mechanical projector for high-speed and high-accuracy 3D surface measurement and broad-light spectrum.**

  A DLP projector, which is widely used in fringe analysis, has DMD to project a pattern(s) pixel by pixel. Micro mirrors inside the DLP projector are made of silicon-based material, which reflects only a specific range of light spectrum. Therefore, only a limited-light spectrum can be used for 3D sensing. Besides, a DLP projector has a speed limitation for projecting gray-scale patterns needed for fringe analysis. Although standard stereo vision can reconstruct 3D images using a single image from each camera [99], the resolution and accuracy is much lower than with DFP techniques. This research proposed a new custom-designed projector, which projects fringe patterns using a rotating wheel with equally spaced ON/OFF structures in lieu of silicon-based projectors, such as a DLP or LCD projector. By making the light source for projection independent of the projector mechanism, users can easily replace it with another one, which has a specific light spectrum. To acquire high-speed 3D sensing, two high-speed cameras and one mechanical projector need to be synchronized precisely. We used a high-performance microprocessor to synchronize the optical devices in microseconds. As a result, the system can capture 3D images at a speed up to 10,000 Hz. With the proposed refinement algorithm, we can achieve sub-pixel level accuracy of 3D images. This research has been published in *Optics Express* and was introduced in Chapter 6.

- **Developed a custom-designed mechanical projector for high-speed and high-accuracy 3D surface measurement and broad-light spectrum.**

The state-of-art 3D shape measurement with digital DFP techniques assume that the influence of projector pixel shape is negligible. However, this research reveals that, when the camera pixel size is much smaller than the projector pixel size in object space (e.g., 1/5), the shape of projector pixel can play a critical role in ultimate measurement quality. This research evaluated the performance of two shapes of projector pixels: rectangular and diamond shaped. Both simulation and experimental results demonstrated that, when the camera pixel size is significantly smaller than the projector pixel size, it is more advantageous for an ultrahigh resolution 3D shape measurement system to use a projector with rectangular shaped pixels than the projector with diamond-shaped pixels. This research was introduced in Chapter 7.

These researches were funded by the National Science Foundation (NSF) under Grant No. CMMII-1531048, IIS-1637961 and National Institute of Justice (NIJ) under Grant No. 2016-DN-BX-0189.

8.2 Future directions

8.2.1 Phase-based feature detection for global mapping

To generate a 3D model of a large object with the 3D sensor, each 3D frame should be stitched to other 3D frames captured at different times. With the release of a low-cost 3D scanner, people can obtain the 3D model of an object, as well as the texture image. Even if researchers easily obtain the 3D geometries sequentially, the stitching algorithms are mainly based on the texture image by calculating the correlation between sequentially captured images. As stated above, processing the data in intensity domain of texture image could be unstable , depending on lighting conditions or surface reflectivity. In addition, if there are not enough feature points on the surface of the object, such as a room surrounded by white walls, it is more difficult to calculate the correlation to stitch the 3D models. Instead of using texture variation for feature points, we can utilize the phase information as feature points for stitching separate 3D images and get an accurate 3D global map. As mentioned before, because phase information is more robust to noise and has high-spatial resolution, we can obtain a number of feature points to reconstruct one large 3D model.

8.2.2 Customized 3D scanning system for maintenance of infrastructures

The customized mechanical projector introduced in Chapter 6 suggested a new projector utilizing the phase information directly without a back-and-forth computational framework. It broadens the light spectrum for projection and achieves super-fast projection speed, which the DLP projector finds difficult to achieve. Even if the configuration of optical devices is very simple, the size of the sensing system is not optimized for a mobile platform or a robotic arm. In addition, because the projector is designed with a rotating wheel for fringe patterns and only a small part of the wheel is used for projection, the field of view is too small to measure the surrounding environments and map the 3D data. Still, a mechanical projector has advantages in projection speed and light spectrum. By rotating a circular tube with fringe patterns—which is similar to praxinoscope—we can retrieve the phase information of the object. Because this circular projection device can project the fringe patterns in all directions, depending on the direction of light source, we can determine the projection area. Additionally, we can put multiple light emitters inside the tube, which means that it is possible to work as multiple projectors to scan surrounding environments. By using these multiple projection system, the customized system can capture a 360-degree 3D image at a time and the image can be used to inspect narrow tunnels of bridges and water pipes.

REFERENCES

REFERENCES

[1] G. Sansoni, M. Trebeschi, and F. Docchio, "State-of-the-art and applications of 3d imaging sensors in industry, cultural heritage, medicine, and criminal investigation," *Sensors*, vol. 9, no. 1, pp. 568–601, 2009.

[2] Martins, Fernando António Rodrigues and García-Bermejo, Jaime Gómez and Casanova, Eduardo Zalama and González, José R Perán, "Automated 3D surface scanning based on CAD model," *Mechatronics*, vol. 15, no. 7, pp. 837–857, 2005.

[3] M. Germani, F. Mandorli, M. Mengoni, and R. Raffaeli, "CAD-based environment to bridge the gap between product design and tolerance control," *Precision Engineering*, vol. 34, no. 1, pp. 7–15, 2010.

[4] S. Zhang, "High-speed 3d shape measurement with structured light methods: A review," *Optics and Lasers in Engineering*, vol. 106, pp. 119–131, 2018.

[5] B. Khoshnevis, "Automated construction by contour crafting—related robotics and information technologies," *Automation in construction*, vol. 13, no. 1, pp. 5–19, 2004.

[6] T. Bock, "The future of construction automation: Technological disruption and the upcoming ubiquity of robotics," *Automation in Construction*, vol. 59, pp. 113–121, 2015.

[7] S. Cai, Z. Ma, M. Skibniewski, J. Guo, and L. Yun, "Application of automation and robotics technology in high-rise building construction: An overview," in *ISARC. Proceedings of the International Symposium on Automation and Robotics in Construction*, vol. 35. IAARC Publications, 2018, pp. 1–8.

[8] American Road and Transportation Builders Association. (2018) Deficient bridge report. [Online]. Available: https://www.artbabridgereport.org

[9] R. Ranasinghe, G. Dissanayake, and D. Liu, "Sensing for autonomous navigation inside steel bridges," in *2018 IEEE SENSORS*. IEEE, 2018, pp. 1–4.

[10] S. J. Lorenc, B. E. Handlon, and L. E. Bernold, "Development of a robotic bridge maintenance system," *Automation in Construction*, vol. 9, no. 3, pp. 251–258, 2000.

[11] P. Chotiprayanakul, D. Liu, and G. Dissanayake, "Human–robot–environment interaction interface for robotic grit-blasting of complex steel bridges," *Automation in Construction*, vol. 27, pp. 11–23, 2012.

[12] G. Paul, P. Quin, A. W. K. To, and D. Liu, "A sliding window approach to exploration for 3d map building using a biologically inspired bridge inspection robot," in *2015 IEEE International Conference on Cyber Technology in Automation, Control, and Intelligent Systems (CYBER)*. IEEE, 2015, pp. 1097–1102.

[13] DARPA. "DARPA Urban Challenge". [Online]. Available: https://www.darpa.mil/about-us/timeline/darpa-urban-challenge

[14] On-Road Automated Driving Committee, "Taxonomy and definitions for terms related to on-road motor vehicle automated driving systems," SAE International, Tech. Rep., 2014.

[15] J. Van Brummelen, M. O'Brien, D. Gruyer, and H. Najjaran, "Autonomous vehicle perception: The technology of today and tomorrow," *Transportation research part C: emerging technologies*, vol. 89, pp. 384–406, 2018.

[16] J.-F. Bonnefon, A. Shariff, and I. Rahwan, "The social dilemma of autonomous vehicles," *Science*, vol. 352, no. 6293, pp. 1573–1576, 2016.

[17] T. Ojha, S. Misra, and N. S. Raghuwanshi, "Wireless sensor networks for agriculture: The state-of-the-art in practice and future challenges," *Computers and Electronics in Agriculture*, vol. 118, pp. 66–84, 2015.

[18] J. Alex Thomasson, Craig P. Baillie, Diogenes L. Antille, Cheryl L. McCarthy and Craig R. Lobsey, "A review of the state of the art in agricultural automation. part ii: On-farm agricultural communications and connectivity," no. 1801590. Optical Society of America, 2018, pp. 1–10.

[19] "Forensic science technology working group operational requirements," https://nij.ojp.gov/sites/g/files/xyckuh171/files/media/document/2018-11-forensic-twg-table.pdf, accessed: 2018-11.

[20] C. V. Poulton, A. Yaacobi, D. B. Cole, M. J. Byrd, M. Raval, D. Vermeulen, and M. R. Watts, "Coherent solid-state lidar with silicon photonic optical phased arrays," *Optics letters*, vol. 42, no. 20, pp. 4091–4094, 2017.

[21] M. I. Skolnik, "Introduction to radar systems," *New York, McGraw Hill Book Co., 1980. 590 p.*, 1980.

[22] B. Schoettle, "Sensor fusion: A comparison of sensing capabilities of human drivers and highly automated vehicles," *Ann Arbor: University of Michigan*, 2017.

[23] U. R. Dhond and J. K. Aggarwal, "Structure from stereo-a review," *IEEE transactions on systems, man, and cybernetics*, vol. 19, no. 6, pp. 1489–1510, 1989.

[24] D. Scharstein and R. Szeliski, "A taxonomy and evaluation of dense two-frame stereo correspondence algorithms," *International journal of computer vision*, vol. 47, no. 1-3, pp. 7–42, 2002.

[25] T. Kanade and M. Okutomi, "A stereo matching algorithm with an adaptive window: Theory and experiment," *IEEE Trans. Patt. Analy. and Mach. Intellig.*, vol. 16, no. 9, pp. 920–932, 1994.

[26] K.-J. Yoon and I. S. Kweon, "Adaptive support-weight approach for correspondence search," *IEEE transactions on pattern analysis & machine intelligence*, no. 4, pp. 650–656, 2006.

[27] Z. Ma, K. He, Y. Wei, J. Sun, and E. Wu, "Constant time weighted median filtering for stereo matching and beyond," in *Proceedings of the IEEE International Conference on Computer Vision*, 2013, pp. 49–56.

[28] Q. Yang, L. Wang, R. Yang, S. Wang, M. Liao, and D. Nister, "Real-time global stereo matching using hierarchical belief propagation." in *BMVC*, vol. 6. Citeseer, 2006, pp. 989–998.

[29] M. G. Mozerov and J. van de Weijer, "Accurate stereo matching by two-step energy minimization," *IEEE Transactions on Image Processing*, vol. 24, no. 3, pp. 1153–1163, 2015.

[30] M. Takeda and K. Mutoh, "Fourier transform profilometry for the automatic measurement of 3-d object shapes," *Appl. Opt.*, vol. 22, pp. 3977–3982, 1983.

[31] B. Li, Y. An, and S. Zhang, "Single-shot absolute 3d shape measurement with fourier transform profilometry," *Applied optics*, vol. 55, no. 19, pp. 5219–5225, 2016.

[32] Q. Kemao, "Two-dimensional windowed fourier transform for fringe pattern analysis: Principles, applications and implementations," *Opt. Laser. Eng.*, vol. 45, p. 304–317, 2007.

[33] H. Yun, B. Li, and S. Zhang, "Pixel by pixel absolute three-dimensional shape measurement with modified fourier transform profilometry," *Appl. Opt.*, vol. 56, no. 5, pp. 1472–1480, 2017, doi: 10.1364/AO.56.001472.

[34] J.-S. Hyun, G. T.-C. Chiu, and S. Zhang, "High-speed and high-accuracy 3d surface measurement using a mechanical projector," *Optics express*, vol. 26, no. 2, pp. 1474–1487, 2018.

[35] S. Zhang, "Absolute phase retrieval methods for digital fringe projection profilometry: a review," *Optics and Lasers in Engineering*, vol. 107, pp. 28–37, 2018.

[36] D. C. Ghiglia and M. D. Pritt, Eds., *Two-Dimensional Phase Unwrapping: Theory, Algorithms, and Software.* New York: John Wiley and Sons, 1998.

[37] R. M. Goldstein, H. A. Zebker, and C. L. Werner, "Two-dimensional phase unwrapping," *Radio Sci.*, vol. 23, pp. 713–720, 1988.

[38] M. Zhao, L. Huang, Q. Zhang, X. Su, A. Asundi, and Q. Kemao, "Quality-guided phase unwrapping technique: comparison of quality maps and guiding strategies," *Appl. Opt.*, vol. 50, no. 33, pp. 6214–6224, 2011.

[39] G. Sansoni, M. Carocci, and R. Rodella, "Three-dimensional vision based on a combination of gray-code and phase-shift light projection: analysis and compensation of the systematic errors," *Applied optics*, vol. 38, no. 31, pp. 6565–6573, 1999.

[40] Y. Wang, S. Zhang, and J. H. Oliver, "3d shape measurement technique for multiple rapidly moving objects," *Optics express*, vol. 19, no. 9, pp. 8539–8545, 2011.

[41] Q. Zhang, X. Su, L. Xiang, and X. Sun, "3-d shape measurement based on complementary gray-code light," *Optics and Lasers in Engineering*, vol. 50, no. 4, pp. 574–579, 2012.

[42] K. Liu, Y. Wang, D. L. Lau, Q. Hao, and L. G. Hassebrook, "Dual-frequency pattern scheme for high-speed 3-d shape measurement," *Opt. Express*, vol. 18, no. 5, pp. 5229–5244, 2010.

[43] D. P. Towers, J. D. C. Jones, and C. E. Towers, "Optimum frequency selection in multi-frequency interferometry," *Opt. Lett.*, vol. 28, pp. 1–3, 2003.

[44] Y. Wang, J. I. Laughner, I. R. Efimov, and S. Zhang, "3d absolute shape measurement of live rabbit hearts with a superfast two-frequency phase-shifting technique," *Opt. Express*, vol. 21, no. 5, pp. 5822–5632, 2013, (*Cover feature*), (Selected for May 22, 2013 issue of The *Virtual Journal for Biomedical Optics*); doi: 10.1364/OE.21.005822.

[45] Y. An, J.-S. Hyun, and S. Zhang, "Pixel-wise absolute phase unwrapping using geometric constraints of structured light system," *Optics Express*, vol. 24, no. 16, pp. 18 445–18 459, 2016.

[46] W. Lohry, V. Chen, and S. Zhang, "Absolute three-dimensional shape measurement using coded fringe patterns without phase unwrapping or projector calibration," *Opt. Express*, vol. 22, no. 2, pp. 1287–1301, 2014, doi:10.1364/OE.22.001287.

[47] T. Tao, Q. Chen, S. Feng, Y. Hu, J. Da, and C. Zuo, "High-precision real-time 3d shape measurement using a bi-frequency scheme and multi-view system," *Applied optics*, vol. 56, no. 13, pp. 3646–3653, 2017.

[48] X. Liu, D. He, H. Hu, and L. Liu, "Fast 3d surface measurement with wrapped phase and pseudorandom image," *Sensors*, vol. 19, no. 19, p. 4185, 2019.

[49] W. Yin, S. Feng, T. Tao, L. Huang, S. Zhang, Q. Chen, and C. Zuo, "Calibration method for panoramic 3d shape measurement with plane mirrors," *Optics Express*, vol. 27, no. 25, pp. 36 538–36 550, 2019.

[50] X. Su and W. Chen, "Reliability-guided phase unwrapping algorithm: a review," *Opt. Laser Eng.*, vol. 42, no. 3, pp. 245–261, 2004.

[51] Y.-Y. Cheng and J. C. Wyant, "Two-wavelength phase shifting interferometry," *Appl. Opt.*, vol. 23, pp. 4539–4543, 1984.

[52] Y.-Y. Cheng and J. C. Wyant, "Multiple-wavelength phase shifting interferometry," *Appl. Opt.*, vol. 24, pp. 804–807, 1985.

[53] G. Sansoni, M. Carocci, and R. Rodella, "Three-dimensional vision based on a combination of gray-code and phase-shift light projection: Analysis and compensation of the systematic errors," *Appl. Opt.*, vol. 38, pp. 6565–6573, 1999.

[54] Q. Z. X. Su, L. Xiang, and X. Sun, “3-d shape measurement based on complementary gray-code light,” *Opt. Laser Eng.*, vol. 50, pp. 574–579, 2012.

[55] Y. Li, H. Jin, and H. Wang, “Three-dimensional shape measurement using binary spatio-temporal encoded illumination,” *J. Opt. A, Pure Appl. Opt.*, vol. 11, no. 7, p. 075502, 2009.

[56] Y. Wang and S. Zhang, “Novel phase coding method for absolute phase retrieval,” *Opt. Lett.*, vol. 37, no. 11, pp. 2067–2069, 2012, doi: 10.1364/OL.37.002067.

[57] C. Zhou, T. Liu, S. Si, J. Xu, Y. Liu, and Z. Lei, “Phase coding method for absolute phase retrieval with a large number of codewords,” *Opt. Express*, vol. 20, no. 22, pp. 24 139–24 150, 2012.

[58] Canlin Zhou and Tongchuan Liu and Shuchun Si and Jianqiang Xu and Yepeng Liu and Zhenkun Lei, “An improved stair phase encoding method for absolute phase retrieval,” *Opt. Laser Eng.*, vol. 66, pp. 269–278, 2015.

[59] K. Creath, “Step height measurement using two-wavelength phase-shifting interferometry,” *Appl. Opt.*, vol. 26, pp. 2810–2816, 1987.

[60] D. Malacara, Ed., *Optical Shop Testing*, 3rd ed. New York, NY: John Wiley and Sons, 2007.

[61] B. Li, N. Karpinsky, and S. Zhang, “Novel calibration method for structured light system with an out-of-focus projector,” *Appl. Opt.*, vol. 53, no. 13, pp. 3415–3426, 2014, doi: 10.1364/AO.53.003415.

[62] L. Guo, X. Su, and J. Li, “Improved fourier transform profilometry for the automatic measurement of 3d object shapes,” *Optical Engineering*, vol. 29, no. 12, pp. 1439–1444, 1990.

[63] Y. Li, C. Zhao, Y. Qian, H. Wang, and H. Jin, “High-speed and dense three-dimensional surface acquisition using defocused binary patterns for spatially isolated objects,” *Opt. Express*, vol. 18, no. 21, pp. 21 628–21 635, 2010.

[64] S. Zhang and S.-T. Yau, “High-resolution, real-time 3-d absolute coordinate measurement based on a phase-shifting method,” *Opt. Express*, vol. 14, no. 7, pp. 2644–2649, 2006, doi: 10.1364/OE.14.002644.

[65] H. Cui, W. Liao, N. Dai, and X. Cheng, “A flexible phase-shifting method with absolute phase marker retrieval,” *Measurement*, vol. 45, pp. 101–108, 2012.

[66] Z. Li, K. Zhong, Y. F. Li, X. Zhou, and Y. Shi, “Multiview phase shifting: a full-resolution and high-speed 3d measurement framework for arbitrary shape dynamic objects,” *Opt. Lett.*, vol. 38, no. 9, pp. 1389–1391, 2013.

[67] C. Zuo, Q. Chen, G. Gu, S. Feng, F. Feng, R. Li, and G. Shen, “High-speed three-dimensional shape measurement for dynamic scenes using bi-frequency tripolar pulse-width-modulation fringe projection,” *Optics and Lasers in Engineering*, vol. 51, no. 8, pp. 953–960, 2013.

[68] Y.-Y. Cheng and J. C. Wyant, “Two-wavelength phase shifting interferometry,” *Appl. Opt.*, vol. 23, no. 24, pp. 4539–4543, 1984.

[69] Y. Wang and S. Zhang, "Superfast multifrequency phase-shifting technique with optimal pulse width modulation," *Opt. Express*, vol. 19, no. 6, pp. 5143–5148, 2011, doi: 10.1364/OE.19.005149.

[70] Y. Wang, S. Zhang, and J. H. Oliver, "3-d shape measurement technique for multiple rapidly moving objects," *Opt. Express*, vol. 19, no. 9, pp. 5149–5155, 2011, doi: 10.1364/OE.19.008539.

[71] B. Li, Y. Fu, J. Zhang, H. Wu, G. Xia, and G. Jiang, "A fast three-dimensional shape measurement method based on color phase coding," *Optik-International Journal for Light and Electron Optics*, vol. 127, no. 3, pp. 1011–1015, 2016.

[72] Y. Xing, C. Quan, and C. Tay, "A modified phase-coding method for absolute phase retrieval," *Opt. Laser Eng.*, vol. 87, pp. 97–102, 2016.

[73] N. Karpinsky, M. Hoke, V. Chen, and S. Zhang, "High-resolution, real-time three-dimensional shape measurement on graphics processing unit," *Opt. Eng.*, vol. 53, no. 2, p. 024105, 2014, doi: 10.1117/1.OE.53.2.024105.

[74] B. Li, N. Karpinsky, and S. Zhang, "Novel calibration method for structured-light system with an out-of-focus projector," *Appl. Opt.*, vol. 53, no. 16, pp. 3415–3426, 2014.

[75] Q. Kemao, "Windowed fourier transform for fringe pattern analysis," *Appl. Opt.*, vol. 43, p. 2695–2702, 2004.

[76] Y. Li, C. Zhao, Y. Qian, H. Wang, and H. Jin, "High-speed and dense three-dimensional surface acquisition using defocused binary patterns for spatially isolated objects," *Optics express*, vol. 18, no. 21, pp. 21 628–21 635, 2010.

[77] D. A. Zweig and R. E. Hufnagel, "Hilbert transform algorithm for fringe-pattern analysis," in *Advanced Optical Manufacturing and Testing*, vol. 1333. International Society for Optics and Photonics, 1990, pp. 295–302.

[78] M. Sutton, W. Zhao, S. McNeill, H. Schreier, and Y. Chao, "Development and assessment of a single-image fringe projection method for dynamic applications," *Experimental mechanics*, vol. 41, no. 3, pp. 205–217, 2001.

[79] M. Gdeisat, D. Burton, F. Lilley, and M. Arevalillo-Herráez, "Fast fringe pattern phase demodulation using fir hilbert transformers," *Optics Communications*, vol. 359, pp. 200–206, 2016.

[80] Y. An, J.-S. Hyun, and S. Zhang, "Pixel-wise absolute phase unwrapping using geometric constraints of structured light system," *Opt. Express*, vol. 24, no. 15, pp. 18 445–18 459, 2016, doi:10.1364/OE.24.018445.

[81] J.-S. Hyun and S. Zhang, "Enhanced two-frequency phase-shifting method," *Appl. Opt.*, vol. 55, no. 16, pp. 4395–4401, 2016, doi:10.1364/AO.55.004395.

[82] W. Lohry and S. Zhang, "Genetic method to optimize binary dithering technique for high-quality fringe generation," *Opt. Lett.*, vol. 38, no. 4, pp. 540–542, 2013, doi: 10.1117/1.OE.51.11.113602.

[83] S. Zhang, *High-speed 3D imaging with digital fringe projection technique*, 1st ed. New York, NY: CRC Press, 2016.

[84] K. Zhong, Z. Li, Y. Shi, and C. Wang, "Analysis of solving the point correspondence problem by trifocal tensor for real-time phase measurement profilometry," *Proc. SPIE*, vol. 8493, p. 8493, 2012.

[85] Z. Li, K. Zhong, Y. Li, X. Zhou, and Y. Shi, "Multiview phase shifting: a full-resolution and high-speed 3d measurement framework for arbitrary shape dynamic objects," *Opt. Lett.*, vol. 38, no. 9, pp. 1389–1391, 2013.

[86] K. Zhong, Z. Li, Y. Shi, C. Wang, and Y. Lei, "Fast phase measurement profilometry for arbitrary shape objects without phase unwrapping," *Opt. Laser Eng.*, vol. 51, no. 11, pp. 1213–1222, 2013.

[87] C. Brauer-Burchardt, P. Kuhmstedt, and G. Notni, "Phase unwrapping using geometric constraints for high-speed fringe projection based 3d measurements," *Proc. SPIE*, vol. 8789, pp. 878 906–1, 2013.

[88] R. Ishiyama, S. Sakamoto, J. Tajima, T. Okatani, and K. Deguchi, "Absolute phase measurements using geometric constraints between multiple cameras and projectors," *Appl. Opt.*, vol. 46, no. 17, pp. 3528–3538, 2007.

[89] C. Brauer-Burchardt, P. Kuhmstedt, M. Heinze, P. Kuhmstedt, and G. Notni, "Using geometric constraints to solve the point correspondence problem in fringe projection based 3d measuring systems," *Proc. 16th International Conference on Image Analysis and Processing*, vol. Part II, pp. 265–274, 2011.

[90] Y. R. Huddart, J. D. R. Valera, N. J. Weston, , and A. J. M. and, "Absolute phase measurement in fringe projection using multiple perspectives," *Opt. Express*, vol. 21, no. 18, pp. 21 119–21 130, 2013.

[91] C. Jiang and S. Zhang, "Absolute phase unwrapping for dual-camera system without embedding statistical features," *Opt. Eng.*, vol. 56, no. 9, p. 094114, 2017.

[92] V. Kolmogorov and R. Zabih, "Multi-camera scene reconstruction via graph cuts," in *Euro Conf. Comp. Vis.*, 2002, pp. 82–96.

[93] J. Kostková and R. Sára, "Stratified dense matching for stereopsis in complex scenes." in *Proc. Brit. Mach. Vis. Conf.*, 2003, pp. 339–348.

[94] H. Hirschmuller, "Stereo processing by semiglobal matching and mutual information," *IEEE Trans. Patt. Analysis Mach. Intellig.*, vol. 30, no. 2, pp. 328–341, 2008.

[95] F. Besse, C. Rother, A. W. Fitzgibbon, and J. Kautz, "Pmbp: Patchmatch belief propagation for correspondence field estimation," *Intl J. Comp. Vis.*, vol. 110, no. 1, pp. 2–13, 2013.

[96] S. Xu, F. Zhang, X. He, X. Shen, and X. Zhang, "Pm-pm: Patchmatch with potts model for object segmentation and stereo matching," *IEEE Transactions on Image Processing*, vol. 24, no. 7, pp. 2182–2196, 2015.

[97] S. Zhu and L. Yan, "Local stereo matching algorithm with efficient matching cost and adaptive guided image filter," *The Visual Computer*, vol. 33, no. 9, pp. 1087–1102, 2017.

[98] B. Li, Y. An, D. Cappelleri, J. Xu, and S. Zhang, "High-accuracy, high-speed 3d structured light imaging techniques and potential applications to intelligent robotics," *Intl Journal of Intelligent Robotics and Applications*, vol. 1, no. 1, pp. 86–103, 2017, doi:10.1007/s41315-016-0001-7.

[99] A. Geiger, M. Roser, and R. Urtasun, "Efficient large-scale stereo matching," in *Lecture Notes Comp. Sci.*, vol. 6492, 2011, pp. 25–38.

[100] K. Song, S. Hu, X. Wen, and Y. Yan, "Fast 3d shape measurement using fourier transform profilometry without phase unwrapping," *Optics and Lasers in Engineering*, vol. 84, pp. 74–81, 2016.

[101] S. Gai, F. Da, and X. Dai, "Novel 3d measurement system based on speckle and fringe pattern projection," *Optics express*, vol. 24, no. 16, pp. 17 686–17 697, 2016.

[102] X. Liu and J. Kofman, "High-frequency background modulation fringe patterns based on a fringe-wavelength geometry-constraint model for 3d surface-shape measurement," *Optics Express*, vol. 25, no. 14, pp. 16 618–16 628, 2017.

[103] D. Dudley, W. Duncan, and J. Slaughter, "Emerging digital micromirror device applications," in *Proc. SPIE*, vol. 4985, no. 14-25, 2003, p. 1.

[104] S. Heist, P. Lutzke, I. Schmidt, P. Dietrich, P. Kühmstedt, A. Tünnermann, and G. Notni, "High-speed three-dimensional shape measurement using gobo projection," *Optics and Lasers in Engineering*, vol. 87, pp. 90–96, 2016.

[105] A. Brahm, C. R*öß*ler, P. Dietrich, S. Heist, P. K*ü*hmstedt, and G. Notni, "Non-destructive 3d shape measurement of transparent and black objects with thermal fringes," *Proc. SPIE*, vol. 9868, p. 98680C, 2016.

[106] J.-S. Hyun, B. Li, and S. Zhang, "High-speed high-accuracy 3d shape measurement using digital binary defocusing method vs sinusoidal method," *Opt. Eng.*, vol. 56, no. 7, p. 074102, 2017, doi:10.1117/1.OE.56.7.074102.

[107] S. Lei and S. Zhang, "Digital sinusoidal fringe generation: defocusing binary patterns vs focusing sinusoidal patterns," *Opt. Laser Eng.*, vol. 48, no. 5, pp. 561–569, 2010, doi: 10.1016/j.optlaseng.2009.12.002.

[108] K. Chen, J. Xi, and Y. Yu, "Quality-guided spatial phase unwrapping algorithm for fast three-dimensional measurement," *Optics Communications*, vol. 294, pp. 139–147, 2013.

[109] M. Arevalillo-Herráez, M. Gdeisat, F. Lilley, and D. R. Burton, "A spatial algorithm to reduce phase wraps from two dimensional signals in fringe projection profilometry," *Optics and Lasers in Engineering*, vol. 82, pp. 70–78, 2016.

[110] S. Zhang and P. S. Huang, "Novel method for structured light system calibration," *Opt. Eng.*, vol. 45, no. 8, p. 083601, 2006, doi:10.1117/1.2336196.

[111] Y. Xu, L. Ekstrand, J. Dai, and S. Zhang, "Phase error compensation for three-dimensional shape measurement with projector defocusing," *Appl. Opt.*, vol. 50, no. 17, pp. 2572–2581, 2011, doi: 10.1364/AO.50.002572.

VITA

Jae-Sang Hyun is a PhD candidate at the School of Mechanical Engineering at Purdue University. He received his BS degree from the School of Mechanical Engineering in Yonsei University. His research interests focus on high-speed 3D reconstruction, high-resolution 3D scanning, 3D sensor design, robotics, simultaneous localization and mapping, 3D data compression, and machine vision. By the time he graduates, he will have published 14 research articles, including nine journal papers and five conference proceedings.

LIST OF PUBLICATIONS

Journal articles

[9] Y. Wang, J. -S. Hyun, S. Zhang, B. Luo, Z. Liu, C. Jiang, B. Tao, “Multilevel symmetric pattern design and optimization for high-speed and high-accuracy 3D shape measurement,” Optics and Lasers Technology, (2020)

[8] J. -S. Hyun, and S. Zhang, “High-speed three-dimensional absolute shape measurement with three binary patterns,” Optical Engineering, 59(2), 024104, (2020)

[7] X. Hu, G. Wang, J. -S. Hyun, Y. Zhang, H. Yang, and S. Zhang, “Autofocusing method for high-resolution three-dimensional profilometry,” Optics Letters 45(2), 375-378, (2020)

[6] M. Zhong, J. Cui, J. -S. Hyun, L. Pan, P. Duan, and S. Zhang, “Uniaxial 3D phase-shifting profilometry using a dual-telecentric structured light system in micro-scale devices,” Measurement Science and Technology, (2019)

[5] J. -S. Hyun, George T-C Chiu, and S. Zhang, ”High-speed and high-accuracy 3D surface measurement using a mechanical projector,” Optics Express 26 (2), 1474-1487, (2018)

[4] J. –S. Hyun, B. Li, and S. Zhang, “High-speed high-accuracy three-dimensional shape measurement using digital binary defocusing method versus sinusoidal method,” Optical Engineering 56(7), 074102, (2017)

[3] J. -S. Hyun and S. Zhang, ”Superfast 3D absolute shape measurement using five binary patterns,” Optics and Lasers in Engineering, 90, 217-224, (2017)

[2] J. -S. Hyun, and S. Zhang, ”Enhanced two-frequency phase-shifting method,” Applied Optics, 55(16), 4395-4401, (2016)

[1] Y. An, J. -S. Hyun, and S. Zhang, ”Pixel-wise absolute phase unwrapping using geometric constraints of structured light system”, Optics Express, 24(15), 18445-18459, (2016)

Conference papers

[5] J. –S. Hyun, and S. Zhang, “Phase-based Stereo Matching for High-accuracy Three-dimensional Optical Sensing,” 2019, Frontiers in Optics

[4] J. -S. Hyun, and S. Zhang, “High-speed three-dimensional shape measurement with three binary patterns using a Hilbert transform,” 2019, Proc of SPIE

[3] J. -S. Hyun, M. G. Carmichael, A. Tran, S. Zhang and D. Liu, “Evaluation of fast, high-detail projected light 3D sensing for robots in construction,” 2019, Proc. of IEEE

[2] J. –S. Hyun, and S. Zhang, “High-speed 3D surface measurement with mechanical projector”, 2017, Proc. of SPIE

[1] S. Zhang, J. –S. Hyun, and B. Li, “High-speed 3D imaging using digital binary defocusing method vs sinusoidal method”, 2017, Proc. of SPIE